DISSERTATION

submitted to the
Combined Faculties for the Natural Sciences and for Mathematics
of the Ruperto-Carola University of Heidelberg, Germany
for the degree of
Doctor of Natural Sciences

presented by
Diplom-Chemiker Thorsten M. Staudt
born in Bruchsal

Oral examination: March 27th, 2009

Strategies to reduce photobleaching, dark state transitions and phototoxicity in subdiffraction optical microscopy

Referees: Prof. Dr. Jürgen Wolfrum
Prof. Dr. Stefan W. Hell

Kurzzusammenfassung

In allen fluoreszenz-mikroskopischen Methoden, die unterhalb des *Abbeschen* Beugungslimits arbeiten, ist das theoretisch unbegrenzte Auflösungsvermögen durch Photobleichen der Farbstoffe limitiert. Wiederholtes Abrastern der Probe, wie beispielsweise bei drei-dimensionalen Aufnahmen nötig, erhöht das Photobleichen, die Bevölkerung von Dunkelzuständen, oder, bei lebenden Zellen, die Phototoxizität. Speziell für solche Anwendungen müssen alle Möglichkeiten zur Bleichreduzierung ausgeschöpft werden. In dieser Arbeit werden verschiedene chemische und physikalische Ansätze zur Bleichreduzierung exemplarisch an *stimulated emission depletion* (STED) Mikroskopie, dem ersten und prominentesten Verfahren zur Bildgebung unterhalb der Beugungsgrenze, erörtert. Das hierfür konzipierte STED Mikroskop kann aufgrund eines neuartigen, einstellbaren Spektral- und Phasenfiltersystems schnell an neue Fluoreszenzfarbstoffe mit verbesserten chemischen und photophysikalischen Eigenschaften angepasst werden und konventionelle Filter mit festgeschriebenen Eigenschaften ersetzen. Ferner erlaubt der optische Aufbau eine schonende Beleuchtungsstrategie. Die erhöhte Auflösung ermöglicht eine viel genauere, lokal angepasste Beleuchtung der Probe. Hiermit werden drei-dimensionale STED Aufnahmen möglich und die Farbstoffpalette um die bislang ungenutzte, bleichanfällige Farbstoffklasse der Cumarine bis in den blaugrünen Bereich erweitert. Der Farbstoff selbst bietet einen weiteren Ansatzpunkt, um bleichbezogene Probleme zu vermeiden. Die Fluoreszenz von Mn dotierten ZnSe Quantum Nanokristallen wird hier erstmals durch Licht via *excited-state absorption* (ESA) moduliert. Dies ermöglicht eine neue Art der Fernfeldfluoreszenzmikroskopie mit beugungs-unbegrenzter Auflösung basierend auf *Quantum Dots,* die sich generell durch eine hohe Photostabilität auszeichnen. Die Probeneinbettung ist ebenfalls von entscheidender Bedeutung, um sphärische Abberationen und Streulicht zu vermeiden, und das Signal-zu-Rausch Verhältnis zu maximieren. Hierfür wird ein vollständig wasserlösliches Einbettmedium, 2,2´-Thiodiethanol (TDE) beschrieben, das die Brechzahl bis hin zu Immersionsöl anpassen kann und hochaufgelöste Aufnahmen tief in fixierten Proben ermöglicht.

Abstract

In all subdiffraction fluorescence microscopy techniques, the theoretically infinite attainable resolution is, in practice, limited by the photobleaching of fluorophores. Repetitive scans of the sample required for e.g. three-dimensional recordings, increase photobleaching, dark state transitions and, in case of living cells, phototoxicity. To advance such experiments all possibilities to reduce the photobleaching must be explored. In this thesis, various chemical and physical approaches to tackle photobleaching are studied within the context of stimulated emission depletion (STED) microscopy, which is the first and most prominent method for subdiffraction imaging. The STED setup constructed for this purpose allows for the fast adaptation to new fluorescent dyes, and relies on a novel adaptive spectral and phase filter technique. Furthermore, the optical setup facilitates a gentle exposure strategy, in which the time that the dye is irradiated is significantly reduced. Three-dimensional images can therefore be recorded, and the palette of applicable dyes can be expanded to the blue-green regime by the so far unemployed coumarin derivatives, which are known to be prone to photobleaching. The label itself is another vantage point from which photobleaching limitations in subdiffraction microscopy can be circumvented. For the first time, light-driven modulation of the fluorescence from Mn-doped ZnSe quantum nanocrystals has been established through excited-state absorption (ESA). This enables a new type of far-field fluorescence microscopy with diffraction-unlimited resolution based on quantum dots, which are well known for their superior photostability. The correct sample embedding in the refractive index matching is also of high importance, if spherical aberrations and light scattering are to be minimized to optimize the fluorescence collection. For this purpose, an embedding medium, 2,2′-thiodiethanol (TDE) is introduced, which, by being miscible with water at any ratio, allows for refractive index matching up to that of immersion oil and making high resolution recordings deep within the sample feasible.

Zusammenfassung

Die Fluoreszenzmikroskopie vereinigt Spezifität und Empfindlichkeit auf eine einzigartige Art und Weise, um sowohl dynamische Prozesse, als auch statische Verteilungen von Objekten zu untersuchen. Dies macht die Fluoreszenzmikroskopie zu einer Schlüsseltechnologie bei der Beantwortung biologischer Fragestellungen. Es gibt jedoch eine entscheidende Einschränkung in der Fernfeldmikroskopie: aufgrund der Beugung ist es nicht möglich, Licht auf einen beliebig kleinen Punkt zu fokussieren. Zwei Objekte, die weniger als die Hälfte der Wellenlänge des verwendeten Lichts voneinander entfernt sind, können nicht voneinander getrennt werden und erscheinen im Bild als ein einziger verwaschener Fleck. *Ernst Abbe* erkannte diese Beugungsgrenze vor über einem Jahrhundert und deren Gültigkeit wurde bis in die 90er Jahre nicht in Frage gestellt. Da alle Fluoreszenzmoleküle innerhalb des beugungsbegrenzten Fokus gleichzeitig angeregt werden, fluoreszieren sie auch ungefähr zur selben Zeit, was eine Unterscheidung der einzelnen Marker unmöglich macht.

Das zeitlich getrennte, der Reihe nach erfolgende Auslesen der Fluoreszenz der einzelnen Objekte ist die grundlegende Idee, welche die Auflösung unterhalb der Beugungsgrenze ermöglicht. Hierfür werden die Marker eines Objekts in einen „signalgebenden“ Zustand überführt, während die anderen Marker in einem „dunklen“ Zustand verbleiben oder gebracht werden. Wenn die Marker in zwei konkreten Zuständen vorliegen können, beispielsweise in einem fluoreszenten und einem nicht-fluoreszenten Zustand, dann ist eine Auflösung unterhalb des Beugungslimits durch sukzessives Abfragen der hellen Marker möglich.

Das prominenteste Verfahren zur Hochauflösung ist die *stimulated emission depletion* (STED) Mikroskopie, bei der dem Anregungslaserstrahl ein zweiter Laserstrahl genau überlagert wird. Der Strahl des zweiten Lasers weist in der Mitte eine Nullstelle auf und verhindert die Fluoreszenz am Randbereich des Anregungslasers durch stimulierte Emission. Mit beiden Lasern wird die Probe gezielt abgerastert wobei die Entstehung der Fluoreszenz auf die Nullstelle eingeschränkt, und somit die Information sequenziell ausgelesen wird. Die Koordinaten der Farbstoffmoleküle können auch durch einfache Schwerpunktsbestimmung der einzelnen mehr als das Beugungslimit voneinander entfernten, zufällig angeschalteten Fluoreszenz-Flecke festgelegt werden (*photo-activated localization microscopy* (PALM), *stochastic optical reconstruction microscopy* (STORM)). Die Nanoskopie eröffnet ungeahnte Details und neue Einblicke in zelluläre Systeme und Mechanismen.

Für das gezielte Auslesen von Ensembles (STED) werden hohe Intensitäten zur Signalunterdrückung am Rand des beugungsbegrenzten Flecks und Trennung der Signale benötigt. Je höher die Intensitäten zur Signalunterdrückung sind, desto besser lassen sich die einzelnen Objekte innerhalb des beugungsbegrenzten Fokus auflösen. Die Hochauflösung basierend auf stochastischem Auslesen von Einzelfarbstoffmolekülen (STORM, PALM) benötigt dagegen hohe Signalintensitäten, um die Objekte möglichst exakt lokalisieren zu können. Je mehr Photonen von einem Objekt durch lange Integrationszeiten oder hohe Anregungsintensitäten gesammelt werden, desto genauer kann das Objekt lokalisiert werden. In beiden Fällen sind die erhöhten Intensitäten oder langen Integrationszeiten mit erhöhten Lichtdosen und somit mit erhöhtem Photobleichen verbunden. Im Allgemeinen erfordert die hochauflösende Bildgebung kleinere Pixelgrößen im Vergleich zur konfokalen Mikroskopie, um die gesamte Information zu erfassen. Ein feineres Abrastern der Probe ist bei gleichbleibender Integrationszeit (abhängig von der Probe) jedoch mit höheren Beleuchtungsdosen und verstärktem Photobleichen, Aufbau von Dunkelzuständen und erhöhter Phototoxizität verbunden. Photobleichen wird durch irreversible chemische Reaktionen der Fluoreszenzfarbstoffe im angeregten Zustand mit umgebenden reaktiven Spezies (Radikale, Oxidationsmittel) verursacht. Zu starkes Photobleichen verhindert immer die Hochauflösung, da es die maximal detektierbare Photonenanzahl beziehungsweise die maximale Intensität zur Signalunterdrückung bei nullstellenbasierten Hochauflösungsmethoden limitiert. Die Verringerung des Photobleichens, der Phototoxizität und des Aufbaus von Dunkelzuständen ist deshalb eine der wichtigsten Aufgaben vor allem im Streben nach immer besserer Auflösung, der Hochauflösung von zellulären Prozessen oder der Hochauflösung in drei Dimensionen.

Im Rahmen dieser Arbeit werden grundlegende chemische und physikalische Strategien zur Reduzierung des Photobleichens, der Phototoxizität und des Aufbaus von Dunkelzuständen in der hochauflösenden optischen Mikroskopie entwickelt und diskutiert.

Erstens, die bestmögliche Ausnutzung des Emissionsspektrums eines Fluoreszenzfarbstoffs garantiert eine ausreichende Signalstärke bei idealer Anregungsintensität und minimiert daher das Photobleichen. In dieser Arbeit wird ein Aufbau zur STED-Mikroskopie vorgestellt, der sich durch hohe Flexibilität auszeichnet, und eine schnelle und verlässliche Anpassung an neu entwickelte Farbstoffe mit verbesserten Eigenschaften erlaubt. Um neue Farbstoffe und alternative Laser einsetzen zu können, ist es von Vorteil, wenn verschiedene Bauteile eines optischen Aufbaus über einen breiten Wellenlängenbereich anpassbar sind. In dieser Arbeit

wird ein einstellbarer Spektral- und Phasenfilter vorgestellt. Als Spektralfilter werden typischerweise Interferenzfilter eingesetzt, die unveränderbare Eigenschaften besitzen. Solche Interferenzfilter können durch das hier vorgestellte, einstellbare Filtersystem ersetzt werden. In den nullstellenbasierten Hochauflösungsmethoden sind die Ansprüche an die Filtersets sehr hoch. Im Falle der STED-Mikroskopie wird ein zweiter Laserstrahl zur Signalunterdrückung verwendet, dessen Wellenlänge notwendigerweise innerhalb des Fluoreszenzspektrums liegt. Ein einstellbarer, *Notch*- oder Bandpassfilter ist daher sehr wünschenswert, um das sehr intensive STED-Licht zu entfernen ohne gleichzeitig zu viel Fluoreszenzlicht zu opfern.
Der hier vorgestellte Phasenfilter zur Erzeugung der Nullstelle bietet neben der Anpassbarkeit an verschiedenste Laserlinien zusätzlich die Möglichkeit einer deutlichen Vereinfachung des optischen Aufbaus. Sowohl der Anregungs-, als auch der STED-Strahl können aus einer Laser- oder Faserquelle stammen und sind somit *per se* genau überlagert. Der Phasenfilter wird von beiden Strahlen durchlaufen und erzeugt aufgrund der Dispersion eine Nullstelle für den STED-Strahl, und lässt den blauverschobenen Anregungs-Strahl unverändert.

Zweitens, adaptive Probenbeleuchtung mit Hilfe der nullstellenbasierten Hochauflösungsinformation. Die verbesserte Auflösung ermöglicht eine gezielte Beleuchtung der Probe im Falle der nullstellenbasierten Hochauflösungsmethoden (STED, *excited-state absorption* (ESA)). Im Rahmen dieser Arbeit wird eine effektive Methode beschrieben, um die Gesamtzahl an Anregungs- und Signalunterdrückungszyklen eines Fluoreszenzmoleküls zu reduzieren (*reduction of excitation and signal suppression cycles* (RESCue)) und somit das Photobleichen zu minimieren. Die Bleichverringerung ist anwendbar auf nullstellenbasierte Hochauflösungsmethoden, bei denen ein metastabiler „Dunkel“-Zustand genutzt wird (STED, ESA), und wird in dieser Arbeit exemplarisch an STED-Mikroskopie gezeigt. Sie erfolgt ohne Einbußen bei Auflösung oder Aufnahmegeschwindigkeit. Die Probe wird nur dann ausgiebig beleuchtet, wenn das Signal nicht durch einen bestimmten Prozess wie beispielsweise stimulierte Emission oder ESA unterdrückt wird beziehungsweise überhaupt vorhanden ist. Die Entscheidung über eine länger andauernde Beleuchtung wird in Abhängigkeit des Photonenflusses während eines Bruchteils der Integrationszeit auf einem Pixel getroffen. Wenn von einem Objekt eine bestimmte Anzahl von Fluoreszenzphotonen während des ersten Teils der Integrationszeit detektiert werden, bleiben die Laser für die verbleibende Zeit der Integrationsdauer angeschaltet. Die augenblickliche Kenntnis der genauen Position des fluoreszierenden Objekts innerhalb der Probe hilft bei der Verringerung der Anzahl der Schaltzyklen und deshalb bei der Verringerung des Photobleichens, der Phototoxizität, des

Aufbaus von Dunkelzuständen und der Ermüdung von Schaltprozessen, wichtige Hürden in allen Nanoskopiemethoden. Die STED-Mikroskopie und ihre verbesserte Auflösung kann somit die Fluoreszenz sogar stärker erhalten als die Konfokalmikroskopie, wie an fluoreszenten Partikeln eindrucksvoll gezeigt wird. Die Effizienz dieser Methode wird ebenfalls durch eine Reihe biologischer Anwendungen untermauert. Eine Bleichreduktion um den Faktor vier wird in Atto565 markierten Glialzellen erzielt. Ganz allgemein ermöglicht der RESCue-Modus hochaufgelöste Aufnahmen, die mit hohen Beleuchtungsdosen verbunden sind, wie beispielsweise Aufnahmen in drei Dimensionen. Mit Hilfe der adaptiven Beleuchtungsstrategie kann nun die bislang unerschlossene, bleichanfällige Farbstoffklasse der Cumarine in der STED-Mikroskopie eingesetzt werden.

Drittens, Optimierungen der Marker selbst bezüglich Photostabilität, hoher Emissionsraten, Schaltbarkeit und zusätzlicher photo-physikalischer Eigenschaften ebnen den Weg zu Ultrahochauflösung und Hochauflösung von lebenden Zellen. Neue, kontrollierbare Realisierungen von „signalgebenden“ und „dunklen“ Zuständen könnten im Falle der nullstellenbasierten Hochauflösungsmethoden mit geringeren Intensitäten zur Signalunterdrückung auskommen. Dies kann in verringertem Photobleichen, Phototoxizität und Aufbau von Dunkelzuständen resultieren. Darüber hinaus tolerieren Marker mit verbesserter Photostabilität höhere Intensitäten zur Signalunterdrückung, was direkt zu höherer Auflösung führt im Falle der nullstellenbasierten Hochauflösungsmethoden beziehungsweise zu einer exakteren Bestimmung der Koordinaten der Fluoreszenzfarbstoffe bei den stochastischen Ausleseverfahren. *Quantum Dots* als Fluoreszenzfarbstoffe sind bekannt für ihre hervorragende Photostabilität. In dieser Arbeit wurde die Modulation der Fluoreszenz von Mn dotierten ZnSe Quantum Nanokristallen durch Licht erreicht. Hierbei konkurriert ein Absorptionsprozess der Kristalle im angeregten Zustand (*excited-state absorption* (ESA)) direkt mit der spontanen Emission. Diese Kontrolle über elektronische Übergänge auf optischem Wege ermöglicht eine neue Art der Fernfeldfluoreszenzmikroskopie mit beugungs-unbegrenzter Auflösung basierend auf *Quantum Dots*.

Viertens, Optimierung der optischen Bedingungen der „letzten Linse“ durch Einbettung der Probe in ein Medium, das den Brechungsindex genau anpasst, führt zu einem verbesserten Signal-zu-Rausch Verhältnis und einem schärferen fokalen Lichtfleck, was wiederum verringerte Beleuchtungsdosen nach sich zieht. Andererseits verhindert Streulicht, das durch eine Fehlanpassung des Brechungsindex verursacht wird, hochauflösende Bildgebung tief in der Probe. Das Einbettmedium selbst besitzt die Eigenschaft eines Antioxidanz und kann somit das Photobleichen der Fluoreszenzfarbstoffe verhindern, da es in sehr hohen Konzentrationen zur Verfügung steht. Höhere Beleuchtungsdosen können so besser toleriert werden.

Der Gebrauch von Objektiven mit hoher numerischer Apertur wird von sphärischen Abberationen beeinträchtigt, die durch sprunghafte Änderung der Brechungsindices zwischen der Immersion und der Probeneinbettung hervorgerufen werden. Besonders wenn mehr als 10 µm tief in die Probe fokusiert wird, führen Fehlanpassungen der Brechungsindices zu einem deutlichen Verlust an Signalintensität und Auflösung. Der genaue Abgleich der Brechungsindices von Probeneinbettung und Immersion löst diese Probleme. Es gibt nur wenige Substanzen, die sowohl einen einstellbaren Brechungsindex aufweisen, als auch mit der Fluoreszenzmikroskopie verträglich sind. In der vorliegenden Arbeit wird ein nicht toxisches, vollständig wasserlösliches Einbettmedium, 2,2´-Thiodiethanol (TDE), vorgestellt, mit dessen Hilfe sich der durchschnittliche Brechungsindex der Probe von 1.333 (Wasser) bis hin zu 1.518 (Immersionsöl, n_D bei 23°C) genau einstellen lässt. Somit können nach Einbettung in TDE tief in fixierten Proben hochaufgelöste Aufnahmen mit Hilfe von Objektiven, die höchste Aperturwinkel aufweisen, gemacht werden. Generell hat die Einbettung in TDE das Potenzial, die Glyceroleinbettung überflüssig zu machen. Die Änderungen der Brechungsindices innerhalb der Probe aufgrund dichter, zellulärer Substrukturen wie zum Beispiel am Kern werden weitestgehend aufgehoben. Zusätzlich erhält TDE aufgrund seiner Eigenschaft als Antioxidanz die Quantenausbeuten der meisten gängigen Fluoreszenzfarbstoffe. Die optischen und chemischen Eigenschaften dieses neuen Einbettmediums werden hier diskutiert und Anwendungen auf verschiedenartig gefärbte Zellen und zelluläre Substrukturen aufgezeigt. Der Einfluss des Einbettungsmediums auf verschiedene Bildgebungsverfahren (Konfokalmikroskopie, 4Pi-Mikroskopie, STED-Mikroskopie) wird gezeigt.

Alle hier dargestellten Strategien können miteinander kombiniert werden, um bleichbezogene Probleme zu lösen. Die Grundvoraussetzung für die Bleichreduzierung durch *RESCue* ist eine hervorragende Auflösung. Eine gute Anpassung der Brechungsindices, photostabile Farbstoffe und eine effiziente Detektion sind Grundvoraussetzungen für die hochauflösende Mikroskopie. Die verbesserten Bleicheigenschaften können in noch höhere Auflösung investiert werden. Es ist auch denkbar, dass die Hochauflösung von dynamischen Prozessen durch Bleichreduzierung erst ermöglicht wird, da dabei wiederholt abgerastert werden muss. In dieser Arbeit wird gezeigt, wie die Verringerung des Photobleichens die Bildgebung hochaufgelöster Details in drei Dimensionen und den Einsatz bleichanfälliger Farbstoffe in der STED-Mikroskopie erlaubt.

Verglichen mit den stochastischen Hochauflösungsmethoden (STORM, PALM) bietet die STED-Mikroskopie eine deutlich überlegenere Zeitauflösung. Bei 30 Bildern in der Sekunde lassen sich beispielsweise synaptische Vesikel in lebenden Zellen mit hoher lateraler Auflösung untersuchen. Gezieltes Auslesen von Farbstoffensembles ist nicht nur zeitlich schneller als stochastisches Auslesen von Einzelmolekülen; es bietet zusätzlich die Möglichkeit, die Beleuchtung analog zu *RESCue* lokal zu dosieren und somit Photobleichen, Aufbau von Dunkelzuständen und Phototoxizität zu reduzieren ohne Auflösung einzubüßen. Ultimative Ergebnisse lassen sich in Zukunft durch spezielle Konstruktion der Beleuchtungsfunktion in Kombination mit der Manipulation der „Dunkel-“Zustände erreichen.

Um zelluläre Vorgänge besser verstehen zu können, ist es das Ziel, dynamische Prozesse und Wechselwirkungen zellulärer Faktoren in lebenden Systemen dreidimensional mit höchster räumlicher und zeitlicher Auflösung zu untersuchen. Die Verringerung des Bleichens und der Phototoxizität wird hierbei eine entscheidende Rolle spielen.

Summary

The unique features of fluorescence microscopy to analyze dynamical processes and static distributions in an extraordinary sensitive and specific way make fluorescence microscopy to the key technology for answering biological questions. However, there is one crucial drawback of light microscopy, namely their resolution imposed by diffraction. Details that are closer than half the wavelength of light can not be discerned. More than one century ago *Ernst Abbe* discovered the diffraction barrier which has become a paradigm ever since. As all fluorescence markers within a diffraction limited focal spot are excited simultaneously, they all emit at about the same time, rendering their separation virtually impossible.

The key concept to overcome this problem is to read-out the fluorescent signals sequentially. To achieve that, some markers of a feature are transferred to a signal generating, “bright” state, while keeping the other markers in a “dark” state. The realization of a fluorescent and a non-fluorescent state of a dye molecule makes subdiffraction resolution possible by successively reading out the bright markers.

The most prominent high resolution method is stimulated emission depletion (STED) microscopy. Here, the excitation laser is superimposed by a second laser. The beam of the second laser displays a zero in the center and prevents the fluorescence in the outer rim of the excitation spot due to stimulated emission. The sample is scanned by both beams in a targeted manner whereas the emergence of fluorescence is confined to the zero and read out sequentially. The coordinates of the fluorescent features can also be determined by the centroids of the fluorescence spots switched on randomly (photo-activated localization microscopy (PALM), stochastic optical reconstruction microscopy (STORM)). These nanoscopic techniques disclose unexpected details and new insights into cellular systems.

For targeted readout of ensembles (STED), high signal suppression intensities are needed to separate the signals. The higher the signal suppression intensities, the better the possibility to resolve objects. The high resolution techniques based on stochastical read-out of single dye molecules (STORM, PALM) lack high photon counts to locate the features of interest accurately. The more information is gathered from an object due to higher dwell times or excitation intensities, the better it can be located. In either case, the increased intensities or longer pixel dwell times mean higher light doses and therefore pronounced photobleaching. Generally speaking, imaging with a high spatial resolution calls for smaller pixel sizes compared to confocal imaging in order to collect all the information. However, if the pixel

dwell time is kept constant (depends on the sample), a more precise dissection of the sample is accompanied by higher light doses affecting the sample, and therefore pronounced photobleaching, higher dark state transition rates and more severe phototoxicity. Photobleaching is caused by irreversible chemical reactions of the dye molecules in the excited state with surrounding reactive species (radicals, oxidative agents). Intense photobleaching always hinders subdiffraction imaging because it limits the maximal count rate or the maximal signal suppression intensities in zero based high resolution techniques. This renders the reduction of photobleaching, dark state transition rates and phototoxicity a bottle neck especially in the aim to achieve super high resolution images, high resolution live cell imaging and three-dimensional recordings.

In the framework of this thesis, several physical and chemical strategies are exploited to reduce photobleaching, dark state transition rates and phototoxicity in subdiffraction fluorescence microscopy techniques.

First, maximal exploitation of the emission spectrum of a fluorescent dye ensures a sufficient signal-to-noise ratio at ideal excitation intensities and therefore minimizes photobleaching. In this thesis, a STED setup is described, which is optimized for flexibility to adapt to new dyes with improved properties. To employ new dyes and alternative laser lines it would be advantageous, if the components of the optical setup are tunable with regard to the wavelength. A tunable phase and spectral filter is described here. Interference filters with fixed properties are typically used as spectral filters in conventional microscopes. The adaptive spectral filter reported here has the potential to replace standard thin film interference filters. The requirements on the filter sets are stringent, if intense signal suppression beams are applied to increase the resolution. In the case of STED microscopy, the beam is spectrally located within the emission spectrum of the dye. An adaptive notch- or bandpass filter that stops the intense STED light without wasting to much fluorescence light is highly desirable.

In addition to the adaptive spectral filter, a tunable phase filter to generate an intensity zero is described here. The new phase filter approach allows one to match every laser line and offers simultaneously a way to simplify a STED setup. The excitation beam as well as the STED beam can be provided by one laser or fiber source and are therefore inherently aligned. Both beams are passing through the phase plate and due to dispersion, a zero is generated for the STED beam whereas the excitation beam stays unaltered.

Second, adaptation of the light exposure affecting the sample due to the zero based high resolution information. A better resolution enables a more accurate exposure of the sample in case of zero based high resolution modalities (STED, excited-state absorption (ESA)). Here, an effective method is demonstrated to reduce the overall number of excitation and emission suppression cycles that a fluorescent molecule undergoes in all zero based high resolution modalities if the non-fluorescent state is metastable (reduction of excitation and signal suppression cycles (RESCue)). The effectiveness of this method is shown exemplarily on STED microscopy without suffering in loss in resolution or imaging speed. It relies on exposing the sample *in extenso* only if the fluorescence signal is not inhibited by any process (stimulated emission, ESA). The exposure decision is made depending on the photon flux during a fraction of the pixel dwell time. If a certain number of fluorescence photons from an object is detected within a first part of the pixel dwell time, the lasers remain on for the residual dwell time. The instantaneous knowledge of the accurate position of the fluorescent entities within the sample can be adapted to reduce the number of switching cycles and therefore to reduce photobleaching, dark state population, phototoxicity and switching fatigue significantly, all of which are important obstacles in every nanoscopic imaging mode. As shown with fluorescent beads, the STED mode and its improved resolution is able to preserve fluorescence even better than the confocal mode. The efficiency of this method is also demonstrated in varying biological samples. An up to four fold decrease in photobleaching is observed while imaging Atto565 labelled glial cells. In general, the RESCue mode enables subdiffraction imaging connected to high light doses such as three-dimensional imaging. Due to the adaptive light exposure strategy, the so far unexploited dye class of coumarin derivatives which is known to be prone to photobleaching, can now be employed for STED microscopy.

Third, optimization of labels themselves regarding photostability, fluorescence turnover, switchability and other photophysical properties paves the way for ultra high resolution imaging and high resolution live cell imaging. New realizations of “signal-giving” and “dark” states may work with lower signal suppression intensities in the case of zero based high resolution methods, leading to a lower light dose and reduced photobleaching, dark state transition rates and phototoxicity. Moreover, labels with improved photostability tolerate higher signal suppression intensities leading to higher resolution in the case of zero based techniques and to a more accurate centroid determination of the fluorescence spot for stochastic read-out methods. Quantum dots are fluorescent entities known for their superior photostability. In this thesis, light-driven modulation of the fluorescence from Mn-doped ZnSe quantum nanocrystals has been established through ESA and its direct competition with spontaneous emission. Such optical control over electronic transitions enables a new type of far-field fluorescence microscopy with diffraction-unlimited resolution based on quantum dots.

Fourth, optimization of the optical conditions of the "last lens", the sample, with the help of a refractive index matched embedding media leads to an improved signal-to-noise ratio and reduced blurring of the focal spot which in turn makes lower light doses possible. On the other hand, stray light caused by refractive index mismatch hinders high resolution imaging deeply inside the sample. Additionally the embedding media itself exhibits good antioxidant properties. So the antioxidant is inserted as an antifade in high concentrations enabling higher light doses without disturbing the optical properties.

The use of high numerical aperture immersion lenses in optical microscopy is compromised by spherical aberrations induced by refractive index mismatch between the immersion system and the embedding medium of the sample. Especially when imaging more than 10 μm deep inside the specimen, the refractive index mismatch results in a noticeable loss of image brightness and resolution. A solution to this problem is to match the index of the embedding medium to that of the immersion system. Unfortunately, not many mounting media are known that are both index tunable as well as compatible with fluorescence imaging. A non-toxic embedding medium, 2,2′-thiodiethanol (TDE) is introduced, which, by being miscible with water at any ratio, allows for fine adjustment of the average refractive index of the sample ranging from that of water (1.333) to that of immersion oil (n_D = 1.518 at 23°C). TDE thus enables high resolution imaging deep inside fixed specimens with objective lenses of the highest available aperture angles and has the potential to make glycerol embedding redundant. The refractive index changes due to larger cellular structures, such as nuclei, are largely compensated. Additionally, as an antioxidant, TDE preserves the fluorescence quantum yield of most of the fluorophores. The optical and chemical properties of this new medium as well as its application to a variety of differently stained cells and cellular sub-structures are described. The impact of the embedding media was tested for different imaging modes (confocal, 4Pi and STED microscopy).

All the strategies presented here can be combined to tackle photobleaching related problems. The basic requirement for RESCue is a superior resolution. Refractive index matching, photostable dyes and an efficient detection are basic requirements for high resolution imaging. The improved bleaching properties can be reinvested in even higher resolution, allowing high resolution imaging of dynamical processes that require repeated scans, or enables imaging in three dimensions.

STED microscopy offers an excellent time resolution compared to stochastically based high resolution methods (STORM, PALM). A frame rate of 30 images per second for example allows to analyze synaptic vesicles in living cells with a superior lateral resolution. Targeted read-out of fluorescence ensembles is not only faster compared to the stochastic read-out of single molecules, but also implies the possibility to adapt the sample exposure analogous to RESCue locally and therefore, to avoid photobleaching, dark state transitions and phototoxicity without sacrificing resolution enhancement. In the future, extraordinary results will be gained by combining “point spread function engineering” and “dark state engineering”. To understand the mechanisms behind life it is essential to quantitatively analyze dynamic processes and interactions of cellular factors in living systems three-dimensionally with the highest temporal and spatial resolution. For that, the reduction of photobleaching and phototoxicity plays a crucial role.

Contents

Abbreviations

3D	three-dimensional
ABS	absorption
AD	*Alzheimer´s* disease
AOTF	acousto-optic tunable filter
APD	avalanche photodiode
APP	amyloid precursor protein
BABB	benzylalcohol/benzylbenzoat
BS	beam splitter
CLEM	controlled light exposure microscopy
cT	cycle time
cw	continuous-wave
DABCO	1,4-diazabicyclo[2,2,2]octane
DMF	*N,N*-dimethylformamide
DMSO	dimethyl sulfoxide
DNA	deoxyribonucleic acid
D-REX	dark state relaxation
dSTORM	direct STORM
dT	dwell time
EGFP	enhanced green fluorescent protein
EM	electron microscope
EOM	electro-optic modulator
ESA	excited-state absorption
Fluor.	fluorescence
FP	fluorescent proteins
FPGA	field programmable gate array
FWHM	full-width at half-maximum
GFAP	glial fibrillary protein
GFP	green fluorescent protein
GSD	ground state depletion
GSDIM	ground state depletion followed by individual molecule return
IC	internal conversion

ICG	interchromatin granule
ISC	intersystem crossing
LC	liquid crystal
LSM	laser-scanning microscopy
lTh	lower threshold
MCA	multichannel analyzer
MEA	2-mercaptoethylamin
Mn-QDs	Mn-doped ZnSe quantum dot
MPM	multi-photon microscopy
mRFP	monomeric red fluorescent protein
NHS	*N*-hydroxysuccinimidyl
NMJ	neuromuscular junction
O	objective lens
OD	optical density
OTF	optical transfer function
PAINT	points accumulation for imaging in nanoscale topography
PALM	photo-activated localization microscopy
PALMIRA	PALM with independently running acquisition
PBS	prism based spectrometer
PBS	phosphate buffered saline
Phos.	phosphorescence
PLL	poly-L-lysine
PMA	poly(methylacrylate)
PP	phase plate
PPD	*p*-phenylenediamine
PSF	point spread function
QD	quantum dot
RESCue	reduction of excitation and signal suppression cycles
RESOLFT	reversible saturable optical fluorescence transition
RET	resonance energy transfer
RNA	ribonucleic acid
ROI	region of interest
ROS	reactive oxygen species
ROXS	reducing and oxidizing system

S	sample
SN	signal-to-noise ratio
SNOM	scanning near field optical microscopy
SPEM	saturated pattern excitation microscopy
STED	stimulated emission depletion
STORM	stochastic optical reconstruction microscopy
TDE	2,2´-thiodiethanol
TIRF	total internal reflection
T-REX	triplet state relaxation
uTh	upper threshold
VR	vibrational relaxation

Chapter 1

Introduction

In natural sciences, processes and conditions are observed, described, interpreted in a bigger context and discussed with people from other special fields. Nature spans a wide range of dimensions: from the size of protons and neutrons to the dimensions of the planetary systems or galaxies. Only a small part is visible to the naked eye. The bulk is hidden in the micro- or macrocosm. Early in history devices such as the microscope were introduced for observing processes and structures in small dimensions. Cell biology essentially started with light microscopy, which still is an essential tool. In recent years, microscopic techniques became ever more important, mostly owing to new developments in the field of specific labelling techniques and imaging of individual cellular elements and the reconstruction of their three-dimensional architecture. A big advantage of light microscopy is that movements and structures of distinct cellular compartments can be observed in living cells or organisms. One important property of a light microscope is its resolution which is defined as the distance of two similar objects that are only just imaged separately. The resolution sets the limit for conventional microscopy hindering the unraveling of a multitude of biological phenomenon. The development of new microscopy techniques is therefore a very active field of research.

A milestone in the development of light microscopy was the derivation of the wave theory of optical imaging in 1873 by *Ernst Abbe* (Abbe, 1873; Abbe, 1884). Abbe demonstrated how the diffraction of light by the specimen and the objective lens determines the resolution. This fact became a fundamental law of physics. The diffraction limit declares that it is not possible to focus light to an infinitesimal small spot by means of far-field optics. The lateral size of the focused spot is limited to $\Delta x = 0.5\lambda / NA$, with λ denoting the wavelength of the focused light, and the numerical aperture $NA = n*\sin\alpha$ describing the light collecting ability of the applied objective lens. The half cone angle α of light included by the objective lens and the refractive index n are technical obstacles. In the visible range (400 to 700 nm), the lateral resolution is limited to approximately 200 nm. Various constituents in cells like the ribosomes (macromolecular machines responsible for translation) with a size of 20 nm are much smaller than the resolution limit (Alberts, 2002). These structures would be imaged as a blurred spot without revealing any structural information. A strategy to resolve such dimensions is the application of light with a shorter wavelength according to *Abbe´s* law. The X-ray microscope discerns details in the range of 20 to 30 nm, the electron microscope (EM) is even capable of resolving 0.1 nm being suitable to discern molecular structures with a *de Broglie* wavelength of 0.004 nm. Aberrations of an electron lens are harder to correct, leading to discrepancy between theory (*Abbe*) and experiment (Alberts, 2002). The major drawback however is the high-energy radiation prohibiting the observation of living cells. Furthermore, the samples for EM have to be cut into thin slices because of the limited penetration depth of the radiation, thereby disturbing three-dimensional information. Often the contrast of structures with different densities has to be enhanced. Techniques for increasing the resolution in light microscopy are therefore highly exciting for biology, medicine and related research fields.

Another milestone was the introduction of fluorescence in light microscopy as a contrast due to its unchallenged sensitivity (Coons et al., 1942). With the aid of antibody specificity, immuno-fluorescent techniques became widespread in many branches of biology and medicine, and immunocytochemistry became established as an important subdiscipline of immunology and cytochemistry. The application of the green fluorescent protein (GFP) as a marker paved the way for fluorescence microscopy of living cells (Chalfie et al., 1994) and visualisation of dynamical processes because the cell itself produces the fluorescent label and links it directly to the desired protein. The importance of such observations in living cells was particularly demonstrated by the award of the *Nobel* prize for fluorescent proteins in 2008. Like no other contrast fluorescence offers an enormous variety of additional, detectable variables depending on the chemical surrounding. The intensity, fluorescence lifetime, emission spectra and the polarization of the emitted light sense the local environment in the vicinity of the fluorescence dye and allow discrimination from undesired signals such as autofluorescence. Together with coincidence analysis, the number of emitters within the focal spot can be determined and correlated to the number of proteins located in a distinct part of the cell (Weston et al., 2002). The possibility to manipulate fluorescence parameters permitted the development of high resolution techniques (STED, STORM, PALM) which are described in detail in the chapter 2.

Not only imaging was strongly influenced by fluorescence, but also spectroscopic approaches. A mechanism called resonance energy transfer (RET) provides a powerful tool to probe distances in the range of 1 to 10 nm well below the diffraction limit. RET is an electrodynamic phenomenon and occurs between a donor molecule in the excited state and an acceptor molecule in the ground state. The donor typically emits at shorter wavelengths overlapping with the absorption spectrum of the acceptor. A long ranged dipole-dipole interaction between the donor and the acceptor causes radiation-less energy transfer which leads to fluorescence of the acceptor, indicating a certain transfer efficiency (Jares-Erijman and Jovin, 2003). The rate of energy transfer depends on the extent of spectral overlap, the relative orientation of donor and acceptor transition dipoles and the distance between donor and acceptor. The transfer efficiency varies with the 6th power of the distance between acceptor and donor. RET senses conformational changes and interactions of cellular factors and has been successfully applied to biomedical diagnostics (Lakowicz, 2006; Hink et al., 2002).

Another spectroscopic approach takes advantage of photoinduced electron transfer (PET), which is very short-ranged and even capable to diagnose distances in the picometer range. In PET, a complex between the electron donor and the electron acceptor is formed after excitation and the transfer of an electron from donor to acceptor. This charge transfer complex can return to the ground state without the emission of a photon (Lakowicz, 2006).

Obviously, the spectroscopic approaches do not provide the exact coordinates of the involved partners. With the aid of fluorescence correlation spectroscopy (FCS), diffusion of molecules, ligand-macromolecule binding, molecule clustering, rotational diffusion, internal macromolecule dynamics, intersystem crossing and excited-state reactions can be investigated in solution as well as in living cells (Schwille et al., 1999).

The confocal microscope as described by *Minsky* in the year 1957 was another milestone enabling for the first time optical sectioning and therefore three-dimensional reconstruction of whole cells (Minsky, 1957). In contrast to wide field techniques, where the specimen is illuminated homogeneously, the specimen is scanned point by point by a laser, and the fluorescence light which is not originating from the focus is removed by a pinhole. The resolution in the axial direction is around 500 nm and by a factor of three smaller than the lateral resolution. Featuring single molecule sensitivity, the confocal microscope has become the gold standard for biological imaging and spectroscopic and analytical applications, (Nie et al., 1994).

Another strategy to overcome the limited sensitivity and spatial resolution of conventional fluorescence microscopy due to out of focus and scattered fluorescence is the application of multi-photon microscopy (MPM). MPM is based on molecular excitation by multi-photon absorption and is usually combined with laser-scanning microscopy (LSM) (Denk et al., 1990). The excitation is almost entirely confined to the high intensity region near the focal point because of the superlinear character of the multi-photon excitation of the fluorophores.

The background is therefore significantly decreased. No confocal spatial filter is required because excitation of fluorescence outside the focus is highly improbable. The probability of excitation scales with the *n*-th power of intensity, where *n* denotes the number of photons involved. Advantages compared to confocal microscopy are reduced photodamage and photobleaching in out-of-focus regions and the superior penetration depths provided by the infrared light employed here. MPM was successfully applied to vital imaging of biological systems, especially to high resolution imaging inside highly scattering brain tissue *in vivo* (Denk et al., 1994). However, in terms of resolution, the MPM cannot surpass the conventional one-photon excitation, since the doubled or tripled excitation wavelength in MPM cancels out the effect of smaller effective focal volumes due to quadratic or cubic excitation probability (Kastrup et al., 2005).

In the recent years, every endeavour has been made to increase the resolution in the axial direction. The most prominent candidates which arose from these efforts were the I^5M and the 4Pi techniques (Gustafsson et al., 1999; Egner and Hell, 2005). The I^5M superimposes counter-propagating, planar waves to generate an interference pattern, the aperture enhancement is only implemented for the detection. If a sufficiently small fluorescent object is scanned through the standing wave, it is detected as a narrow main maximum with axially shifted side maxima. The side maxima are then mathematically removed by a deconvolution algorithm. However, the reconstruction of three-dimensional I^5M data is challenged by very prominent side maxima. In 4Pi microscopy, two objectives with a high numerical aperture are used to coherently superimpose the excitation and the fluorescent light. Compared to the I^5M technique, the excitation is performed by focused light. Two spherical wave caps are superimposed rendering the side lobs significantly smaller. According to *Abbe*, the application of two objectives leads to a doubled cone angle and therefore pushes diffraction to its limit. For reliable deconvolution, the side maxima are decreased further by two-photon excitation. The applicability of 4Pi to living cells was demonstrated with an axial resolution of 80 nm (Gugel et al., 2004).

Likewise motivated by insufficient resolution for a multitude of biological problems, optical near field methods were developed and successfully applied. In total internal reflection (TIRF) microscopy, the evanescent field generated directly above the glass surface excites fluorescent molecules up to an axial depth of approximately 100 nm creating one, very thin optical section. A light beam, incident on an interface separating two regions of different refractive indices, is reflected totally if the incident angle exceeds the critical angle. Quantum mechanics calls for a portion of light which penetrates into the distal phase. This is called the evanescent wave; its strength decays exponentially (Pawley, 2006). Another method which is not based on probing the sample with focused light and therefore not subjected to the diffraction limit is scanning near field optical microscopy (SNOM). The trick here is to use a nano-sized tip featuring a light-emitting aperture much smaller than the wavelength of the light coupled into the tip. Light passing through the aperture illuminates the sample which is placed in its near field at a distance much closer than the wavelength. The resolution is then directly determined by the dimension of the point-like source, and is typically around 50 to 100 nm (Lewis, 1984; Pohl, 1984). All methods based on optical near fields are however restricted to surfaces limiting their applicability. Similar arguments apply to the more recent and intriguing concept of imaging with a material of negative refractive index (Pendry, 2000). The need to collect non-propagating waves requires the sample to be placed on top of the material (Podolskiy and Narimanov, 2005).

All of the so far mentioned methods have addressed specialized problems, but none of them tackled the fundamental problem itself, namely the diffraction limit. A genuine breakthrough was accomplished in the year 1994. The idea to establish and control two states of a fluorescent molecule, namely a fluorescent and a non-fluorescent state, during image formation led to a new formulation of *Abbe´s* law which had been a paradigm ever since (Hell and Wichmann, 1994). The resolution in all spatial directions is thus no longer limited by diffraction. The general concept behind subdiffraction resolution is called reversible saturable optical fluorescence transition RESOLFT (Hell, 2003). The most prominent representative of RESOLFT is stimulated emission depletion (STED) microscopy. In STED microscopy, the fluorophores are excited by a *Gaussian* beam and the fluorescence is quenched by a second, doughnut-shaped beam featuring a zero in the center. Only those fluorophores located right at the zero are not influenced by the signal suppression beam and remain therefore in the fluorescent state. In theory, the zero can theoretically be confined to an infinitely small point by increasing the power of the STED beam. A recent example demonstrating the power of STED microscopy in terms of live cell compatibility was the dissecting of synaptic vesicle movement at video rate by Westphal et al., 2008.

Instead of the targeted read-out used in STED microscopy, it is also possible to read out the image information stochastically and determine the centroid of the isolated fluorescence spot. This is realized in photo-activated localization microscopy (PALM) or stochastic optical reconstruction microscopy (STORM) (Betzig et al., 2006; Rust et al., 2006). However, the common denominator of all these nanoscopic techniques is to read out the fluorescent signals sequentially within a volume defined by diffraction. The combination of both, “point spread function engineering” as applied in 4Pi or STED microscopy on the one hand and “dark state engineering” (applied in STORM- or PALM-related techniques) on the other hand, will result in a highly promising tool for ultra resolution. The ultimate goal is to provide a tool for cell biology allowing to create a quantitative map of different cellular compartments and factors in living systems with unprecedented resolution to establish new, empirical based models of life.

The limited number of emitted photons actually collected by a microscope is a general problem, no matter whether it is restricted by dye properties, photobleaching, detectors and/or optics. If the photon count is below the noise level, an image can not be recorded. In the mid of the 90´s, it was by far not obvious to what extent principles like STED were applicable, since nanoscopy places high demands on fluorescent labels and sample embedding. The dyes have to exhibit two states, a bright “signal-giving” and a “dark” state, and the switching between these two states should be manipulable and robust. STED microscopy for example takes advantage of the non-linear process of fluorescence quenching by stimulated emission to confine the origin of fluorescence to a subdiffraction area. The higher the intensity of the signal suppression (STED) beam, the stronger the confinement. On the other hand, those subdiffraction techniques based on stochastical readout of single molecules rely on a high number of detected photons from each single molecule in order to determine the coordinates of the fluorescent molecule with high accuracy. To gather high photon counts in a reasonable time, it is necessary to apply high excitation light intensities. The subdiffraction microscopy approaches are highlighted in *chapter 2*. In either case, high excitation light or high signal suppression intensities are connected to higher photobleaching, limiting the number of detected photons, as described in *chapter 2*. Photostability and the switchability between two states has to be maintained during the data acquisition, otherwise subdiffraction imaging is hindered. The dyes available till the 90´s were not optimized or screened for photostability, switching or fluorescence depletion processes necessary for subdiffraction imaging. Today, subdiffraction images can be recorded due to a consequent improvement of dye properties over the last years. But there still is plenty of room for improvements, especially if very high resolutions are desired, fast image series are to be recorded to capture dynamical processes, three dimensional information should be gathered, or for further simplification. A lot of improvements are connected to photobleaching or more generally to the overall number of collected photons. To increase the number of collected photons with a subdiffraction microscope, all possibilities have to be exploited. Solutions can be provided by biology, physics and chemistry. Biological approaches include for example enzyme systems to remove oxygen which can be responsible for photobleaching, or advancements in the field of fluorescent proteins. The approaches offered by chemistry are besides developments in the field of fluorescent dyes itself, special embedding media, substances to prevent photobleaching and “dark state engineering”. Physical approaches can provide new detectors, flexible setups and adaptive filters to better match dyes with improved properties and to exploit the entire emission spectrum. Furthermore, applications of new molecular processes for subdiffraction imaging and adaptive light exposure help to decrease photobleaching. The aim of this thesis is the evaluation and development of chemical and physical approaches for minimizing photobleaching, phototoxicity and dark state transitions in subdiffraction microscopy. The results and discussions are therefore divided into *four* parts, resembling different physical and chemical approaches to tackle photobleaching:

1) In *Chapter 3*, an optical setup is described, which is characterized by high flexibility. It allows one to easily adapt to new fluorophores with enhanced properties and alternative laser lines for RESOLFT experiments. A flexible system requires a tunable dichroic mirror, an adaptive emission and excitation filter system and a tunable phase filter to generate a zero in the STED beam. Solutions to all these points are addressed in *Chapter 3*. As a result, the whole emission spectrum of a dye can be exploited leading to an increased signal-to-noise ratio (SN) and the chance to reduce the excitation intensity and thus photobleaching. The requirements for the spectral filter sets are heavy, when intense signal suppression beams are applied to enhance the resolution. In STED microscopy, the wavelength of the signal suppression beam inevitably is part of the fluorescence spectrum. An adaptive notch or bandpass filter to remove intense signal suppression light is described in *Chapter 3*, replacing thin film interference filters with fixed spectral properties. Additionally, a new phase plate approach significantly simplifies the alignment procedure. The spectral adaptive filter system consists of a quadruple AOTF arrangement and a prism based spectrometer.

2) The quadruple AOTF arrangement allows for the complete control of the sample exposure which is a basic requirement for a method introduced in *chapter 4*. This approach reduces the number of excitation and signal suppression cycles in zero based high resolution methods using metastable off-states (RESCue) and therefore prevents photobleaching and dark state transitions by adaptively controlling the light dose on the fluorescent sample without sacrificing localization information. The efficiency is exemplarily demonstrated on STED microscopy which is the first and most prominent candidate among all subdiffraction microscopy techniques. RESCue takes the high resolution information itself as a basis to locally adapt the sample exposure and therefore significantly reduces the photobleaching even compared to the standard confocal imaging mode. The common opinion, that high resolution microscopy is always connected to higher bleaching, now has to be reconsidered.

3) The development of new fluorophores is a highly active field. The high requirements placed by nanoscopic techniques is challenging the fluorophore development, as mentioned above. The screening for new, photostable and bright dyes suitable for high resolution techniques led to the discovery of a new mechanism for signal suppression. Direct light-driven modulation of fluorescence from quantum dots (QD) is described in *chapter 5*. The mechanism for fluorescence modulation relies only on internal electronic transitions within Mn-doped ZnSe quantum dots (Mn-QDs). It is demonstrated that the QD fluorescence can be reversibly depleted with efficiencies of more than 90%, using continuous-wave (cw) optical intensities of ~1.9 MW cm^{-2}. Time-domain measurement during modulation indicates that the number of fluorescent on-off cycles exceeds 10^3 before significant loss of fluorescence quantum efficiency occurs. Such robust nanometric probes having remotely controllable optical transitions are useful in many areas of research, and in particular, in far-field nanoscopy based on RESOLFT. Consequently, it can be shown that implementation of Mn-QDs for imaging leads to an increase in resolution over standard confocal microscopy by a factor of 4.4.

4) Matching the refractive index of the sample to that of the immersion system is a crucial step to avoid a blurred focal spot. A refractive index mismatch reduces the signal-to-noise ratio (SN) and calls for compensation by higher excitation intensities resulting in higher photobleaching. On the other hand, subdiffraction imaging deeply inside the specimen is hindered due to spherical aberrations and stray light caused by refractive index mismatch.

In *chapter 6*, a novel mounting medium whose refractive index can be continuously tuned between that of water and that of immersion oil is described. This medium is not only cost-effective but also enables a flexible use of all available immersion lenses, including the novel oil immersion lenses with an ultrahigh aperture angle $\alpha = 75°$ and thus renders subdiffraction imaging deeply in biological samples feasible. Of vital importance is the water solubility of the new high refractive index embedding medium, simplifying the embedding process. Additionally, the embedding media itself exhibits good anti-oxidant properties and can therefore act as an antifade in high concentrations.

Chapter 2

Theory

2.1 Fluorescence

All subdiffraction microscopy approaches to date rely (although not mandatory) on the manipulation of fluorescence processes and the detection of fluorescence photons. The photophysical principles underlying fluorescence emission are therefore summarized here.

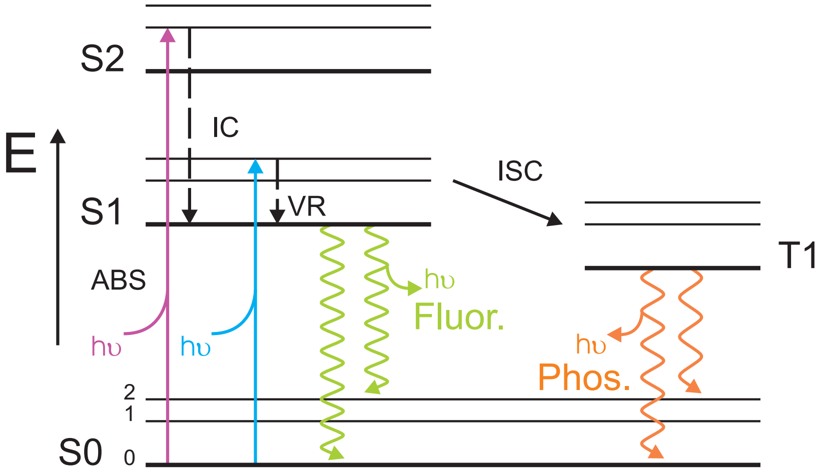

Fig. 2.1: The *Jablonski* diagram describes the most important processes taking place in a fluorescent dye. *ABS* denotes the absorption of a photon and instantaneous transition from the groundstate (*S0*) to higher excited singlet states (*S1*, *S2*). *IC* describes internal conversion (radiationless transitions between states of the same spin multiplicity), *VR* is the vibrational relaxation of higher vibrational states within an electronic state into the lowest vibrational state, *ISC* denotes intersystem crossing i.e. radiationless transitions between states of different multiplicities (spin-forbidden) (from *S1* to the triplet state *T1*, for example). The transitions involving photon emissions (luminescence) are called fluorescence (*Fluor.*, states with the same multiplicity involved) and phosphorescence (*Phos.*, states with different multiplicities are involved). Phosphorescence is a spin-forbidden process, therefore the triplet state *T1* features a 1000 times longer lifetime compared to the *S1* state. The channels responsible for photobleaching are described later (Fig. 2.6). Modified from Lakowicz, 2006.

A fluorescent molecule can be excited from the electronic ground state to higher electronic states by electromagnetic radiation, if the electric dipole moment of the dye is not perpendicular to the electric field of the radiation. The *Franck-Condon* principle states that the nuclei framework of the dye is not affected by the excitation which takes place on femtosecond time scales. The higher the overlap of the two wave functions describing the dye before and after the excitation, the more probable is the transition (*Franck-Condon* factors). A fluorophore is usually excited to some higher vibrational level of either *S1* or *S2* by light featuring a wavelength according to $\lambda = hc / \Delta E$. ΔE denotes the energy spacing between the involved states. Molecules in the higher excited state (*S2*) relax radiationless (internal conversion, *IC*) to the lowest vibrational level of *S1* within picoseconds which is according to *Kasha´s* rule the origin of a radiation transit called fluorescence. Fluorescence is a transition between states with same spin multiplicity and therefore allowed. The radiation decays exponentially in the nanosecond time scale. The fluorescence photon has a longer wavelength compared to the excitation photon, a phenomenon called *Stokes* shift. Molecules in the *S1* state can alternatively undergo a rather infrequent spin conversion to the first triplet state *T1*. Emission from *T1* is termed phosphorescence and is generally shifted to longer wavelengths relative to the fluorescence. Conversion of *S1* to *T1* is called intersystem crossing (*ISC*). Transitions from *T1* to *S0* are spin-forbidden, the lifetime of triplet states is therefore in the range of microseconds up to hours. All the radiation and radiationless processes can be summarized in the *Jablonski* diagram (Fig. 2.1).

2.2 Microscopy at and beyond *Abbe´s* diffraction limit

The STED microscope featuring enhanced spatial resolution is typically based on a confocal microscope to discriminate the desired signal from *Rayleigh* and *Raman* scattered light as well as from fluorescence which is generated out of focus. The key principle to suppress the background is to reduce the detection volume. Since many of the experiments described in this thesis are preformed in the STED mode, the confocal microscope and its underlying principle is briefly reviewed here. For more in-depth information see Wilson, 1990; and Pawley, 2006.

In the year 1873, *Ernst Abbe* recognized that the resolution of an optical microscope can not be arbitrarily improved but is, in contrast, fundamentally limited. Besides the so-called diffraction limit, he also identified the conditions needed to design an objective lens which is only limited by diffraction rather than limited by chromatic and spherical aberrations (Abbe, 1873; Abbe, 1884). That time, the influence of the objective´s numerical aperture (*NA*) on the image resolution was found to be of crucial importance. The image of a point-like source in the focus is itself not infinitesimal small, but rather a circular *Airy* diffraction image with a central bright disk surrounded by progressively weaker concentric dark and bright rings. The intensity distribution of the focused light in the focal plane $h(\vec{r})$ is called the point spread function (PSF). The PSF is given by the squared field amplitude $E(\vec{r})$ which is according to the scalar diffraction theory given by (Born and Wolf, 1999):

$$h(\vec{r}) = |E(\vec{r})|^2 = E_0 \int_0^{\alpha} \sqrt{\cos\theta}\, \sin\theta J_0(k\sqrt{x^2+y^2}\,\sin\theta)\, \exp(ikz\cos\theta)\, d\theta \qquad (2.1)$$

where $\vec{r} = (x, y, z)$ describes the spatial coordinates in object space, E_0 is a constant which scales with the incident optical power, α denotes the half-cone angle of the lens, θ is the integration variable, $J_0()$ is the zero order Bessel function of the first kind, n is the medium´s refractive index and $k = 2\pi n / \lambda_0$ and λ_0 are, respectively, the wave number and the vacuum wavelength of the focused light.

The resolution of a microscope is defined by half the diameter of the *Airy* disk according to the *Rayleigh* criterion. The *Airy* disk itself is given by the diameter of the first minimum of the PSF ($h(\vec{r})$) enclosing the main maximum as a dark ring. For the epifluorescence microscope, the diameter of the *Airy* disk is given by :

$$\Delta x = 1.22\frac{\lambda_0}{NA}. \tag{2.2}$$

where $NA = n * sin\alpha$ denotes the numerical aperture of the lens. The *Airy* disk in axial direction exhibits a separation of the minima on both sides of the maximum by (Wilson, 1990):

$$\Delta z = 4.00\frac{n\lambda_0}{NA^2}. \tag{2.3}$$

Alternatively, the full-width at half-maximum (FWHM) of the PSF is often determined to characterize the optical resolution of a microscope. In the frequency domain, the counterpart of the PSF is the optical transfer function (OTF), which is related to the PSF via a simple *Fourier* transform. Here, the optical resolution is described as the transmittance of the instrument as a function of spatial frequency. If small features are imaged, high spatial frequencies are required. A circular aperture for example reduces the amplitude of the OTF with increasing spatial frequency. Therefore, the most limiting aperture in the system, which is usually the *NA* of the objective lens, determines the resolution. Enhancing the resolution is thus equivalent to widening up the support of the OTF (Born and Wolf, 1999; Gu, 1999).

2.2.1 Confocal microscopy

The confocal microscope allows to section the sample optically and reconstruct three-dimensional (3D) images. This is the main advantage of a confocal microscope compared to an epifluorescence microscope. The principle of the discrimination along the optical axis (z) can be explained from the schematic drawing of a confocal microscope as depicted in Fig. 2.2.

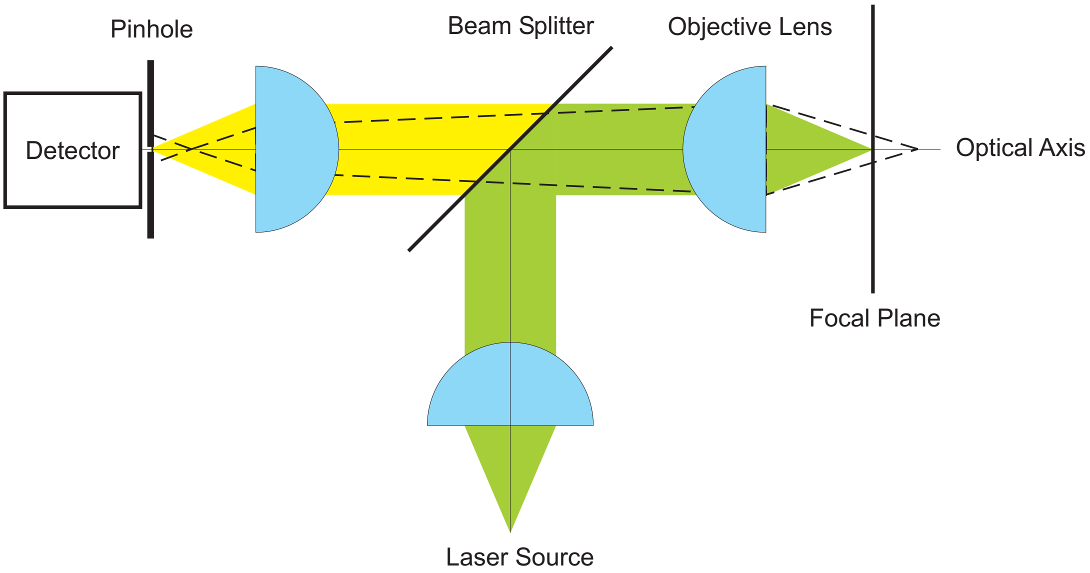

Fig. 2.2: Operating principle and main components of a confocal microscope.

A point-like source, e.g. a laser focused through a micrometer-sized pinhole or emitted from the end of a single-mode optical fibre, is collimated by a lens, reflected by a dichroic mirror and focused into the sample via an objective lens. The fluorescence signal emitted by the sample is usually collected by the same objective lens, passes the dichroic mirror to be separated from the excitation light and is focused through a pinhole onto the detector. The focused, cone-like excitation beam exhibits non-vanishing intensities above and below the focal plane. A signal which is generated outside the focal plane will not be focused through the pinhole and is therefore not detected, but suppressed due to beam divergence or convergence as shown by the dotted beam path in the drawing. As described by the alternative beam path of light originating outside the focal plane, the detection pinhole is responsible for the discrimination in the optical axis (z).

Because beam paths are reversible, the detection pinhole can theoretically be imaged into sample space and then further towards the point-like light source. The two pinholes have corresponding foci within the sample (*con*focal). Hence, the effective PSF of the confocal microscope is given by the product of the excitation PSF $h_{exc}(\vec{r})$ and the detection PSF $h_{det}(\vec{r})$. In reality, the detection pinhole is not point-like but has a finite diameter. The detection PSF therefore has to be convolved with a pinhole function

$$o(\vec{r}) = \begin{cases} 1, if \sqrt{x^2 + y^2} < d/(2M) \\ 0, else \end{cases} \tag{2.4}$$

describing the detection pinhole with a given diameter d projected into the focal space. M denotes the magnification of the microscope. The effective confocal PSF is then given by:

$$h_{conf}(\vec{r}) = h_{exc}(\vec{r})\left[h_{det}(\vec{r}) \otimes o(\vec{r})\right]. \tag{2.5}$$

The product of both similar PSFs results approximately in a quadratic suppression of out-of-focus light. This ensures an axial resolution determined by the confocal spot size of about the wavelength.

2.2.2 Subdiffraction fluorescence microscopy

Basic idea

The methods to discern subdiffraction features discussed in this thesis are STED and RESOLFT microscopy. As STED is part of the more general RESOLFT concept, the fundamental ideas behind RESOLFT should be discussed first (Hell, 2007).

In the mid 90´s the first concrete and feasible concepts emerged showing that the diffraction limit can be broken even in the far field with propagating light by regular lenses (Hell and Wichmann, 1994; Hell and Kroug, 1995). The fundamental idea behind these concepts is the application of the fluorescent dye´s different molecular states not only for fluorescence generation but also for overcoming the limit dictated by diffraction. The diffraction limit *per se* has not been eliminated (Hell, 1994).

The separation of fluorescence signals which differ in absorption or emission spectra, polarization, or fluorescence lifetime is not challenged by diffraction and hence the different signals can be read out one after the other (Betzig, 1995; van Oijen et al., 1999). The coordinates of the fluorescence molecules can be determined with arbitrary precision down to 1 nm depending on the number of detected photons by identifying the centroid of the separated signals (Kural et al., 2005). The scheme depicted here is not governed by *Abbe´s* barrier, as long as there is no other molecule of the same type within the diffraction-limited focal volume, but it gives a first glance on how to break it. Breaking *Abbe´s* limit means discerning features which are labelled by the same type of fluorescence markers within the diffraction-limited volume. For that, the signals have to be recorded sequentially e.g. by successively transferring (one of) the markers of each feature to a signal giving bright "on" state while keeping the other markers in the dark "off" state (Hell, 2003; Hell et al., 2003). By reading out the bright fluorescent molecules together with the knowledge of their coordinates, the subdiffraction image can be assembled (Fig. 2.3). The most direct way to determine the coordinates of the bright markers is to define their location r_i.

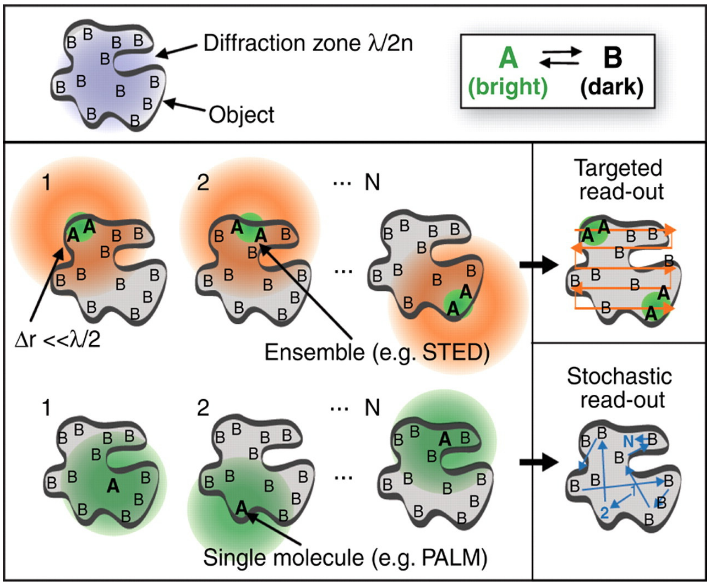

Fig. 2.3: Difference of targeted and stochastic read-out of the fluorescence labels of a nanostructure within the diffraction zone with a diameter of *λ/2n*. In the targeted read-out one of the two states (here **A**) is established within the subdiffraction-sized region at the zero. The image is assembled by scanning the zero across the structure and reading out the bright markers. The zero can also be a groove or a multiple set of zeros can be used for parallelization. In the stochastical read-out approaches, a single switchable fluorophore at a random position within the diffraction zone is switched to a bright state **A** by low intensity activation light, while the other molecules remain in **B**. The coordinate is determined by the centroid of the diffraction-limited spot on a pixelated detector. After switching of the bright fluorophore (**A→B**), another fluorophore is randomly switched on and read out. After a certain time, a sufficient number of fluorophores have revealed their position and are summed up to form an image (from Hell, 2007).

This can be realized by forcing an optical transition **A→B** everywhere except at r_i, to ensure that all molecules are converted to the dark state except those present at r_i. The optical transition can be implemented by a light intensity distribution $I(r)$ featuring an intensity zero at position r_i. Driving **A→B**, this intensity $I(r)$ must produce a rate $k_{AB}(r) = \sigma I(r)$ that outperforms competing spontaneous rates basically everywhere except at r_i. The spontaneous rates are given by the inverse of the lifetimes $\tau_{A,B}$ of the involved states **A** and **B**, and σ

denotes the optical cross section of the transition. The possible occurrence of the on state **A** is therefore confined to $r_i \pm \Delta r / 2$ with Δr being significantly smaller than the diffraction limit when an intensity of $I(r) >> (\sigma\tau)^{-1} = I_{sat}$ is applied (Fig. 2.5c). The region r_i gets even more confined with increasing intensity $I(r)$. The saturation intensity I_{sat} is a measure of the intensity needed to even outperform the spontaneous rates. By probing the diffraction-limited volume with the confined Δr, the signal of all markers is inhibited except those which are present at $r_i \pm \Delta r / 2$ leading to a sequentially read-out of neighbored features with a resolution of Δr (Hell, 2003; Hell 2004). This can be parallelized by scanning multiple zeros across the sample and detecting the fluorescence with a camera (Hell, 2003).

In contrast to the above-mentioned scheme, which consists of applying markers of different spectroscopic properties simultaneously for subdiffraction imaging, the ground breaking idea here is to read out the information sequentially by successive manipulation of the markers, rendering them distinguishable. The markers do not have to feature different spectroscopic properties *per se*.

RESOLFT

STED and ground state depletion (GSD) (Hell and Kroug, 1995) microscopy are representatives of the zero-based time-sequential read-out methods which have been generalized under the acronym RESOLFT (Hofmann et al., 2005). Another concept exploiting reversible saturable or photoswitchable transitions is saturated pattern excitation microscopy (SPEM) (Heintzmann et al., 2002; Gustafsson et al., 2005). Their resolution can be described by:

$$\Delta r \approx \frac{\lambda}{2n \sin\alpha \sqrt{1 + I_{max} / I_{sat}}} \tag{2.6}$$

with I_{max} denoting the intensity of the zero featuring signal suppression beam. The striking difference to *Abbe´s* equation is the introduction of the term I_{max}/I_{sat}, which can become infinite resulting in a resolution only dependent on the fluorophore´s molecular size (1 nm). The square root factor originates from the parabolic approximation of ordinary intensity zeros in space. Although the RESOLFT concept is capable of resolving single molecules (Westphal et al., 2005), it is conventionally applied to molecular ensembles. The size of Δr and, connected to that, the average number of simultaneously recorded fluorescent molecules can be tuned by the ratio I/I_{sat}. The resolution is ultimately dependent on the quality of the zero, photobleaching, the available laser intensity and the choice of the states **A** and **B** influencing I_{sat}. **A** and **B** can include electronic states like *S0*, *S1* (Singlet), *T* (Triplet) and dark states, or conformational states directly affecting the fluorophore and states with different separations of FRET partners or quenchers, or binding and temporarily immobilized states. Besides "PSF engineering" providing zero patterns or confined PSFs in *z* direction, "dark state engineering" became a crucial discipline for subdiffraction microscopy (Steinhauer et al., 2008).

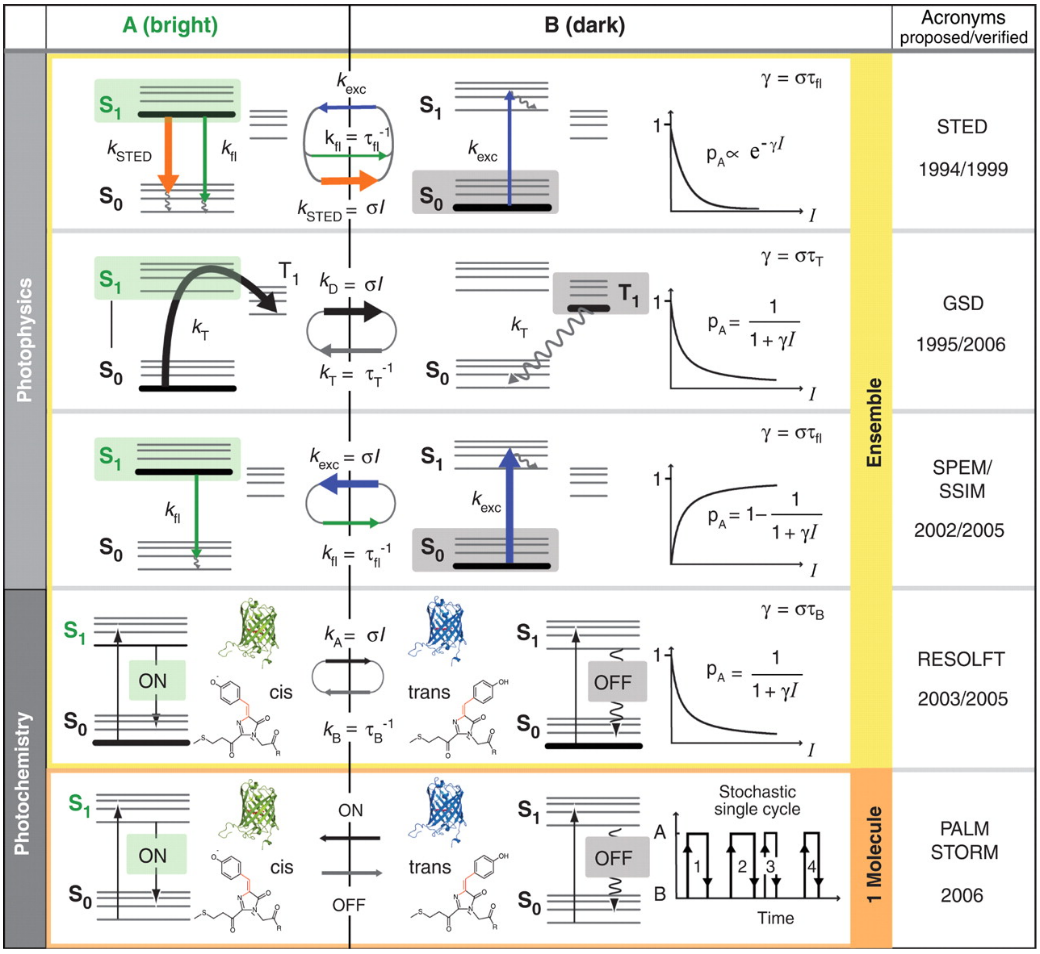

Fig. 2.4: Bright (**A**) and dark (**B**) molecular states used to break the diffraction barrier. A classification can be made depending on whether photophysical transitions (STED, GSD, SPEM, GSDIM, ESA) or photochemical transitions are involved, where atoms are relocated or molecules isomerised (RESOLFT, PALM, STORM, dSTORM). PALM, STORM dSTORM and GSDIM are based on single molecule detection, whereas the other concepts (although compatible to single molecule imaging), principally read out ensembles. Ensemble techniques require reversible transitions between **A** and **B**, as indicated by the rates *k*. The probability p_A of being in state **A** depends nonlinearly on the light intensity applied, as indicated by the equations, ensuring that either **A** or **B** is confined to a subdiffration area at a targeted coordinate in space. The $e^{-\gamma I}$ and the $(1+\gamma I)^{-1}$ dependence entail nonlinearities of infinite order $(\gamma I)^m$; $m \rightarrow \infty$. The higher the lifetime of the chosen state, the more the nonlinear dependence of p_A is strengthened by γ. Huge nonlinearities at low intensities *I* are enabled in that way (in contrast to m-photon processes, which are practically limited to I^m; $m<4$). Because PALM, STORM, dSTORM and GSDIM are dealing with single molecules in a known state, the probability concept is not suitable. The resolution is dependent on the number *N* of collected photons per molecule (from Hell, 2007).

STED microscopy

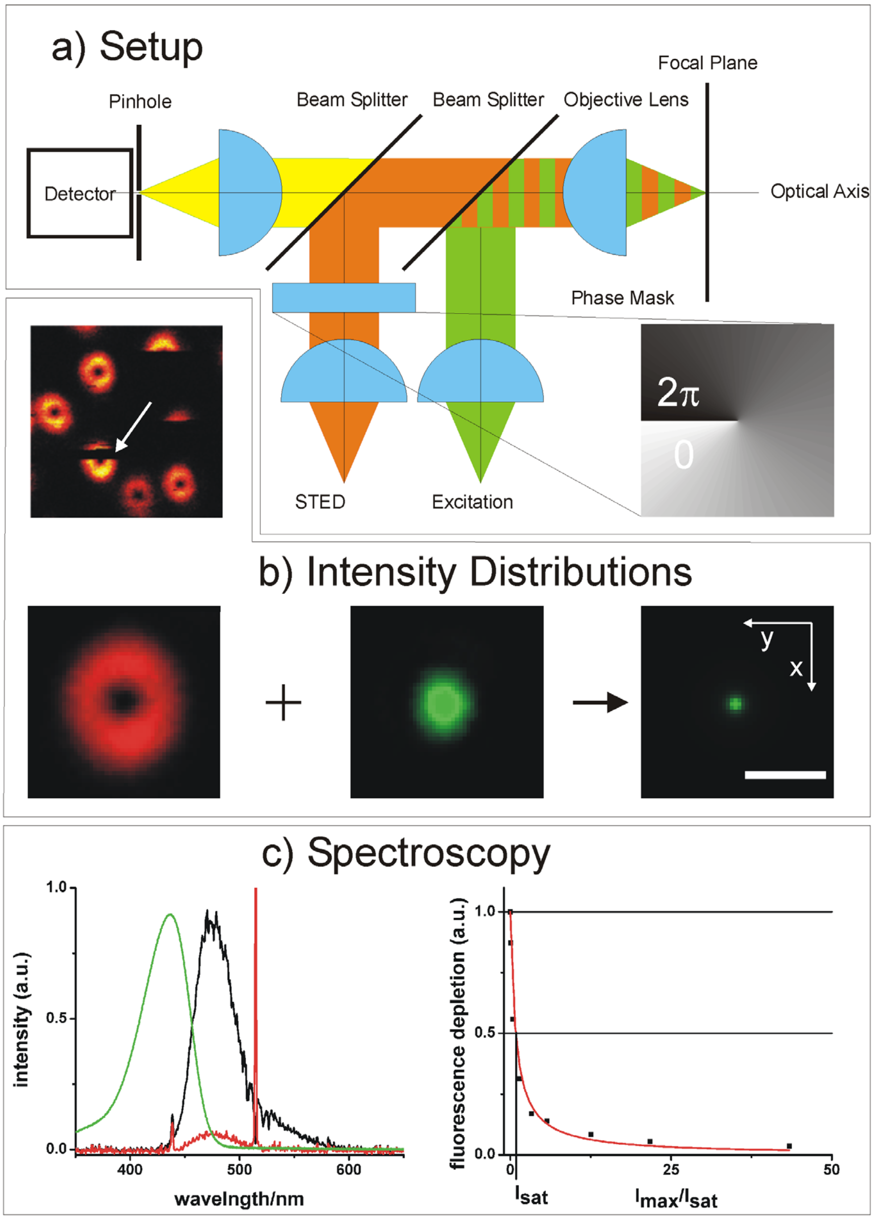

Fig. 2.5: Main components and operating principle of a STED microscope (**a**). PSFs probed by detecting light scattered from gold beads by the excitation (green) and the STED (red) beam respectively, if a vortex-type phase plate is used (**b**). The resulting effective PSF is significantly reduced in size (scale bar: 500 nm). The PSF can also be measured with quantum dots (QD705), fluorescent at 705 nm. The blinking which is typical for quantum dots can be seen (arrow). Absorption (green) and emission (black) spectrum of a fluorescent dye (**c**). The STED wavelength (514 nm, spike) is located within the red end of the fluorescence spectrum. Applying high STED intensities leads to fluorescence emission depletion demonstrated by the significantly reduced fluorescence intensity (red). A measurement of depletion efficiency with regard to the STED intensity can be seen on the right side.

STED microscopy, which is the first concept of the RESOLFT family, uses the *S0* and the *S1* state as **B** and **A** respectively (Fig. 2.4). The fluorescence molecules are excited by a focused beam and the fluorescence signal is quenched by a second, red-shifted, doughnut-shaped beam due to stimulated emission *S1*→*S0* (Fig. 2.5c). The STED beam is exactly aligned with the excitation beam (Fig. 2.5a). Generally, pulsed laser sources are used to perform STED experiments. The excitation pulse (100ps) excites the molecules which are subsequently relaxing vibrationally within a few picoseconds (Fig 2.4). After the transition of the molecules to the vibrational ground state of the excited singlet state, the synchronized STED pulse (several 100 ps) quenches the fluorescence by stimulated emission. However, the excitation and STED process can also be carried out in cw mode, making an elaborate pulse synchronization redundant (Willig et al., 2007). The few stimulated photons have the same properties as the photons in the STED beam and are removed by the filter system. To confine the fluorescence to the zero of the doughnut-shaped PSF, fluorescence quenching must outperform the spontaneous decay of the *S1* given by the inverse fluorescence lifetime $\tau_{fl} = 1\text{ns}$. $I_{sat} = 1/(\sigma\tau)$ typically amounts to $3*10^{25}/\text{cm}^2\text{s}$, i.e. 10MW/cm^2 with $\sigma = 10^{-16}/\text{cm}^2$. Increasing the intensity above I_{sat} leads to a confined fluorescence-emitting volume which is scanned across the sample to map out subdiffraction features.

Mathematically, the four level system consisting of *S0*, *S1*, and the vibrational excited states S_{vib0} and S_{vib1} can be modeled by a set of four differential equations (for a detailed description see (Dyba et al., 2005)). The population of the excited state level *S1* immediately after the STED pulse can be approximated by:

$$N_{S1} \approx N_0\, exp(-\sigma_{STED} I_{STED}) = N_0 \eta(I_{STED}) \tag{2.7}$$

η is called the STED suppression coefficient, since it describes the amount of fluorescence inhibition. Such experimental depleting curves can be directly measured (Fig. 2.5c) and determine the performance of the fluorescent dye under STED conditions, hence the performance of the STED microscope. The most important aspect of Eq. (2.7) is the strong nonlinear dependence of the remaining fluorescence on the STED intensity I_{STED}, hence creating the saturation behavior (Fig. 2.5c).

To generate a zero-containing focus, several techniques are conceivable. A technically simple implementation is to position a properly designed phase retardation filter into the expanded STED beam in a conjugated back focal plane of the objective lens (Fig. 2.5a). The phase filter spatially modifies the phase front of the STED beam. As an example, by placing a vortex-type phase filter into the beam and thereby introducing a continuous phase shift from 0 to 2π clockwise within the area of the back aperture of the objective lens, the intensity distribution shown in Fig. 2.5b is obtained after focusing, which features a ring- or doughnut-like maximum enclosing the central minimum or zero. Here, the fluorescence is only confined in the focal plane and not in the optical axis. The calculation of the intensities in the focus requires the consideration of the vectorial properties of light for high *NAs*. Applying the *Debye* integral for linearly polarized illumination with a polarization angle ϕ_0 in respect to the x axis, the intensity distribution in the focal region (PSF) of an aplanatic lens can be calculated as follows (Klar et al., 2001):

$$h^{\kappa}(\vec{r},t)=\frac{cn\varepsilon_0}{2}\left|\vec{E}^{\kappa}(\vec{r},t)\right|^2=\frac{cn\varepsilon_0}{2}\left|\begin{pmatrix}E_x^{\kappa}\\E_y^{\kappa}\\E_z^{\kappa}\end{pmatrix}\right|^2=\frac{n^3c\varepsilon_0}{2\lambda^2}\left|\begin{array}{l}\int_0^{\alpha}\int_0^{2\pi}E_0^{\kappa}(\theta,t)\sqrt{\cos\theta}\,\sin(\theta)\exp\{i[\Psi^{\kappa}(\theta,\phi)+ks-kf]\}\\ \times\begin{pmatrix}\cos^2(\phi-\phi_0)\cos(\theta)+\sin^2(\phi-\phi_0)\\ \sin(\phi-\phi_0)\cos(\phi-\phi_0)[\cos(\theta)-1]\\ -\cos(\phi-\phi_0)\sin(\theta)\end{pmatrix}d\phi d\theta\end{array}\right|^2 \tag{2.8}$$

The superscript κ = *exc* or *STED* stands for the excitation or STED beam, respectively. $\vec{E}^{\kappa}$ denotes the electric-field amplitude, c the speed of light, ε_0 the permittivity of free space, f the focal length of the lens, ϕ the azimuth angle, and θ the polar angle of the aperture, with $0 \le \theta \le \alpha$. The angle α is the half-aperture angle and $E_0^{\kappa}(\theta,t)$ is the wave front amplitude at the entrance pupil of the lens. The phase $\Psi^{\kappa}(\theta,\phi)$ denotes any arbitrarily induced phase change across the wave front; it equals zero if the wave front is planar (in the back focal plane), as it is the case here for excitation. s is the path traveled by the light from the point on the converging spherical wave front with the coordinates $[f,\theta,\phi]$, to the position r in the focal region. The focal point is located at $\vec{r} = [0,0,0]$. λ is the vacuum wavelength and $k = 2\pi n/\lambda$ the wave number with n being the refractive index. For any given $\Psi^{\kappa}(\theta,\phi)$, Eq. 2.8 can be evaluated numerically.

Recent achievements in STED microscopy

The zero does not have to be formed by a doughnut, but can also be established by one or more grooves which are part of an interference pattern (Westphal et al., 2005; Schwentker et al., 2007). The point-like detector is then replaced by a CCD camera. Furthermore, there are not only phase plates providing a zero in the focal plane but also along the optical axis with high peak intensities above and below the focal plane. With the help of such a phase plate it was possible to confine the fluorescence to 100 nm in z direction with a single lens (Klar et al., 2000). In combination with a 4Pi system the steepest zero is possible, allowing for a z resolution of 33 to 60 nm (Dyba et al., 2002). Moreover, the application of two lenses in STED-conditioned experiments creates an isotropically confined fluorescence volume of 40 to 45 nm in all dimensions, dissecting sub-λ-sized organelles of cells in two colors and offering co-localization on the nanoscale (Schmidt et al., 2008, Donnert et al., 2007). So far, the highest resolution achieved with a STED microscope of 16 nm has been obtained by imaging single dye molecules as test objects (Westphal et al., 2005). A crucial step to further improve the performance of the STED microscope was the addressing of the more pronounced photobleaching in STED-conditioned measurements. Allowing fluorophore dark states to relax (triplet state relaxation (T-REX)) enabled Δr to be in the range of 20 to 30 nm in fixed biological samples (Donnert et al., 2006). The impact of STED microscopy on cell-biological problems was even more boosted by introducing a fast scanning STED system suitable for subdiffraction life cell imaging. This way, the movement of synaptic vesicles was discerned with a high temporal resolution of 28 frames per second (Westphal et al., 2008). The problem of channeling organic dyes into living cells was circumvented by screening a variety of fluorescence proteins suitable for STED microscopy. Citrine turned out to perform well under STED conditions, shown by nanoscopic ($\Delta r < 50$ nm) recordings of the endoplasmatic reticulum in living cells (Hein et al., 2008). In order to facilitate the widespread adaptation of far field nanoscopy, a versatile, low cost system based on a super continuum source was developed. Using the same source both for excitation and STED, this implementation of STED microscopy avoids elaborate preparations of laser pulses and conveniently provides multicolor imaging. Operating at pulse repetition rates around 1 MHz, it also affords reduced photobleaching rates by allowing the fluorophore to relax from excitable metastable dark states (T-REX) involved in photodegradation (Wildanger et al., 2008).

Alternative subdiffraction microscopy techniques

S0 and *S1* is not the only set of states which can be exploited in the way described in Fig. 2.4. Ground state depletion (GSD) for example requires a 100 times smaller I_{max} for similar performance, because it employs the metastable triplet state *T* with a lifetime τ of 1000 ns to 1000000 ns as **B** and the singlet system (*S0* and *S1*) as **A**. Probing **A** is performed at the same wavelength as its pumping to **B** (Bretschneider et al., 2007).

The ultimate saturable transition is a photoswitch, as the thermodynamically and kinetically stable states and the absence of spontaneous interstate rates result in a very small I_{sat} and hence a huge I_{max}/I_{sat} at low I_{max}. Photoswitching between different isomers, where only **A** yields fluorescence, is found in reversibly photoactivatable relatives of GFP, such as asFP595 and dronpa, and in photochromic synthetic compounds (Lukyanov et al., 2000; Ando et al., 2004; Bossi et al., 2006).

A very important parameter for achieving subdiffraction resolution is the finite number of cycles between **A** and **B**. However, cycling is essential if molecular ensembles are to be read out at targeted coordinates with diffraction limited beams. Reading out **A** at a given coordinate requires nearby molecules to be switched to **B** (Fig. 2.3). In other words, for targeted read-out, one has to accept a higher number of switching cycles. If the molecule´s switching behavior is lost or the dye gets destroyed too quickly during the read-out of nearby molecules, subdiffraction imaging is hindered. In STED microscopy, the state **B** is metastable and has to be maintained. During each switching cycle, there is a certain probability (related to k_{isc}) that the molecule is transferred to the triplet state. This state is a prominent bleaching precursor because of the high lifetime (µs) and the deposited energy. In *chapter 4*, a method will be discussed, which uses the high resolution information to instantaneously adapt the local light dose and to reduce the number of switching cycles in STED microscopy.

Stochastic read-out

The problem of excessive switching cycle numbers is avoided in PALM, STORM and related techniques (Betzig et al., 2006; Rust et al., 2006). Here, single molecules are read out at random coordinates. A single dye is switched on or activated (**B→A**) in a wide field setup, so that the next molecule that is on is farther apart than $\lambda/2n$. It is then repeatedly excited and fluoresces ($\mathbf{A}\leftrightarrow\mathbf{A}^*$) to collect *N* photons forming a diffraction-limited spot on a camera. Switching off neighbored molecules is not needed, because they are off (state **B**) already. With the assumption, that only one molecule per diffraction zone is in state **A**, which is ensured by adjusting the intensity of the activation light, its coordinate can be calculated from the centroid of the spot with a precision of $\approx \lambda/(2n\,sin(\alpha)\sqrt{N})$. The last step is to switch the molecule into state **B´**, which is non-fluorescent. Here, the switching does not necessarily have to be reversible. Another molecule is then switched on, read out, and switched off. Thus, the image is assembled molecule by molecule underlying a single switching cycle ($\mathbf{B}\rightarrow\mathbf{A}\rightarrow\mathbf{B'}$). PALM switches off by bleaching ($\mathbf{B}\neq\mathbf{B`}$), greatly expanding the number of applicable compounds, whereas STORM relies on a true, reversible switch ($\mathbf{B}=\mathbf{B`}$). In both approaches, it is necessary to adapt the intensity to the dye concentrations.

PALM images of thin cryosections of lysosomal transmembrane protein in a mammalian cell displayed a resolution of <20 nm. STORM is based on dye pairs containing a reporter and an activator dye. Due to combinatorial pairing, a broad palette of different labels is available for multicolor applications (Bates et al., 2007). The implementation of a cylindrical lens in front of the objective allows 3D imaging due to the ellipticity of the PSFs dependent on the *z* position of the dye (Huang et al., 2008). The stochastical approaches also allow investigations of dynamical processes in living cells. Nanoscale dynamics within individual adhesion complexes in living cells under physiological conditions were recorded for as long as 25 min with a spatial resolution of 60 nm and a frame time of 25 s (Shroff et al., 2008). A major drawback of stochastical read-out approaches is the poor temporal resolution. The faster the photons are emitted, the shorter the data acquisition. The cameras should therefore run at a fast frame rate (500 Hz) and the excitation intensity should be chosen to match the desired number of collected photons within the timespan of a camera frame. The camera can be conveniently operated asynchronous to the $\mathbf{B}\rightarrow\mathbf{A}\rightarrow\mathbf{B'}$ cycles, as stated in the variant PALM with independently running acquisition (PALMIRA) (Egner et al., 2007).

A generalization can be made regarding suitable dyes for the stochastical read-out. As a sufficient condition, the dyes have to feature a stable or metastable optically or chemically manipulable dark state. This has the potential to make the vulnerable switchable or photoactivatable fluorophores or fluorophore assemblies such as double-labelled antibodies with a reporter and an activator dye (needed for STORM) redundant. A simplified version of STORM is direct STORM (dSTORM), which uses commercially available antibody (FAB fragment)-cyanine dye conjugates for subdiffraction imaging instead of a special dye for activation (Heilemann et al., 2008). In ground state depletion followed by individual molecule return (GSDIM) the molecules are switched off by depleting the molecular ground state and shelving the dye molecules into their triplet state. The read-out is stochastical with an independent running acquisition like PALMIRA. The dye molecules are not optically activated but are automatically switched on after their spontaneous return from the dark state to their singlet state (Fölling et al., 2008). The dark state (**B**) can also be the absence of a label if freely diffusing probes are used which are binding reversibly to the target structure. In points accumulation for imaging in nanoscale topography (PAINT), the probes are hitting the object of interest, get immobilized (entering state **A**) and are read out. After a certain time, the probes are leaving the structure (**B**) or are photobleached (**B´**) (Sharonov and Hochstrasser, 2006). The freely diffusing probes induce an overall background which is however well below the defined signals generated by the immobilized probes.

2.3 Photobleaching

The performance of a fluorophore strictly determines the ability of a fluorescence microscope to detect specific molecules at very low concentrations. Fluorescent dyes featuring high excitation coefficients, high quantum yields, and large Stokes shifts are now widely available. However, the photostability of the dye used is another crucial attribute. In laser scanning microscopy (LSM), the laser beam has to be intense enough to provide an adequate signal-to-noise ratio within a reasonable scan time. Under these conditions, the fluorescence emitted is often decreasing in intensity with exposure time, a phenomenon referred to as photobleaching. In general, photobleaching reduces the signal-to-noise ratio and the precision of most techniques relying on fluorescence (Pawley, 2006). Endeavors to understand the mechanisms underlying photobleaching and to tackle them will become more and more important especially in the nanoscopic field. Unfortunately, the mechanism of photobleaching is by far not fully understood, even in the case of very common dyes like fluorescein in solution (Song et al., 1996).

Photobleaching renders a molecule irreversibly non-fluorescent. This can be caused by a photochemical modification, either photolysis, i.e. light induced cleavage of chemical bonds, or other modifications like the addition of radicals to double bonds the chromophore is based on. A generalization of the exact photobleaching mechanisms fails, since many parameters like the dye used, the molecular environment and the intensity of excitation light may affect the mechanism and the rates of photobleaching (Bernas et al., 2004).

2.3.1 Photobleaching mechanisms

Several theories have been proposed to explain the photobleaching processes. The interaction of molecular oxygen in its triplet ground state with excited fluorophores is a probable step of the mechanism leading to photobleaching. If a dye molecule exhibits a high intersystem crossing rate (k_{ISC}), a significant number of molecules cross from the excited singlet state ($S1$) to the long lived excited triplet state ($T1$) (Fig. 2.1). Rhodamine derivatives usually exhibit intersystem crossing rates k_{ISC} in the range of 5 to $6.5*10^5 s^{-1}$ (Menzel and Thiel, 1998). With a nanosecond fluorescence lifetime, the measured rate constant k_{ISC} corresponds to a quantum yield for the triplet population in the range of 10^{-3}.

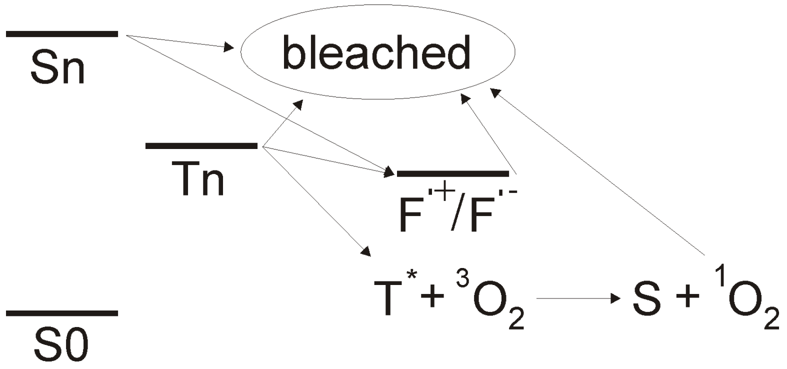

Fig. 2.6: A multitude of different bleaching precursors and bleaching pathways are conceivable. All higher excited states (*Sn*, *Tn*) can be precursors for photoionization reactions yielding reactive radicals ($F^{\circ+}/F^{\circ-}$). The crucial state is the triplet state *T1*, which is the origin of many chemical processes leading to photobleaching (“*bleached”*). Because of the long lifetime and the higher energy containment of the triplet state, further interactions yielding radical ions ($F^{\circ+}/F^{\circ-}$) (photoionization) are probable. Alternatively, photooxidation, in which highly reactive singlet oxygen ($^1O_2$) is formed by sensitization of ground state triplet oxygen ($^3O_2$) by triplet state dyes (T^*), can take place.

Dye molecules in the excited triplet state feature a 1000 to 100000 times longer time frame for reactions compared to the fast-relaxing molecules in the excited singlet state and additionally provide the necessary energy. Interactions of a dye in *T1* with triplet oxygen $^3O_2$ generates singlet oxygen $^1O_2$. At the same time, the dye returns to the singlet ground state (Fig. 2.6). Singlet oxygen has a similar lifetime in water as dye molecules in *T1* (20µs) and is responsible for damaging effects due to the production of many different highly reactive radical oxygen species (photooxidation) (Merkel and Kearns, 1972). A fluorophore in *T1* is also highly reactive and can undergo irreversible chemical reactions with surrounding molecules, leading to a direct destruction of the chromophore system. Pathways via photoinduced ionizations involving radical cations and anions ($F^{\circ+}/F^{\circ-}$) are also proposed (Widengren et al., 2007; Vogelsang et al., 2008). All these reaction pathways depend on the concentration of molecular oxygen, the dye properties, and the availability of other suitable reaction partners such as lipids, proteins, oxidative and reductive agents. The pathways can therefore be different for binding to different compartments of the cell (Benson et al., 1985). If a dye is protected from reacting with environmental molecular oxygen, the observed rate of photobleaching is lower (Bernas et al., 2004). This occurs naturally in GFP, where the intrinsic chromophore is positioned in the core of a β-barrel structure (Ormö et al., 1996).

Reactive oxygen species (ROS) in living cells generated by the reaction of triplet oxygen with dyes (also intrinsically fluorescent proteins such as the phycobiliproteins) in the triplet state via singlet oxygen (Fig. 2.6) are responsible for cell damaging or phototoxicity (Pawley, 2006).

Two-step photolysis

Alternatively, the absorption of an additional photon by an already excited molecule depositing even more energy in the dye system may also be involved in bleaching processes of some dyes. Molecules in the first excited singlet and triplet states, *S1* and *T1*, may be subject to so-called two-step excitation, where the molecules are excited to higher electronic states, *Sn* and *Tn*, by absorption of a second photon (Eggeling et al., 1998). In polar solvents like water, these states couple efficiently with ionic states due to the high solvation energy. Once excited to the state *Xn* (either *Sn* or *Tn*), a molecule can either directly relax to *X1* with a quantum yield of ($1-\phi_{ion}$), or form a radical cation electron pair $(M^{\cdot +}e^{-})$ with a quantum yield of ϕ_{ion} (photoionization) (Fig. 2.7b).

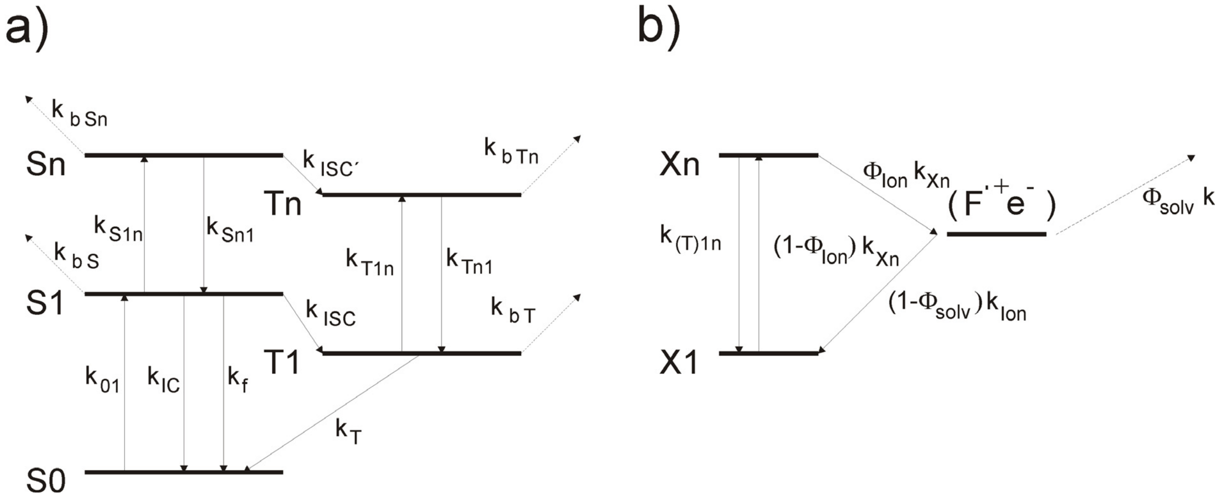

Fig. 2.7: Electronic energy diagram of a fluorophore with five electronic states depicting photobleaching (k_{bSn}, k_{bTn}, k_{bS}, k_{bT}) from each higher excited electronic state (*S1, Sn, T1, Tn*)(**a**). Basic mechanism of the photobleaching reaction from a higher excited state *Xn* (*X=S or T*) including the formation of an ion pair $(F^{\circ +}e^{-})$(**b**). Modified from Eggeling et al., 1998.

This radical ion pair can undergo two depopulation reactions described by the rate constant k_{ion}: either fast geminal charge recombination to the first excited state, *S1* or *T1*, respectively; or an escape reaction, characterized by the quantum yield of solvation, ϕ_{solv}, to form a free radical cation and a solvated electron. Because organic radical cations are chemically unstable in polar solvents, two-step and multi-step absorption processes open up additional channels for photobleaching (Anbar and Hart, 1964; Reuther et al., 1996; Khoroshilova and Nikogosyan, 1990). The quantum yields, ϕ_{ion} and ϕ_{solv}, increase with increasing electronic excitation, n. This two-step photolysis is readily obtained by the use of pulsed lasers, as shown previously in the case of coumarins and Rhodamine 6G (Eggeling et al., 1997, Aristov, 1994). Photobleaching following pulsed excitation depends on the peak irradiance as well as on the repetition rate.

The photobleaching of a dye solution can be characterized by the quantum yield of photobleaching, ϕ_b, or the photobleaching probability, p_b. Usually, photophysical and photochemical reactions are characterized by a quantum yield. The quantum yield of a photobleaching reaction is equal to the number of molecules that have been photobleached, divided by the total number of photons absorbed during the same time interval

$$\phi_b = \textit{(number of photobleached molecules)/(total number of absorbed photons).} \qquad (2.9)$$

It is important to note that the total number of absorbed photons also includes those absorbed in a second step, leading to higher excited electronic states, which opens up new bleaching channels. However, since fluorescence emission is usually related to the first excited singlet state, *S1*, it is crucial for the accuracy of experiments such as single-molecule fluorescence detection to know the probability of photobleaching, p_b, at a certain excitation irradiance. The probability is equal to the number of photobleached molecules divided by the mean number of molecules in the *S1* state for a given time interval

$$p_b = \textit{(number of photobleached molecules)/(number of molecules in S1).} \qquad (2.10)$$

Unfortunately, the total number of absorbed photons as well as the mean number of molecules in the *S1* state cannot be measured precisely, which makes it impossible to determine ϕ_b and p_b directly. However, it is possible to measure the number of irreversibly photobleached molecules as a decrease in the dye concentration, $c(t)$, with time, t. The photobleaching reaction can be regarded as a quasi-unimolecular reaction. This assumption results in an exponential decrease of the dye concentration (Hirschfeld, 1976; Eggeling et al., 1997)

$$c(t) = c_0 \, exp(-k_Z t) \, . \tag{2.11}$$

c_0 is the initial concentration at time $t = 0$ and k_z is the effective pseudo-first-order bleaching rate constant. Fig. 2.7a shows the electronic energy diagram of a dye molecule with five electronic levels: ground singlet state, *S0*, first excited singlet state, *S1*, lowest excited triplet state, *T1*, and higher excited singlet and triplet states, *Sn* and *Tn*. Photobleaching reactions are assumed to be possible from all excited states with the microscopic rate constants k_bS, k_bT, k_bSn, and k_bTn, respectively.

As long as the fluorescence flux depends linearly on the excitation irradiance (**low excitation irradiance range**), which is the case in cell-bleaching experiments, the probability of a molecule to be in a first excited electronic state, *S1* or *T1*, is very low. Hence, the absorption of a second photon by *S1* and *T1* can be neglected, and the electronic five-level system described above simplifies to a **three-level system** with the states *S0*, *S1*, and *T1*. Then bleaching occurs only from *S1* and *T1*, where $\phi_b(I)$ is independent from *I* and equivalent to $p_b(I)$ (the subscript *eq* denotes the steady-state population probability)

$$\phi_b(I) = \frac{k_Z}{k_{01} S_{0eq}} = \frac{k_b}{k_0} = \frac{k_Z}{k_0 S_{1eq}} = p_b(I) = const. \tag{2.12}$$

At excitation irradiances necessary for effective single molecule application (**high excitation irradiance range**) and in STED microscopy, the population of *Sn* and *Tn* due to n-step ($n \geq 2$) excitation becomes important. Therefore, a **five-level system** (Fig. 2.7a) has to be considered including the higher excited singlet and triplet states *Sn* and *Tn*. *Sn* and *Tn* open up new channels for photobleaching. The effective bleaching rate constant k_z is then a sum of the composite microscopic bleaching rate constants k_b of the first excited electronic states *S1* and *T1* and $k_{bn}I$ of the higher excited electronic states *Sn* and *Tn* with $k_{bn} = (k_{bSn} / k_{Sn1}) \sigma_{1n} \gamma + (k_{ISC} / k_T)(k_{bTn} / k_{Tn1}) \sigma_{T1n} \gamma$. The probability of photobleaching $p_b(I)$ for a five-level system is then dependent on the irradiance intensity and given by

$$p_b(I) = \frac{k_Z}{k_0 S_{1eq}} = \frac{k_{bn} I + k_b}{k_0} = \frac{k_{bn}}{k_0} I + p_b^3 = \frac{k_{bn}}{k_0} I + \phi_b^3 . \tag{2.13}$$

p_b^3 and ϕ_b^3 can be determined for the three level system. The theoretical model is confirmed by experimental data using coumarin and rhodamine derivatives in air saturated aqueous solutions. For a detailed theoretical description see (Eggeling et al., 1998).

Deschenes and vanden Bout propose a **four-level system** to describe the photobleaching rate of Rhodamine 6G in poly(methylacrylate) PMA under vacuum (Deschenes and vanden Bout, 2002) (Fig. 2.8).

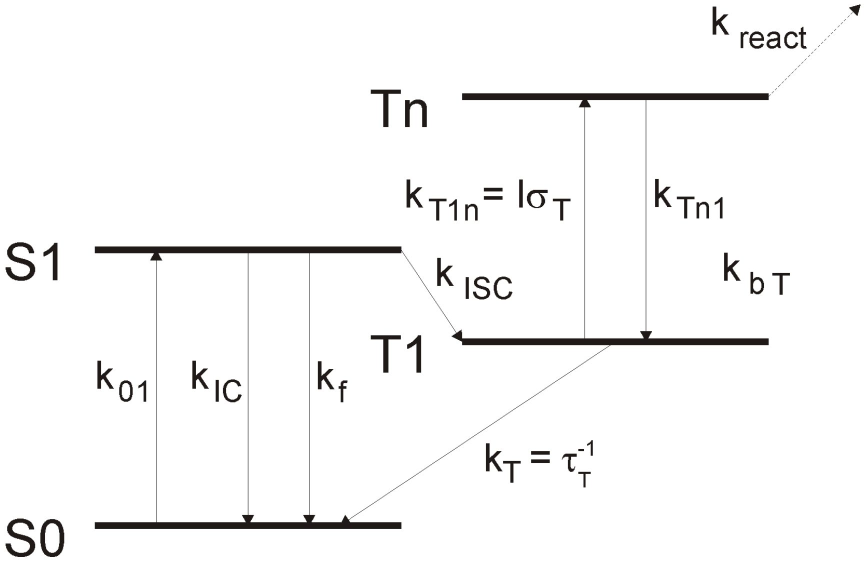

Fig. 2.8: Jablonski diagram of the relevant states for photobleaching of Rhodamine 6G. Absorption (k_{01}) from *S0* to *S1* may lead to radiationless internal conversion (k_{IC}), fluorescence (k_f), or intersystem crossing (k_{ISC}) to *T1*. From *T1*, the molecule may relax to *S0* (k_T), or absorb a second 532 nm photon (k_{T1n}) and go to *Tn*. From there, the molecule may either relax back to *T1* (k_{Tn1}) or react (k_{react}), leading to irreversible photobleaching. Modified from Deschennes and van den Bout, 2002.

Photobleaching is modeled as a two-photon process where the first photon excites the molecule to *S1*, from which it undergoes intersystem crossing to *T1* where the second absorption takes place, producing a *T1*→*Tn* transition where *Tn* is the reactive state for the photobleaching reaction. The short-lived higher excited singlet states are not considered (Fig. 2.8). The study reveals that low excitation rates yield long photochemical survival times and unprecedented amounts of emitted photons. A higher triplet excited state *Tn* is found to be the predominant reactive state for photobleaching. Based on the model of the fluorophore as a three-level system, the kinetics governing the steady state populations of the ground singlet state *S0*, singlet excited state *S1*, triplet excited state *T1*, can be written as

$$\begin{aligned}
\frac{dS0}{dt} &= -k_{01}S0 + k_S S1 + k_T T1 = 0 \\
\frac{dS1}{dt} &= k_{01}S0 - k_S S1 + k_{ISC} S1 = 0 \\
\frac{dT1}{dt} &= k_{ISC} S1 - k_T T1 = 0.
\end{aligned} \tag{2.14}$$

S0, *S1*, and *T1* denote fractional populations in each state, where all three must sum up to unity. The rate k_s is used to denote all depopulation routes from *S1* to *S0* (intersystem crossing *IC* and fluorescence f). From Eq. (2.14), the intensity-dependent population in the triplet state is given by

$$T1(I) = \frac{k_{ISC}\sigma I}{\sigma I(\tau_T^{-1} + k_{ISC}) + \tau_T^{-1}\tau_S^{-1}} \, . \tag{2.15}$$

It can be seen that the triplet population is a function of excitation intensity (I), absorption cross section (σ), singlet excited state lifetime(τ_s), intersystem crossing rate (k_{ISC}), and triplet state lifetime (τ_T). The bleaching rate, shown in Fig. 2.9, is strongly intensity-dependent.

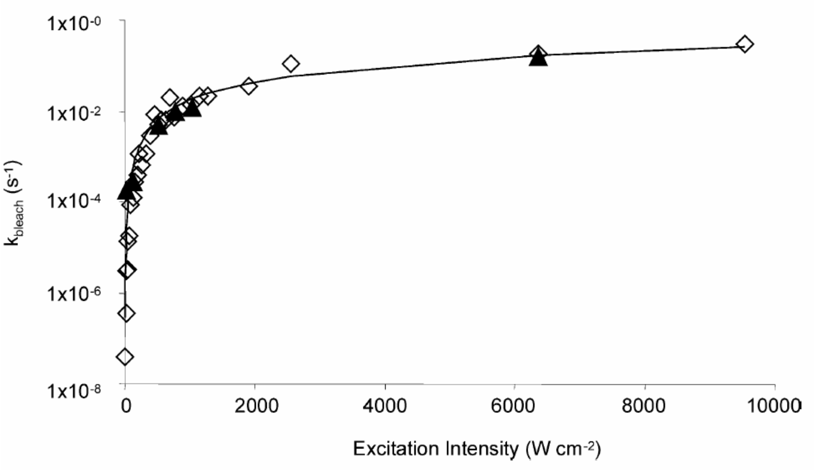

Fig. 2.9: The overall rate of photobleaching k_{bleach} for a single molecule. Single molecule points (▲) are given by the inverse of the average survival time, while ensemble points (◊) are calculated from the total photons detected per molecule scaled by the intensity-dependent emission rate. The fitted line yields the calculated photobleaching rate, k_{bleach} (Eq. (2.16)). Modified from Deschennes and van den Bout, 2002.

This strong intensity dependence implicates that the absorption of a second photon from the triplet state is responsible for creating the active state from which photobleaching occurs. The bleaching rate can be written as

$$k_{bleach} = T1(I)I\sigma_T\Phi_{react}\,. \tag{2.16}$$

with $T1(I)$ as the population of the excited state (Eq. 2.15), I as the excitation intensity, σ_T as the cross-section for triplet–triplet absorption, and Φ_{react} as the probability of a reaction once the molecule is in Tn: $\Phi_{react}=k_{react}/(k_{react}+k_{Tn1})$. Even at the lowest excitation intensities, the results show an intensity dependence stronger than triplet saturation, thus suggesting that two-photon photobleaching is the dominant mechanism even at low irradiation intensities. This is in contrast to the result from Eggeling et al. above discussed, but might be explained by different chemical environments. Furthermore, the presence of dissolved oxygen in the aqueous solvent can drastically change the intersystem crossing and triplet relaxation rates, altering the energy landscape and relevant lifetimes of the excited states.

Because of the very short lifetime of *S1*, it is unlikely that photobleaching occurs from a higher excited singlet state *Sn*. Since the cross-section for triplet–triplet absorption is fairly large, it is reasonable to assume that photobleaching occurs from *Tn*. The conventional view that although high excitation rates lead to shorter survival times, the photon yield is fixed, must be dismissed.

2.3.2 Reducing photobleaching

The mean number of excitation cycles survived by a molecule spans across a wide range from for example 1000 (coumarin derivatives) to 3000000 (Tetramethylrhodamine). The number of photons emitted before a dye molecule is destroyed depends on the nature of the dye molecule itself, on its environment, and on the irradiance and can be strongly influenced (Eggeling et al., 1998). First of all, the detection efficiency must be optimized to decrease the required excitation intensity if photobleaching is to be avoided. Using fluorescence correlation spectroscopy (FCS), several chemicals were found to be effective anti-bleaching agents (Dittrich and Schwille, 2001). All the relevant steps involved in photobleaching processes can be attacked by additives. Triplet quenchers such as 2-mercaptoethylamin

(MEA) can reduce the triplet lifetimes of the dye, singlet oxygen scavengers like 1,4-diazabicyclo[2,2,2]octane (DABCO) lower the concentration of the highly damaging oxygen form. Radical scavengers and anti-oxidants quench the occurrence of secondary radicals, reducing or oxidizing agents recover radical ions (Song et al., 1996; Schwille et al., 2001, Pawley, 2006, Widengren et al., 2007). One has to keep in mind, that fluorescence quenching is often accompanied by reduced photobleaching. The concentration of anti-fading agents should be kept sufficiently low in order to avoid a collision rate with fluorophores in the singlet system that would lead to either fluorescence quenching or bleaching due to modification, i.e. reduction or oxidization (Widengren et al., 2007). As molecular oxygen is one of the main players in photobleaching, deoxygenating by degassing or the application of an oxygen-scavenging system based on catalase and glucose oxidase and subsequent substitution of the oxygen’s triplet relaxation capability by an alternative triplet quencher can strongly prolong the survival times (Harada et al., 1990; Heilemann et al., 2005). However, most stabilizers are not compatible with live cell experiments (one exception is *N*-propyl gallate).

A new approach for minimizing photobleaching and blinking by recovering reactive intermediates was recently introduced by Vogelsang et al., 2008. The method is based on the removal of oxygen owing to its dye-dependent influence on photostability and oxidizing properties and quenching of triplet as well as charge-separated states by electron transfer reactions. To accomplish this, a structure that contains reducing as well as oxidizing agents, namely a reducing and oxidizing system (ROXS), is used. The success of this approach is demonstrated by single-molecule fluorescence spectroscopy of oligonucleotides labelled with different fluorophores: cyanines, (carbo-)rhodamines, and oxazines, in aqueous solvents; individual fluorophores can be observed for minutes under moderate excitation with increased fluorescence brightness.

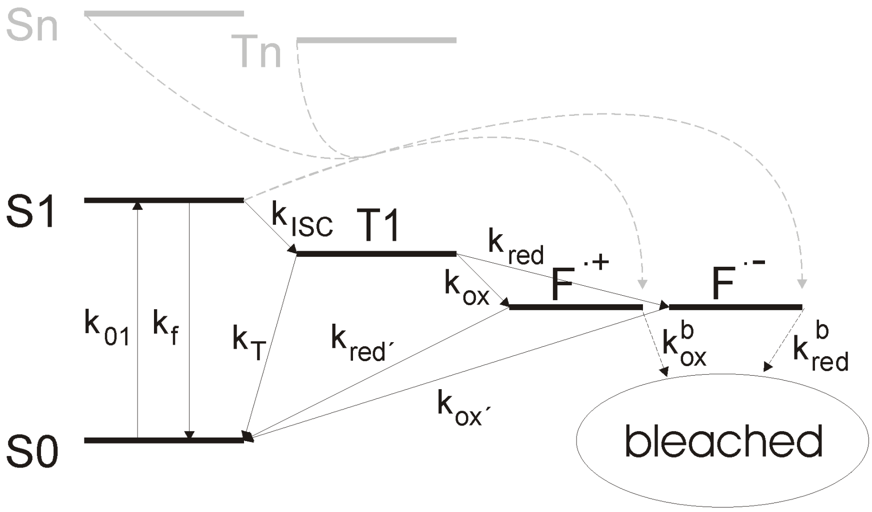

Fig. 2.10: Photoinduced processes of an organic fluorophore that lead to photobleaching ("*bleached*"). The steps k_{01}, k_f, k_T, k_{ISC} are described in Figs. 2.1, 2.6, 2.7, 2.9. With ROXS, the *T1* is rapidly relaxed via electron transfer reactions. The oxidizing agent can either lead to the formation of a radical cation $F^{\circ+}$ with the rate constant k_{ox}, or the reducing agent forms a radical anion $F^{\circ-}$ (k_{red}). The two possible radical ions are then recovered to the singlet ground state by another set of electron transfer reactions ($k_{red'}$ and $k_{ox'}$). The rapid recovery by ROXS prevents further photobleaching steps (k_{ox}^{b}, k_{red}^{b}). Higher excited states are also involved in photobleaching, as discussed above, but not addressed here. Modified from Vogelsang et al., 2008.

As an alternative triplet-quenching mechanism, electron transfer reactions are suggested. Triplet quenching by electron transfer, however, yields a radical anionic or cationic dye molecule (with respect to an assumed neutral ground state). Such ionized dyes can also be formed by other pathways such as photoionization, and they represent additional potentially reactive intermediates in photobleaching pathways (Widengren et al., 2007; Hoogenboom et al., 2005). Depending on the predominant photobleaching pathway, that is, whether for a certain fluorophore the triplet, the reduced, or the oxidized form is the more reactive intermediate towards photobleaching, redox-active agents might reduce or even increase the photobleaching rate. The ROXS provides a universal method to improve the photostability and reduce blinking of fluorescent dyes using both a reducing and an oxidizing agent to quickly recover all triplet states and ionized states. The working principle of the developed reducing and oxidizing system (ROXS) is shown schematically in Fig. 2.10. After intersystem crossing to *T1*, the fluorophore can be reduced by the reducing agent (ascorbic acid, trolox, or cysteamine (1 mM) for example) yielding the radical anion $F^{\circ-}$. The radical anion is then quickly reoxidized by the oxidizing agent (one electron acceptor methylviologen (1 mM) for example) to repopulate the singlet ground state. Alternatively, the fluorophore is oxidized from *T1* by the oxidant to form $F^{\circ+}$ and subsequently returns to the ground state by the reductant. The fast recovery of the singlet ground state is essential to successfully compete with side reactions leading to photobleached products ("*bleached*"). Other conceivable pathways can also yield radical ions as indicated in gray in Fig. 2.10, but they are not explicitly discussed in this context. The oxidizing and reducing agents are chosen out of thermodynamic considerations and not empirically.

2.3.3 Photobleaching in subdiffraction fluorescence microscopy

Especially nanoscopic microscopy techniques call for high photostability, because higher spatial resolution requires a more precise scanning of the object i.e. a higher number of pixels, since the probe is smaller in size. A higher number of pixels is connected to a higher light dose affecting the sample if the dwell time is kept constant (depending on the sample, the dwell time does not necessarily have to be constant; if the signals are well separated, the dwell time can be decreased). Therefore pronounced photobleaching, higher dark state transition rates and more severe phototoxicity occur. Furthermore, the more photons a dye emits, the better it can be located if stochastical read-out methods are applied. The time a molecule spends in its dark states is a crucial parameter, because data acquisition times should be kept short for dynamical assays. In targeted read-out schemes a photostable dye allows for increasing the intensity of the signal suppression beam, thus confining the volume allowed to fluoresce. Intense photobleaching always hinders high resolution imaging because it either limits the maximal count rate or the maximal signal suppression intensities in zero based high resolution techniques.

In zero-based high resolution methods the dye molecules that are not present in the zero at a certain time are forced into the non-fluorescent state. If the non-fluorescent state has to be maintained during read-out, the dye molecules undergo a high and finite number of excitation and/or signal suppression cycles which is the major drawback of using metastable non-fluorescent states. After each cycle, the dye molecule makes a transition into a dark or triplet state with a finite probability. The higher the cycle count, the higher the probability to end up in the states which are well-known precursors for bleaching pathways. If the cycle number is too high, the acquisition of high resolution images is hampered. Therefore the reduction of the number of switching cycles addresses a fundamental problem in zero-based high resolution microscopy using metastable off-states.

In STED microscopy, photobleaching is significantly increased because dye molecules in the triplet state, populated by the high cycle count, can be further excited by the intense red-shifted STED laser beam leading to higher excited triplet states (*Tn*) and two-step photolysis even at low excitation intensities. Rhodamine 6G for example exhibits a broad triplet-triplet absorption in the visible and a high triplet absorption cross-section which is roughly an order of magnitude smaller than the *S0→S1* cross-section (Deschenes and vanden Bout, 2002; Korobov and Chibisov, 1978; Pavlopoulos et al., 1988). This renders *T→T* absorption by a STED beam, which is a 10000 times more intense than the excitation beam, highly probable. Higher excited singlet states might also be involved in STED-conditioned bleaching pathways. In cw-STED mode, a dye can theoretically perform a higher number of *S0-S1* cycles because the dye gets de-excited after vibrational relaxation (ps) and is immediately re-excited by the persistent excitation light. Each cycle gives rise to a certain probability that the molecule transits to the triplet state. High cycle numbers mean high population of the triplet state. In either case, the *T1* state is the fundamental precursor for bleaching pathways. Motivated by the role of triplet states in bleaching pathways and signal intensification, a new imaging modality was addressed, namely dark state or triplet state relaxation (D-REX or T-REX) (Donnert et al., 2006). By ensuring that the transient molecular dark states, such as the triplet state, relax between two molecular absorption events, the bleaching is reduced and the signal intensity increased. Since triplet lifetimes are quite long (microseconds), the pulsed laser source in case of the D-REX mode had a repetition rate of about 1 MHz leading to long data acquisition times rendering it not suitable for live cell acquisition. Moreover, T-REX does not reduce bleaching effects associated with higher states within the singlet system of the dye itself.

Chapter 3

Adaptive filtering and simple STED

The ability to employ a variety of new dyes with enhanced properties regarding quantum yield, photostability, lifetime, depletion efficiency etc. and new lasers in a fluorescence microscope is of particular importance. More photostable or less toxic organic dyes or fluorescent proteins may allow experiments which are not possible otherwise. Sometimes, a certain chemical environment or embedding is needed which in turn can strongly influence spectral properties (Fig. 6.8). Flexibility calls for tunable elements to match the wavelength of light replacing elements with fixed properties in a microscope. Fig. 3.1 sketches the most important elements of a STED microscope.

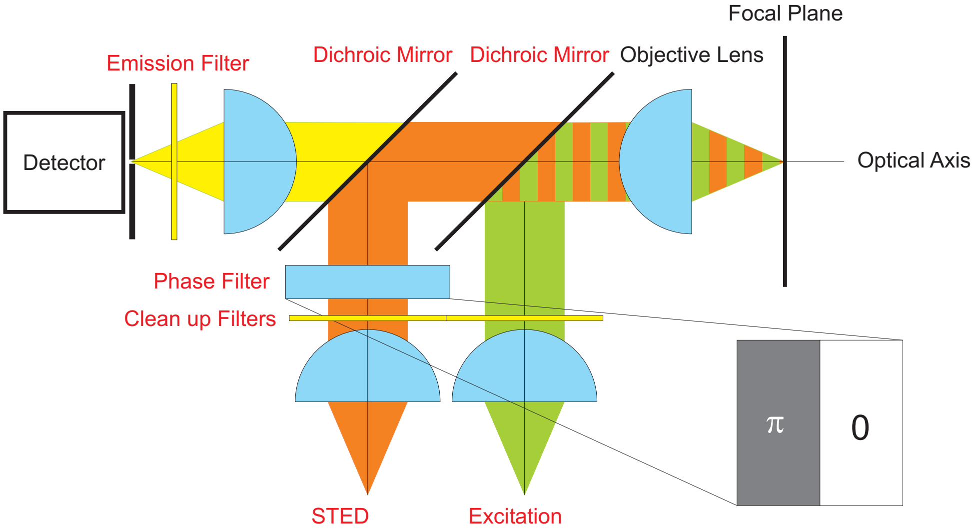

Fig. 3.1: Sketch of a STED setup already introduced in Fig. 2.5. The parts that should be tunable to offer flexibility regarding alternative dyes and lasers are written in red. The phase plate depicted here provides a zero line in one dimension after focusing.

Some parts such as achromatic lenses are wavelength independent over a wide range of the spectrum. However, a lot of parts have to be adapted to accommodate changed excitation or signal suppression sources, fluorescent dyes or whole setup rearrangements.

These parts are:

excitation and signal suppression beam filters (clean up filters)
phase filter to generate a signal suppression beam featuring a zero intensity
dichroic mirrors for separation of the fluorescence
spatial filter (pinhole)
detection filter

In a typical microscope, thin film interference filters, dichroic mirrors and phase filters with fixed wavelength characteristics are used and have to be changed if new lasers, new dyes or new setup arrangements are implemented. Exchanging filtersets is accompanied by a time consuming system realignment. Wavelength tunable elements are therefore highly desirable.

On the following pages, tunable elements to replace clean up filters, phase filters, dichroic mirrors and detection filters with fixed characteristics are described. A quadruple acousto-optic tunable filter (AOTF) arrangement serves as a freely programmable dichroic mirror and clean up filter. The combination with a prism-based spectrometer yields an adaptive detection filter, which can be used as a notch or band pass filter having the potential to make thin film interference filters redundant. STED measurements with polystyrene beads and SupT1 cells prove that the adaptive filter system shows comparable performance to thin film interference filters, with the additional advantage of flexibility.

The tunable phase filter consists of two adjacent optical flats which are slightly tilted with respect to each other and imprint a phase shift of π on one half of the beam. Any wavelength can be matched to feature a phase shift of π just by rotating the two optical flats. Hence, another simplification results from the new phase filter in combination with STED in cw mode. The excitation as well as the signal suppression beam can be provided by one laser without the need for separation by a dichroic mirror. Both beams pass the new phase filter and are inherently aligned. Dependent on the wavelength, a phase shift is generated for the signal suppression beam, whereas the excitation beam stays unaltered due to dispersion. The principle was shown with polystyrene beads at a resolution of 40 nm.

3.1 Optical setup

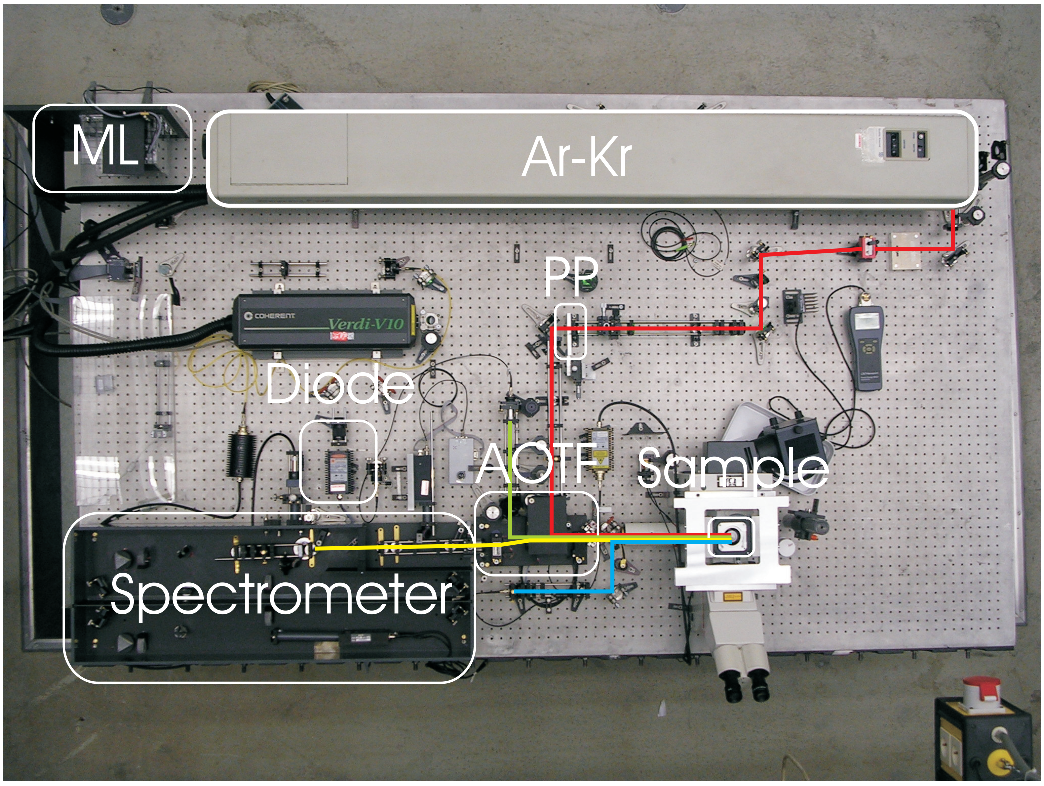

Fig. 3.2: The optical setup used for the majority of experiments. The confocal setup consists of an actively mode-locked (ML, modelocker) Ar-Kr-laser for pulsed and cw mode applications (red beam path) and of a variety of high repetition rate (amplified and frequency converted) diode lasers for excitation (green and blue beam paths). The phase of the signal suppression beam is manipulated by a phase plate (PP) in such a way that an intensity zero is generated after focusing. The lasers are coupled into a stage-scanning microscope via a quadruple AOTF arrangement serving as a freely programmable dichroic mirror. Fluorescence light (yellow beam path) passes the AOTFs unaltered, is confocalized by a pinhole, enters the spectrometer and is detected with an APD (Fig. 3.3).

The optical setup was built from scratch and used for the majority of the experiments described in this thesis is depicted in Fig. 3.2. The system is based on a confocal microscope equipped with an Ar-Kr-laser (Spectra Physics-Division of Newport Corporation, Irvine, CA) which provides a variety of laser lines with high intensities mandatory for STED microscopy (Tab. 3.1) and, therefore, offers high flexibility regarding measurements of different dyes (647 nm pulsed and cw for Atto565, NK51, Dy485XL, Nile red; 676 nm cw for Mn-QD, 514 nm pulsed and cw for coumarin derivatives, DAPI, and SYTOX blue).

Wavelength/nm	**Power/W (cw)**
350.7	0.8
356.4	0.4
406.7	0.72
413.1	1.4
415.4	0.24
468.0	0.4
476.2	0.3
482.5	0.3
488.0	2
514.5	**2.5**
530.9	1.2
568.2	0.5
631.2	0.16
647.1	**2.5**
676.4	**0.72**
752.5	0.95

Tab. 3.1: A compilation of all laser lines with the corresponding powers provided by the Ar-Kr-laser. The mainly used laser lines are written in bold letters.

Each laser line can be used in cw mode or can be actively mode-locked (APE, Berlin, Germany) for pulsed excitation and/or pulsed STED experiments. The mode-locked laser lines typically have 20 to 30% of the average power provided in cw mode. Besides the Ar-Kr-laser lines the setup also contains pulsed high-repetition rate laser diodes (PicoQuant, Berlin, Germany) and cw laser diodes for excitation of the fluorescent dyes (405 nm (coumarins Atto390, C6H, C522), 440 nm (Mn-QD, Atto425), 470 nm (Dy485XL)). For excitation at 532 nm (Nile red beads, NK51, Atto565) a pulsed amplified diode laser is applicable (PicoTA, PicoQuant, Berlin, Germany). In the case of pulsed STED experiments the laser diodes are synchronized with the STED-laser via a photodiode (Alphalas, Göttingen, Germany) and a home built programmable delay unit (MPI Göttingen, Germany).

The excitation and signal suppression beams are combined using acousto-optic tunable filters (Crystal Technology, Palo Alto, CA) and coupled into a microscope stand (DMI 4000B, Leica Microsystems GmbH, Mannheim, Germany) equipped with a three axis piezo stage-scanner (PI, Karlsruhe, Germany) and an ACS APO, 63x/1.30NA oil immersion lens (Leica Microsystems GmbH, Mannheim, Germany). The acousto-optic tunable filters (AOTF) allow the power of each laser beam to be controlled independently and also separate counterpropagating fluorescence returning from the confocal microscope. The power and the radio frequency of the AOTF are controlled with a home built software (LabVIEW, National Instruments, Austin, USA), either in digital (RS232) or in analog mode for high speed blanking purposes (see RESCue experiments) (NI-DAQ, National Instruments, Austin, USA). They are also part of a new adaptive filter system which will be described later in this chapter. The 405 nm diode is reflected into the microscope via a dichroic mirror because of the limited radio frequency range of the AOTFs employed. Collected fluorescence passes through an additional band-pass filter (AHF Analysentechnik, Tübingen, Germany) or the prism based spectrometer (Fig. 3.3a, c) described below and is detected using a photon-counting module (SPCM-AQR-13-FC, PerkinElmer, Canada). The generated signal is recorded with a multichannel analyzer (MCA)(FAST ComTec Communication Technology GmbH, Oberhaching, Germany) which is controlled by the data acquisition software Imspector (MPI Göttingen, Germany).

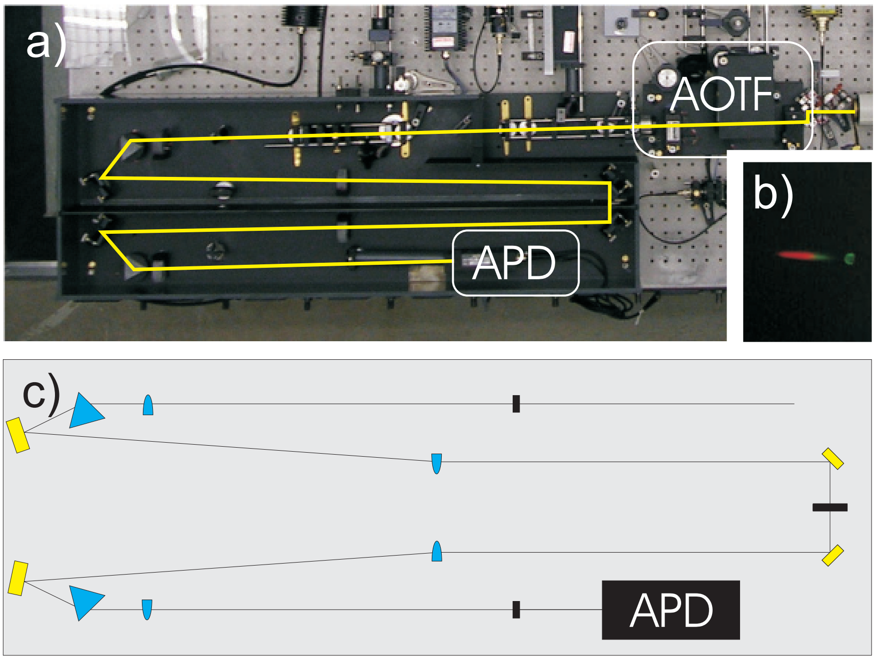

Fig. 3.3: (**a**) and (**c**) depicts the spectrometer in detailed view. Having passed the confocal pinhole (black rectangle), the beam is parallelized by a lens (blue semi-oval; a lens with a focal length of 500 mm was quartered to ensure the same optical properties for all lenses within the spectrometer) and is spectrally dispersed by a prism (blue triangle, SF10). A mirror reflects the fluorescence spectrum towards a second lens (*f* = 500) that focuses the fluorescence spectrum to a sharp line shown in (**b**). After yet another mirror, the sharp line spectrum can be manipulated with plates and a strip. After that, the filtered beam passes a second set of components recombining the manipulated spectrum to a single beam and which is launched into a multi-mode fibre for detection using an APD.

For RESOLFT experiments, one has to introduce a phase-plate in a plane that is conjugated to the entrance pupil of the objective lens. RESOLFT nanoscopy requires the modulating beam to have a zero or null which is used to confine the region in which fluorescence is allowed. A simple way of producing such a phase distribution is to introduce a 180º phase-step midway through the modulation beam before it is focused. To accomplish this, two identical adjacent optical flats are placed in the modulation beam, and one is tilted slightly to adjust the path length in one half of the beam. When focused, the resulting point-spread function (PSF) exhibits a line of zero intensity through its center and can be used to selectively inhibit fluorescence of dyes. With the aid of this phase plate based on two adjacent optical flats, the desired phase shift can be generated for any λ. Additionally, it allows to simultaneously manipulate the excitation and signal suppression PSFs of cw laser lines provided by one single laser or fiber source. Time-consuming PSF alignment procedures are redundant as described in section 3.2.2. Alternatively, a vortex phase plate (RPC Photonics, NY, USA) was used in the modulation beam path to generate a doughnut-shaped point spread function in the focus. The diffraction-limited PSFs of the excitation and modulation beams are characterized by scanning nanometric gold particles (80 nm suspended in Canada-Balsam) through the focused beam while detecting the back-scattered laser light. Special requirements and changes of the setup are described in the corresponding chapters.

The major advantage of the setup introduced here is its superior flexibility. The Ar-Kr-laser provides a variety of different laser lines. With the aid of the AOTFs as a freely programmable dichroic mirror, every laser line in the visible range from 420 to 700 nm can be cleaned up and coupled into the microscope without any alignment. In combination with a prism-based spectrometer, the result is an adaptive filter system (described in the following). A tunable phase filter further supports the flexibility and allows for easy adaptation to different dyes and experiments.

3.2 STED microscopy applying an adaptive spectral and phase filter system

3.2.1. An adaptive spectral filter system consisting of a quadruple AOTF arrangement and a prism based spectrometer

Quadruple AOTF arrangement serving as a tunable dichroic mirror

A standard confocal microscope contains many thin film interference filters. Clean-up filters may be required to get rid of the spectrally broad sockets of laser sources overlapping with the desired emission of the fluorescence dyes, especially if laser diodes are used. To separate the excitation light from the fluorescence signal, dichroic mirrors are employed. Before the detection, a bandpass filter selects the desired fluorescence photons. A STED setup requires even more filters with stringent specificities because the intense STED wavelength is necessarily located within the fluorescence spectrum. All standard filters have fixed spectral properties. When new lasers are coupled into a microscope, new dyes are used, or the whole system is rearranged, these filters have to be changed. One has to have different sets of filter combinations ready at hand to be flexible enough to adapt to differently labelled samples or changed setup conditions. The exchange of filters is often accompanied by the need for time-consuming system realignment because of unavoidable beam displacement. Especially the field of fluorescence dyes is growing rapidly. New dyes exhibiting different photophysical, chemical and biological properties do not necessarily match exactly the available or integrated laser lines. Photostability is one of the most important properties when it comes to high resolution microscopy. In this case, a photostable dye is preferred instead of a dye which matches existing filter sets. To avoid bleaching is therefore also a question of flexibility and the ability to adapt the system to new, more photostable dyes. Other disadvantages are the limited range of designed optical densities (ODs) (especially dichroic mirrors), imperfect transmissions, and limited edge steepness (5 to 15 nm). The filters are susceptible to damage and attrition caused by exposure to mechanical load, heat, humidity and high light intensities, changing their spectral characteristics over time. The growing importance of white light lasers with their tunable excitation and STED capability also strongly demands for adaptive filter systems (Wildanger and others, 2008).

Because of the fixed spectral characteristics of standard dielectric filters, a tunable filter would be highly desirable. To date, there are adjustable filters such as tunable LC filters. These filters are based on rotating the incoming, linear polarized, polychromatic light dispersively. Then, the direction of the polarization becomes wavelength-dependent and the desired wavelength can be selected by rotating an analyzer. Other wavelengths are partially blocked because of their non-parallel orientation with respect to the analyzer. Repeating these steps leads to increased filter efficiency. With the help of liquid crystal variable retarders, the bandpass can be shifted without any mechanical motion of the optics by adjusting the voltage. However, the major drawback of these devices is the poorly polarized peak transmission of 40 to 60% depending on the wavelength. The band width is typically in the order of a few nanometer, the switching speed below 100 ms (Meadowlark optics, Frederick, USA).

Another way to tune filter properties is the application of acousto-optic which was also chosen for the setup described here. AOTFs for microscopy are typically made of a birefrigent material like quartz or tellurium oxide which is coupled to a piezoelectric transducer (Fig. 3.4a). By feeding an oscillating radio frequency electric signal to the transducer, an acoustic wave is generated propagating through the crystal.

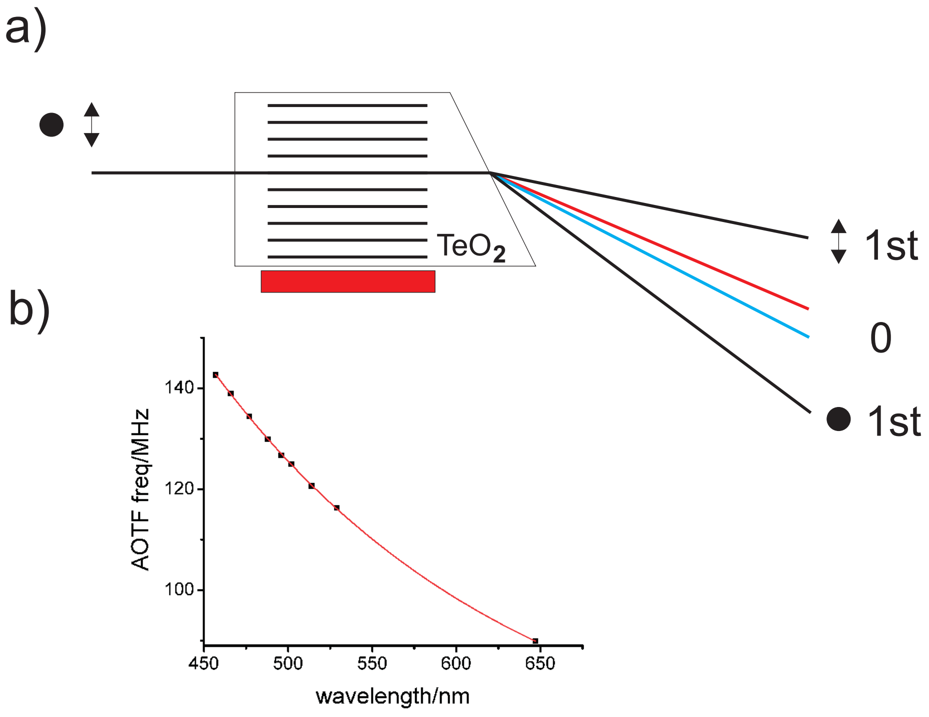

Fig. 3.4: An ultrasonic wave originating from the transducer penetrates the dispersive Tellurium oxide crystal, and periodically modulates the crystal´s refractive index (**a**). This diffraction grating deviates the beam into a first order beam depending on the original polarization. The AOTF changes the polarization of the diffracted beam by 90° relative to the incident beam. (**b**) shows the dependence of the diffracted wavelength from the radio frequency.

This acoustic wave induces a periodic variation of the refractive index in the crystal that acts as diffraction grating. The diffraction grating deviates a certain wavelength into a first order beam which is fed into the microscope. By changing the radio frequency of the transducer signal, the period of the refractive index variation is altered as well as the wavelength of the diffracted light. Fig. 3.4b shows the relationship between the diffracted wavelength and the radio frequency of the electric signal fed into the transducer for the AOTF used in the setup. The AOTF frequency (ν) can be calculated using the following empirically gained formula:

$$\nu = A \cdot B^{-C\lambda} + D \tag{3.1}$$

λ denotes the wavelength of the light to be diffracted, A, B, C and D are constants determined as: 1003.40, 1.00435, 1.265, 61.15, respectively. The intensity of the first order beam depends on the amplitude or power of the signal coupled into the crystal. Another prominent attribute of the acousto-optic tunable filter is the possibility to change the intensity or the diffracted wavelength very rapidly which is important for the RESCue modality discussed in chapter 4. The here employed AOTFs allow for changes well below 10 µs only limited by the acoustic waves´s transit time through the crystal.

The optical setup introduced here features four AOTFs for dispersive and birefringent compensation (Fig. 3.5a). The prism-like layout of the AOTF leads to dispersion. Compared to tunable liquid crystal filters, the AOTFs exhibit a high diffraction efficiency of 96% measured on narrow Ar-Kr lines (this corresponds to the transmission of the tunable liquid crystal filter) and a three times higher optical density (OD6). One disadvantage of the high spectral resolution of about 2 nm (Fig 3.5b, FWHM of the dips) lies in the incomplete spectral coupling of diode lasers into the microscope since these lasers exhibit broad lines in the range of 2 to 8 nm for wavelengths under 900 nm. Applying more than one frequency for diffraction to the AOTF leads to a diffraction efficiency of 50% for diode lasers. If the frequencies are too close, they disturb each other resulting in decreased diffraction efficiencies. The usage of clean up filters in the excitation and signal suppression beam path to remove potentially background generating light is redundant due to the high spectral resolution of the AOTFs.

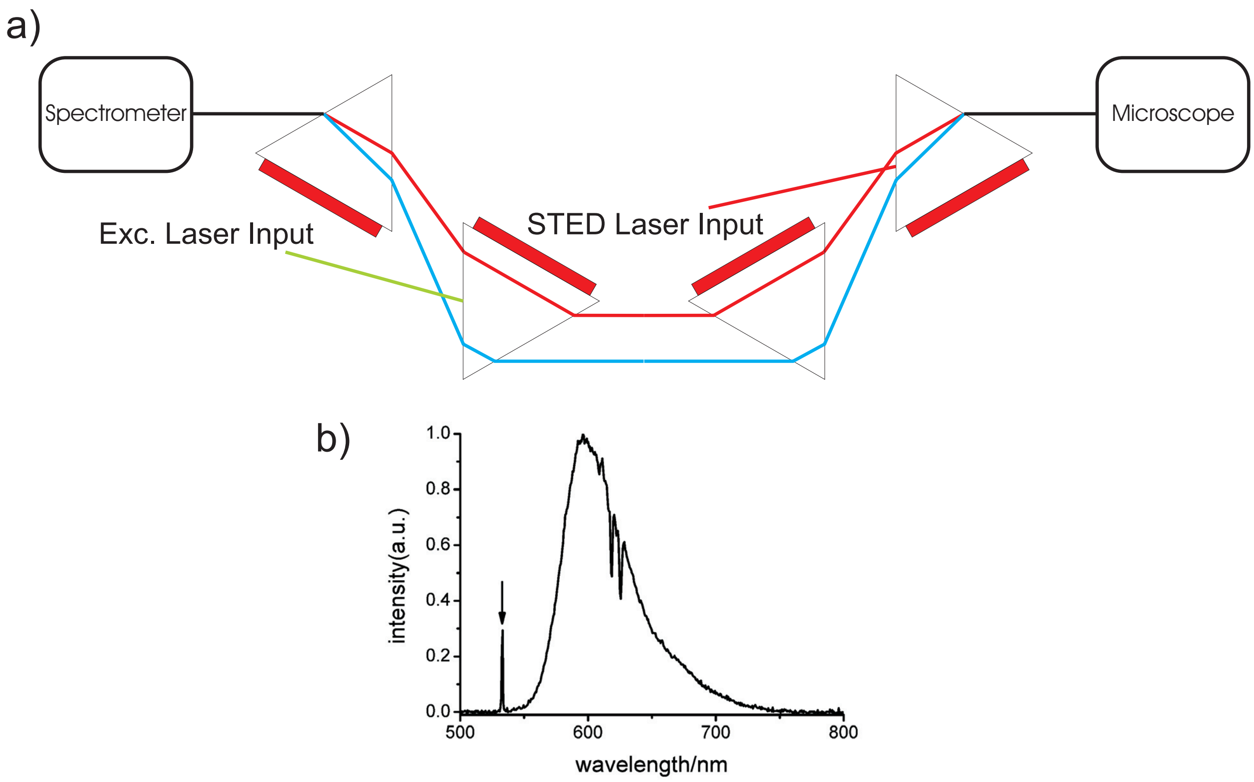

Fig. 3.5: The quadruple AOTF arrangement acts as an acousto-optic beam splitter or freely programmable dichroic (**a**). Multiple laser lines can be coupled into the microscope via the diffracted beam path without the need for realignment. The dispersion as well as the birefringence are fully compensated for the arrangement. (**b**) shows a fluorescence spectrum of the Atto565-NHS dye in DMSO measured after its passage through the AOTF arrangement. The arrow marks the unfiltered excitation line at 532 nm. The first AOTF is programmed to a radio frequency of 95MHz corresponding to a diffracted wavelength of around 625 nm and 618 nm. The fluorescence is usually unpolarized resulting in two diffracted wavelengths 7 nm apart in combination with the birefringence of the crystal. The FWHM of the two dips reveal a spectral resolution of the AOTF of about 2 nm. The quadruple AOTF arrangement is the first part of the adaptive filter system.

The fluorescence loss caused by the whole quadruple arrangement is around 8 %. The AOTF ensemble represents a tunable dichroic mirror for multiple laser feeding with linear polarization and narrow line width. The suppression of the remaining laser light in the fluorescence path is better than $1*10^5$. In the case of laser light (514 nm) reflected on a mirror installed in place of the sample, the suppression is even in the range of $1*10^6$ to $1*10^7$. Fig. 3.5b shows the fluorescence of Atto565-NHS in dimethyl sulfoxide (DMSO), the two dips around 622 nm correspond to the wavelengths which are filtered out by one AOTF operating at the frequency 95MHz. There are two dips in the spectrum, because of the birefringent properties of the crystal. The two different polarizations propagate in slightly different directions therefore facing slightly different lattice constants. The excitation wavelength at 532 nm is not filtered out in this case.

Prism based spectrometer

The AOTF quadruple arrangement is not sufficient to provide a satisfying suppression of the intense STED laser beam. Therefore, the fluorescence light is further filtered by a prism based spectrometer (PBS). Fig. 3.6a outlines the spectrometer setup.

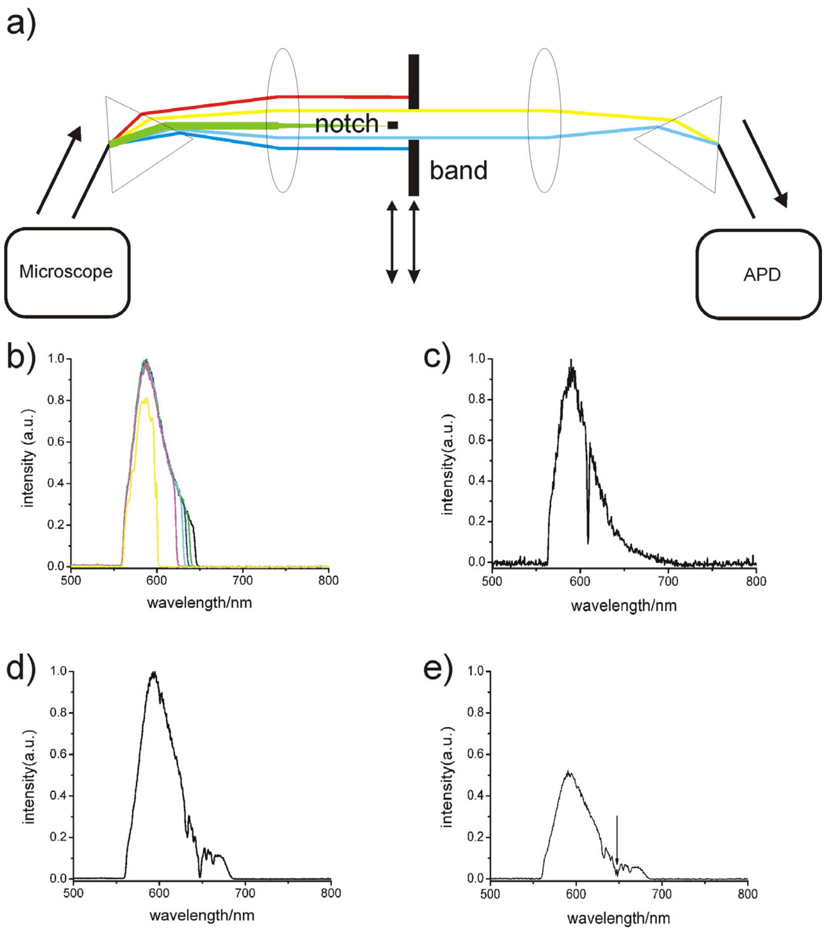

Fig. 3.6: The spectrometer shown in (**a**) is the second part of the adaptive filter system. After passing the quadruple AOTF arrangement the fluorescence is spectrally dispersed by a prism (SF10, triangle) and focused by a lens (oval) to a sharp line spectrum. The focus of the lens is an image of the fluorescence within the confocal pinhole. The line spectrum visualized in Fig. 3.2b can be filtered with movable plates and a narrow stop (200 µm). The STED beam, which is approximately 10000 times more intense compared to the excitation beam, is focused onto the stop (shown) or plates to remove it by blocking. Applying the strip is equivalent to using a notch filter. In this case the fluorescence on the red side of the

STED line can also be detected. (**c**) shows the spectrum of Atto565 (confocal) after passing the adaptive spectrometer filter. A sharp line at 609 nm with a FWHM of 2.5 nm is filtered out of the spectrum. The plates are equivalent to a bandpass filter. (**b**) shows the Atto565 spectrum (non-confocal) confined by sequentially moving in a plate starting from the red side of the spectrum. The yellow band corresponds to the band passing the normally used filter (580/40). The integral is significantly smaller than the integral of the band produced with the adaptive spectrometer filter. The adaptive filter allows one to exactly remove a signal suppression line located at 647 nm without preventing too much fluorescence from reaching the detector. (**d**) shows the Atto565 spectrum (non-confocal) with the whole adaptive filter system applied. The band around 647 nm is completely filtered out. (**e**) switching on the STED beam (647 nm) leads to a decreased fluorescence intensity, the STED line gets visible as a tiny signal within the filtered narrow band marked by the arrow.

While passing the prism (SF10), the fluorescence spectrum of a dye is dispersed. After focusing with a lens (f = 500mm), the spectrum can be seen as a 10 to 20 mm wide, sharp line (Fig. 3.2b) which can be manipulated via apertures or stops. The sharp line corresponds to the spectrum of the fluorescence within the confocal pinhole. For letting only a certain fluorescence band pass, two plates are introduced from the sides. Fig. 3.6b depicts the situation of a plate brought in from the red side of the fluorescence of Atto565-NHS in dissolved DMSO (non-confocal). The spectral resolution is in the range of 80 µm per nm, so it is easy to adaptively manipulate the cut-off of the spectral band with nm resolution. The spectral resolution is strongly dependent on the refractive index of the prism´s glass. Using BK7 glass instead of SF10 would lead to a spectral resolution which is only 30% percent of the resolution achieved with the SF10 prism. In return, a larger spectral width would be accessible, allowing multicolour analysis (described below). In the following, only the SF10 Prism was applied, which provides a 120 nm band (Fig. 3.6d) which is sufficient for standard fluorescent dyes and limited by apertures and edges of lenses and mirrors.

Another possible filtertype which can be realized with the spectrometer is the notch filter. The notch filter attenuates a very sharp wavelength band and lets other wavelengths pass unaltered. It is the opposite of a bandpass filter. To notch a certain, 2.5 nm narrow band in the fluorescence spectrum for filtering out a very intense STED wavelength for example, a 200 µm wide, and 20 mm long slit with a 200 µm broad strip in the middle was produced with an Nd-YAG laser cutting process (Metaq GmbH, Wuppertal, Germany). Fig. 3.6c shows the spectrum of Atto565-NHS in DMSO (confocal), where the strip filters out a narrow band around 609 nm by blocking these wavelengths. In a STED or RESOLFT experiment, the signal suppression beam is focused directly onto the strip. This leads to an attenuation of the intensity by a factor of 770 measured with the 514 nm laser line of the Ar-Kr-laser reflected from a mirror. Light diffracted by apertures, lens edges, the strip and mirror edges is the main source of bleed through. To combat this diffracted light, the fluorescence is coupled into a 62 µm fiber (Thorlabs, Cambridgeshire, UK) which is directly connected to an APD to sort out unfocused, diffusely scattered or diffracted light. The introduction of an additional pinhole (a multimode fiber) into the detection system leads to a further attenuation of the signal suppression beam by a factor of 530. The overall attenuation of the laser beam due to the spectrometer setup is then $4*10^5$. Combined with the quadruple AOTF arrangement an attenuation of $4*10^{11}$ to $4*10^{12}$ was obtained. For comparison, a standard thin film interference filter exhibits an OD of 6. Fig. 3.6d shows the Atto565-NHS spectrum with the whole filter system (spectrometer and tunable dichroic) enabled. A clear deep spike is distinguishable at 647 nm, the STED wavelength for the Atto565 dye. If the 647 nm laser line is switched on additionally, the fluorescence is depleted, which is manifested by a decreased fluorescence intensity (Fig. 3.6e). A tiny signal is visible in the notch, which is due to break through of the intense STED line. The overall reflection loss within the spectrometer is around 30% measured at 647 nm with the phase plate installed. The fluorescence spot is significantly smaller than the doughnut-shaped beam and therefore apertures do not block that much intensity. The reflection loss is estimated to be 25%. The SF10 prisms are coated with an anti-reflex coating (ARB2) to minimize the reflection loss to 2.7 to 3% for unpolarized light at an angle of incidence of 60° (Linos Photonics GmbH & Co. KG, Göttingen, Germany). The anti-reflex coating spans across a range from 500 to 750 nm. In combination with the tunable dichroic, which exhibits a reflection loss of 8% (2% for each AOTF) the overall reflection loss of the filter system is on the order of 30 to 35%.

If the number of fluorescence photons collected by applying the adaptive filter system is greater than the number using the fixed thin film interference filters, the light dose for excitation of the dyes can be reduced compared to the fixed filter system. Thereby, photobleaching can be minimized. With other words, perfect filtering, which is only achievable by an adaptive filtering helps to reach a sufficient SN with a lower excitation dose and therefore helps to prevent photobleaching. Especially for STED microscopy, intense light has to be removed which is spectrally located within the red end of the emission. Usually, all the fluorescence light ranging from the STED line to the red end of the dye´s spectrum is filtered out. With the aid of an adaptive notch filter, the fluorescence to the red side relative to the STED line can also be collected. Depending on the dye, this fraction can account for up to

40% of the fluorescence intensity. Interestingly, by applying the adaptive notch filter to STED measurements of Nile red beads (the sample was produced following the protocol described in the appendix A.1.1) the background was significantly raised by a factor of 20 to 50 (Fig. 3.7).

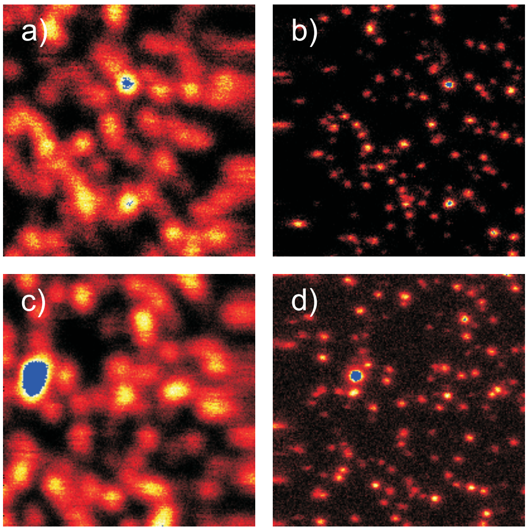

Fig. 3.7: A comparison of confocal ((**a**), (**c**)) and STED ((**b**), (**d**)) images of Nile red beads embedded in Mowiol and excited at 532 nm. The STED wavelength was 647 nm. The images (**a**) and (**b**) were recorded applying a thin film interference filter (580/40). The background is 1kHz. The images are slightly shifted with respect to each other because the scanner´s fly back creates the confocal image. The images (**c**) and (**d**) were taken using the adaptive filter system based on the strip. A significantly increased background of 25kHz is apparent. Spectrally opening up the detection window may sensitize the system to *Raman* scattering originating from the embedding media.

The additional background may originate from STED-beam induced, *Raman* scattered light in the embedding media spectrally located on the red side of the fluorescence spectrum and will be investigated in more detail in the future.

Fig. 3.8 shows a STED experiment on Nile red beads measured with the adaptive filter system (Fig. 3.8c, d), and with a disabled filter system but with an implemented thin film interference filter (580/40) (Fig. 3.8a, b). For the adaptive filter recordings a band was applied (see Fig. 3.6b).

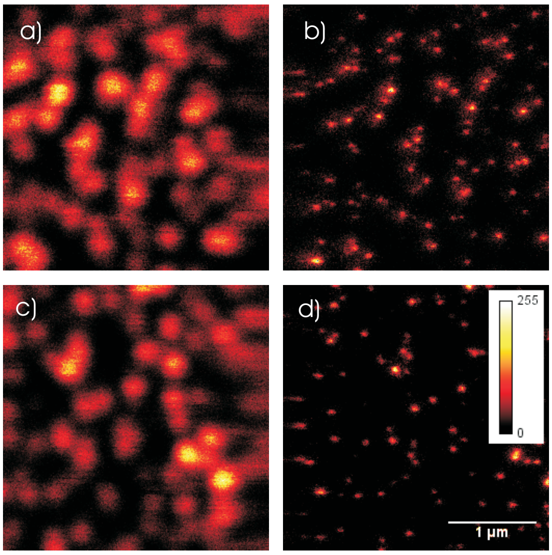

Fig. 3.8: The same experimental series as in Fig. 3.7 has been carried out here. This time, instead of the bar, the adaptive filter system based on the plate was applied to simulate a bandpass filter. The background levels of all measurements are comparable.

The fluorescence intensities of the images recorded with the adaptive filter are comparable to that recorded with the fixed bandpass filter. The background levels are also comparable. These findings are also appropriate for Atto565-phalloidin labelled actin filaments in SupT1 cells (Fig. 3.9) (for preparation see appendix A.1.2).

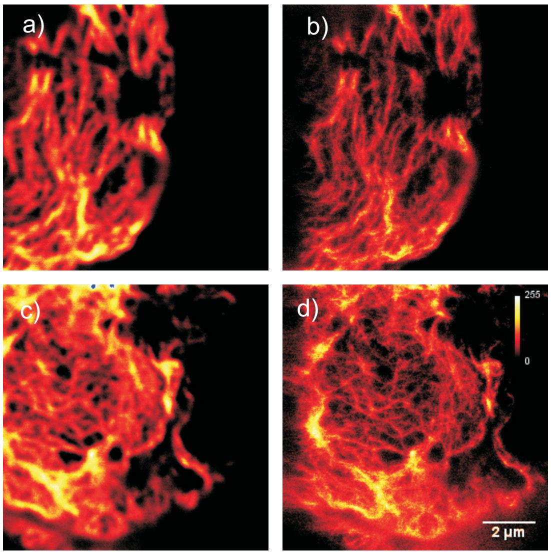

Fig. 3.9: A comparison of Atto565-phaloidin labelled actin filaments in SupT1 cells recorded in confocal mode ((**a**) and (**c**)), and STED mode ((**b**) and (**d**)). To record the images (**a**) and (**b**) a bandpass filter was applied (580/40). The images (**c**) and (**d**) were taken using the adaptive filter system based on the plates. The background levels of all images were comparable. All images were processed by subtracting a background of 10%.

In conclusion, the application of the notch-like adaptive filter results in extra background, presumably generated by converted STED light and spectrally located within the red end of the dye´s fluorescence spectrum. Replacing the notch-like adaptive filter with the adaptive band pass filter removes all the background light. The measurements of the polystyrene (Nile red) beads and SupT1 cells prove the applicability of the adaptive filter system. A drawback of this system is the time-consuming alignment procedure of the spectrometer part. The whole adaptive filter system can however be automated. For the determination of the optimal AOTF frequencies an iterative algorithm can be applied to optimize the diffraction and filtering of the signal suppression wavelength. Within the spectrometer part, the apertures and the strip can be motorized.

For the experiments in the following chapters thin film interference filters were used.

3.2.2 Tunable phase filter and Simple STED

Conventional phase plates are not tunable and different phase plates for different wavelengths are required. The phase plates are produced by vapor deposition of MgF_2 on a glass substrate or a laser-writing process. The thickness of the coating has to be adapted to the desired wavelength. For the Ar-Kr-laser a whole set of phase plates must be provided to take advantage of all laser lines and to fully exploit the above mentioned flexibility. A tunable phase filter is therefore highly desirable.

In the following, a new approach to create a 180° phase step midway through the signal suppression beam with the aid of two identical adjacent optical flats is described (Fig. 3.10a, b). The signal suppression beam passes the optical flats, which are slightly tilted with respect to each other. Due to dispersion, a difference in the optical path lengths between the two halves of the beam is introduced. If the difference of the optical path lengths equals $\lambda/2$, a zero line is generated in the focus. The phase plate can be tuned to match every laser line (every λ) by simply tilting the whole arrangement.

During the investigation of the new phase plate approach, a way to significantly simplify a RESOLFT setup was found (simple STED). The excitation and the signal suppression beams can be provided by the same laser or fibre source without the need for separating the laser beams with dichroic mirrors to place a phase plate in the beam path of the signal suppression laser. The tilting of the two optical flats has to be adjusted in such a way, that a phase step of

180° is created for the signal suppression beam, and a phase step of 0° is created for the excitation beam (Fig. 3.10).

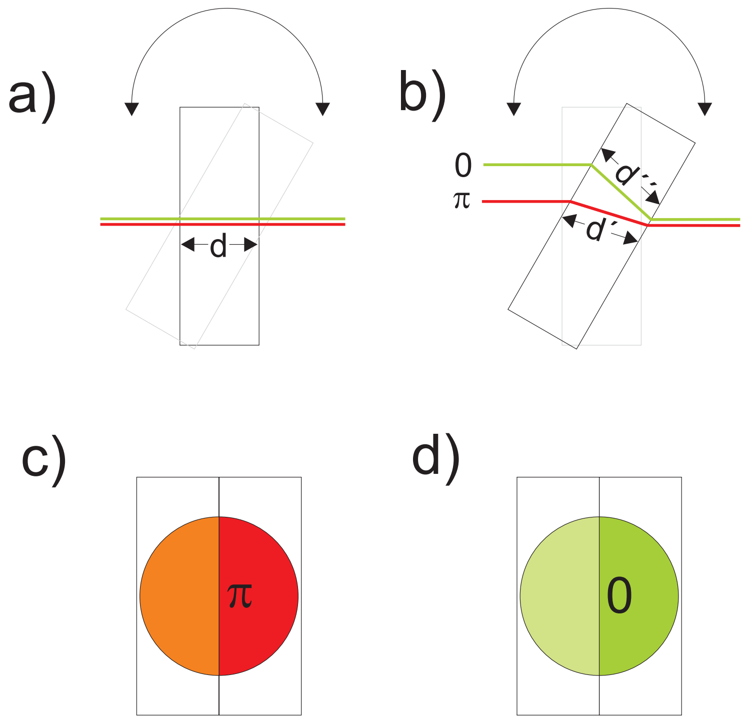

Fig. 3.10: A linear polarized beam (red or green) passing the two adjacent optical flats which are slightly tilted with respect to each other is modified by a freely adjustable phase step midway through the signal suppression beam. (**a**) and (**b**) shows the situation for each individual flat. The differences in the optical path lengths (d to d`or d``) through each flat are tunable by turning the whole arrangement. For a zero line in the focus, a phase step of 180° is necessary (**c**). Because of dispersion there is a certain tilt angle causing a 180° phase step for the signal suppression beam (**c**) and a phase step of zero for the excitation beam (**d**) simultaneously.

The time-consuming alignment procedure to overlay two foci in the sample would be redundant, because both laser beams are inherently aligned due to the fact that they are originating from a single laser or fibre source. The dispersion of the optical flats used allows the adjustment of the phase of one half of the beam relative to the other and relative to a second beam. Fig. 3.11 shows a typical PSF in the *xy* and *xz* plane (Fig. 3.11b, a) of the signal suppression beam (red) with a wavelength of 647 nm and the excitation beam with a wavelength of 514 nm (green) shaped simultaneously by the two optical flats. This enables for one-dimensional high resolution imaging. The *xz* section reveals that the foci are shifted relative to each other by 120 nm because of residual chromatic aberrations of the objective in *z* direction. The applied objective lens has to provide a superior foci correction like the one described above in the setup section. Alternatively, a custom designed lens has to be placed in the beam path to compensate for the chromatic dependence of the focal length. The line profile through the *xy* section (Fig. 3.11c) proofs that the zero intensity is below 0.5%.

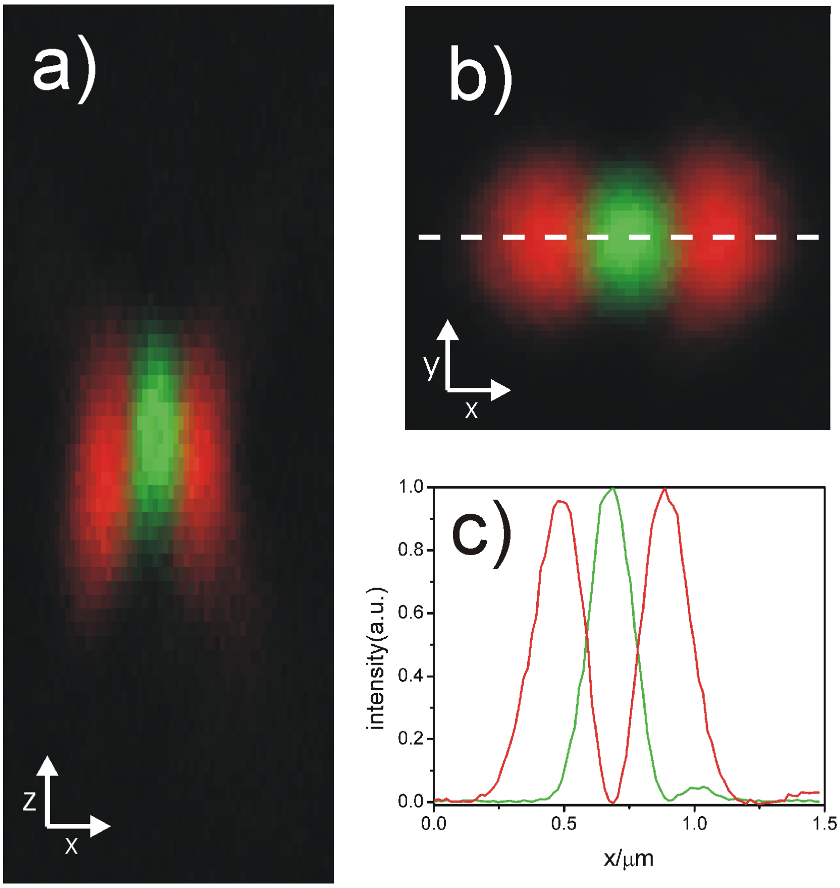

Fig 3.11: z (**a**) and *xy* (**b**) section showing the excitation (514 nm) PSF colored in green and the STED PSF (647 nm) colored in red. Both lasers operate in cw mode. The PSFs were recorded by scanning a 80 nm gold particle. (**c**) The line profile through the XY PSFs proves a good zero (<0.5%).

The method to generate a zero introduced here is particularly suitable for setups using different wavelengths for signal suppression. The adaptation to different laser lines is accomplished simply by rotating the two optical flats and is fast and reliable. The possibility to exactly match every desired wavelength compared to other phase plates suitable for only one wavelength is an advantage when improving the overall performance.

The new phase plate was applied to resolve Nile red beads (Fig. 3.12), which were excited by the 514 nm laser line. Stimulated emission was performed by the 647 nm laser line. The FWHM of some Nile red beads which are not clustered are around 40 nm. Both laser lines originate from the same Ar-Kr-laser, making beam alignment redundant. Images were taken with lasers in cw mode which is mandatory because adjustment for the timing between excitation and STED laser pulses is not possible when using the same laser as excitation and de-excitation source.

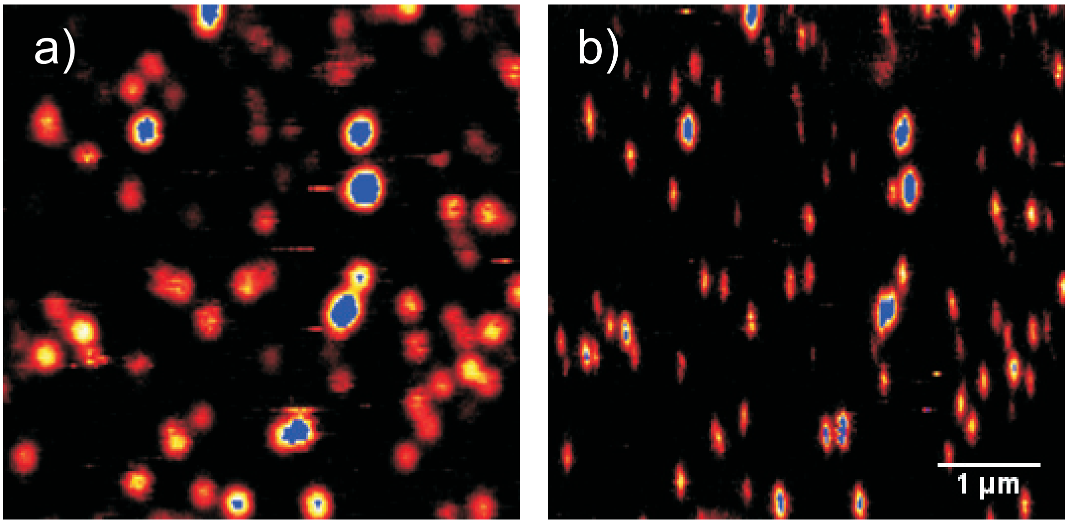

Fig. 3.12: Comparison of Nile red beads imaged under confocal mode (**a**) and STED mode (**b**). Features in the range of 40 nm are discernable.

For two-dimensional high resolution imaging, a second set of two adjacent optical flats is necessary. The beam would be split into two beams with crossed polarizations passing two phase plates thereby generating a zero in *x* and *y* direction when focused. Next, the two beams would be merged again by a polarizing beam splitter and fed into the microscope.

The tunable phase filter introduced here covers the whole visible range and simplifies the STED setup in combination with the application of cw laser beams due to redundant PSF and timing alignment procedures.

Chapter 4

Reduction of excitation and signal suppression cycles (RESCue) in zero based high resolution optical microscopy

Most of the destructive processes are dependent on the light dose. When an object is scanned by the laser beams in a RESOLFT type of microscope, many parts of the object are exposed to and therefore affected by the light, even though they are momentarily not contributing to the signal. This leads to the consideration, that the sample has to be exposed if and only if the desired object is present in the effective focal spot. Accordingly, it is possible to reduce the overall dose affecting the sample with the aid of an algorithm which switches off the lasers whenever possible. To accomplish this, each pixel is initially exposed for a short time-period in order to determine whether a certain number of fluorescence photons are emitted and whether further exposition of this particular spot is worthwhile.

In zero based high resolution methods the dye molecules not present in the zero are forced into the non-fluorescent state. If the non-fluorescent state has to be maintained during the readout of the signal, the dye molecules undergo a high and finite number of excitation and/or signal suppression cycles, which is the major drawback of using a metastable non-fluorescent states. After each cycle the dye molecule makes a transition into a dark or triplet state with a probability unequal zero. The higher the cycle number, the higher the probability to end up in these states, which are well known precursors for bleaching pathways. If the cycle number is too high, the acquisition of a high resolution image is hindered. Therefore the reduction of the number of switching cycles addresses a fundamental problem in zero based high resolution microscopy using metastable off-states.

In this chapter, a strategy is described for reducing photobleaching in zero based high resolution optical microscopy by instantaneous coupling of the sample exposure to the high resolution information.

4.1 Principles of RESCue

Developing an appropriate scan algorithm to reduce the overall dose inside a 3D specimen is a straight consequence of the primary attribute of the zero based RESOLFT techniques to excite and quench the fluorescence in a much larger volume than the volume emitting fluorescence. It is obvious that the excitation as well as the fluorescence-depleting beam stress a much greater diffraction-limited volume than the small volume actually emitting fluorescence. The modality introduced in this chapter significantly decreases the amount of light hitting the sample and therefore reduces bleaching of fluorescent dyes and phototoxicity in case of living cells.

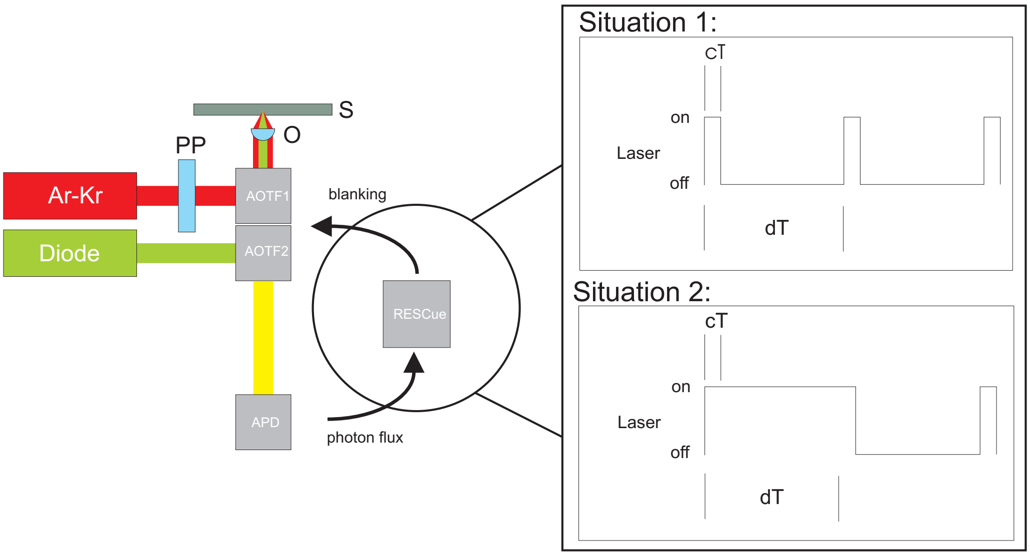

Fig. 4.1: Setup for the RESCue-STED experiments (see also Fig 3.2). The excitation and the STED laser beams pass an AOTF to switch the laser light on and off during the RESCue experiments depending on the RESCue control, are then coupled into the microscope using two beam splitters (BS) and are focused into the sample (S) via an objective lens (O). A vortex phase plate (PP) is placed in the beam path of the STED laser to create a doughnut-shaped beam profile. The fluorescence is collected by an APD measuring the photon flux, which is interpreted by the RESCue control driving the AOTFs. Two situations have to be considered (right side): *Situation 1*: the lower threshold (lTh) is not reached during the cycle time (cT) (a dye is not present OR the fluorescence of the dye is depleted). The lasers are switched off during the dwell time (dT). *Situation 2*: the lower threshold is reached during the cycle time of the first dwell time (a dye molecule is present in the effective fluorescence region). The lasers are switched on.

The number of photons originating from the fluorescence volume is determined for the cycle time (cT) which is a small fraction of the pixel dwell time (dT) (Fig. 4.1). In case that this number is below a certain lower threshold (lTh), the binary decision is made that no dye-labelled object is present in the shrunken effective fluorescence volume. Any further exposure would not increase the signal-to-noise ratio (SN) of the image but only stress the dye molecules present in the whole diffraction-limited illumination volume as well as the fluorescent molecules above and below the focal plane. Therefore, both the excitation and the quenching beam are shut off for the residual dwell time (dye-depending, blanking of only the excitation beam may be sufficient) (Fig. 4.1). Alternatively, one could proceed the scan immediately to the next detection volume reducing data acquisition time. The reduction of the number of switching cycles due to the lower threshold depends mainly on the dT/cT ratio, the fluorescence distribution and the volume ratio of the conventional PSF to effective PSF. As the resolution of the system increases, the size of the effective PSF decreases, which results in the possibility to detect the fluorescence distribution more accurately and to simultaneously increase the ratio between the illumination-stressed volume and the effective fluorescence volume (Fig. 4.2). If the resolution of the system is higher than the diffraction limit, it is possible to switch off the lasers between adjacent fluorescent objects with a distance smaller than the diffraction limit (Fig. 4.2). Only if an object is present with a certain accuracy defined by the resolution of the system the lasers remain switched on. A better resolution also gives the possibility to accurately control the sample exposure and the local dose and thus to decrease photobleaching compared to the confocal mode. The principle of STED allows for adaptive bleaching control depending on the photon flux of only a fraction of the illuminated volume. Including a similar illumination decision and detection feedback as presented by Hoebe et al. (controlled light exposure microscopy, CLEM), one obtains a simple rule to control the illumination of the specimen. Hoebe et al. presented a method where phototoxicity and photobleaching are reduced in the focal plane of a conventional confocal microscope by collecting the photons point by point up to a certain threshold, which is still high enough for a sufficient signal-to-noise ratio. By using a lower threshold photobleaching is reduced in the out of focal planes (Hoebe et al., 2007). The combination of the illumination strategy based on the lower threshold with zero-based subdiffraction microscopy makes a reduction of photobleaching within the focal plane feasible. The lasers are shut off at regions where the signal gets quenched.

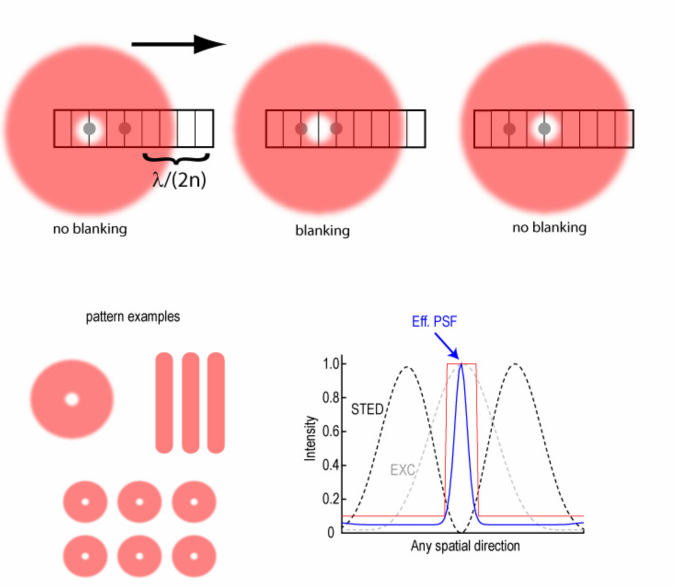

Fig. 4.2: A high-resolution beam featuring an intensity zero (red) scans across two subdiffraction-sized objects (grey circles) which are separated by half the diffraction limit. The lasers remain switched on for the whole dwell time only if an object is present in a subdiffraction-sized area. The two fluorescent objects are not resolvable by a conventional confocal microscope (limit: $\lambda/(2n)$, the grid marks the pixels, the beam is scanned from left to right). If the read-out of the fluorescence is confined to the zero of the lasers beam profile inhibiting fluorescence (red, any zero pattern, for example multiple doughnuts or grooves), the objects are resolvable and the lasers can be blanked in regions where no fluorescence is emerging because of the fluorescence inhibition (between the two objects) (*middle*) or the absence of fluorescent molecules. A narrower effective PSF yields the possibility to expose the sample more accurately. The number of cycles a fluorescent molecule undergoes in the RESCue-STED modality is strongly reduced compared to the cycle number in the conventional STED mode (red line) related to cT/dT, the systems resolution and the distribution of the fluorescent molecules.

The lower threshold is implemented by a stand-alone circuit board (Fig. 4.3). The pixel clock (J1) provided by the multichannel analyzer (MCA) board (FAST ComTec Communication Technology GmbH, Oberhaching, Germany) switches on the laser (J8) via a mono flop (U1A). At the same time, the RS flip flop (U2) and the binary counter (U5) are cleared. If the collected photon (J5) count during an adjustable time span is below a certain threshold which can be adjusted to a value 2^n by the binary counter (U5), the laser will be blanked (J8) by the AOTFs (see also chapter 3) after the operation of the mono flop. The duration the mono flop stays in the high level can be adjusted by a potentiometer (J9). In case that enough photons have been counted, the RS flip flop keeps the lasers switched on also after the mono flops has switched to low. The MCA board collects the pulses from the APD caused by detected photons and is controlled by the data acquisition software Imspector (MPI Göttingen, Germany). The scanner´s fly back signal J7 is provided by the software Imspector and blanks the laser via a NAND gate (U4).

Alternatively a field programmable gate array (FPGA, National Instruments, Austin, USA) is used to implement the lower threshold and additionally takes over the scan control instead of Imspector (Staudt et al., in preparation).

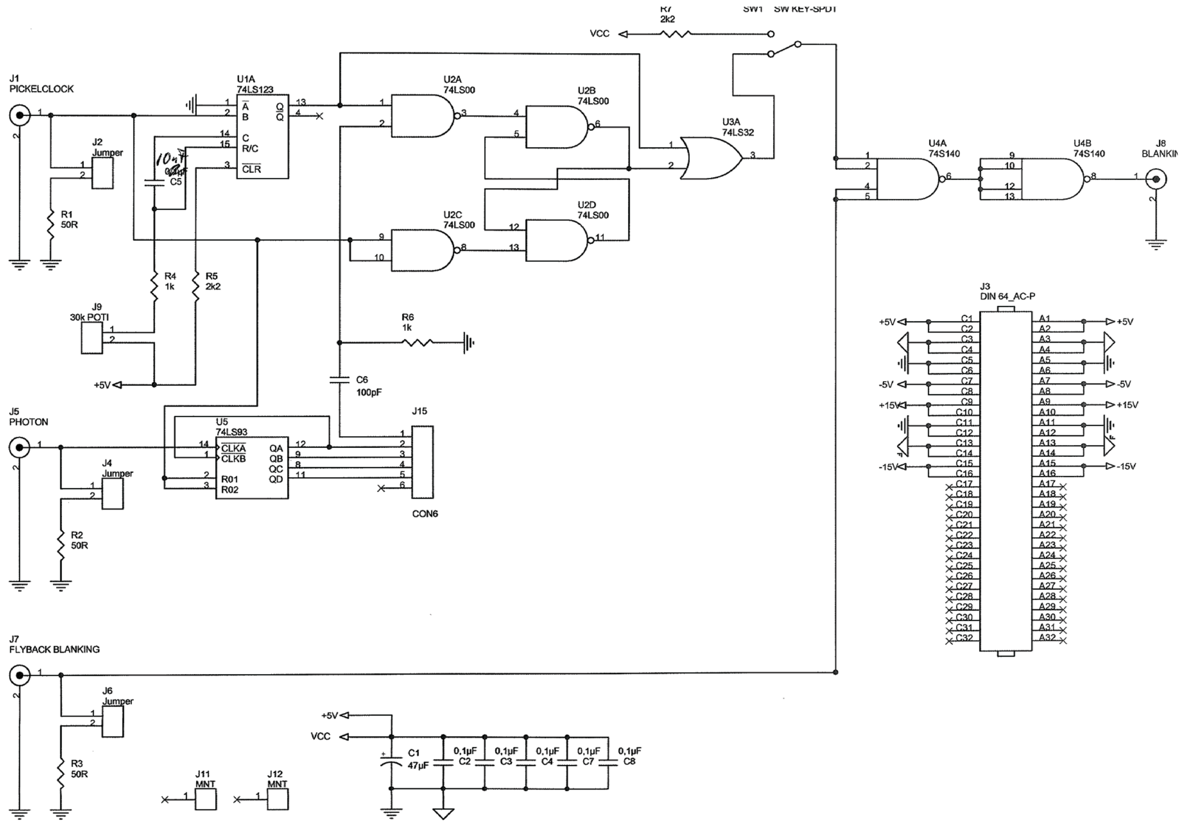

Fig. 4.3: The lower threshold is implemented by a stand-alone circuit board, which utilizes a binary counter (U5) to track the photons measured during the cycle time by a detector device synchronized with the pixel clock. This information is then used to decide on the operation of both illumination beams.

4.2 Materials and methods

4.2.1 Optical setup used for the Nile red, Atto565 and coumarin experiments

Pulsed excitation of the antibodies labelled with Atto565 (Atto-Tec, Siegen, Germany) or Nile red beads (Molecular Probes, Carlsbad, USA) was achieved using a high-repetition rate pulsed amplified laser diode source (PicoTA, Picoquant, Berlin, Germany) at a wavelength of λ_{exc} = 532 nm. Dy-485XL (Dyomics GmbH, Jena, Germany) was excited by the 470 nm line from a pulsed high-repetition rate laser diode source (PicoTA, Picoquant, Berlin, Germany). The coumarin derivatives Atto390 (Atto-Tec, Siegen, Germany), C6H and C522 (Lambda Physik AG, Göttingen, Germany) were excited by the 405 nm line, and Atto425 (Atto-Tec, Siegen, Germany) and Dy-415 (Dyomics GmbH, Jena, Germany) by the 440 nm line from pulsed high-repetition rate laser diode sources (PicoTA, Picoquant, Berlin, Germany). Fluorescence depletion was carried out at λ_{STED} = 647 nm for Atto565, Dy-485XL and Nile red, and λ_{STED} = 514 nm for the coumarin derivatives. The AOTFs enabled blanking of the lasers and allowed the power of each laser beam to be controlled independently. The collected fluorescence passed through an additional bandpass filter (580/40 for Atto565, Dy-485XL and Nile red, and 480/40 for the coumarin derivatives, AHF Analysentechnik, Tübingen, Germany) and was detected confocally with a photon counting module (SPCM-AQR-13-FC, PerkinElmer, Canada). A vortex phase plate (RPC Photonics, NY, USA) is used in the STED beam path to generate a doughnut-shaped point spread function in the focal plane (Fig. 4.1).

4.2.2 Optical setup used for the Atto647N related 3D experiments

The setup used is very similar to that in recent publications (Harke et al., 2008). The excitation beam wavelength was set to λ_{exc} = 635 nm, the detection was performed at 670 nm ± 20 nm. The STED wavelength was set to λ_{STED} = 750 nm. A phase plate retarding an inner part of the beam by $\lambda/2$ was used to generate the depletion pattern for pronounced resolution enhancement in the axial direction and a slight enhancement in the lateral directions. For detection, four photon-counting avalanche photodiodes (APD) (PerkinElmer, Canada) with multimode fibers were used in parallel to reduce saturation effects occurring with a single APD. In order to blank the lasers according to the RESCue modality described above, an electro-optic modulator (EOM) (LM002 P5W, Linos, Germany) was used to switch off the STED beam and an AOTF (PEGASUS OPTIK GMBH, Wallenhorst, Germany) was used to blank the excitation beam. Both devices were also controlled by the above-mentioned circuit board getting the pixel clock from a multichannel analyzer (MCA) board (Fast ComTec GmbH, Oberhaching, Germany).

4.3 RESCue-STED measurements

4.3.1 Resolution enhancement

A more intense STED beam leads to a higher resolution, but also to more severe photobleaching.

RESCue-STED in turn makes it possible to reduce photobleaching associated with increased intensities due to a more accurate sample exposure. To this end, photobleaching in this modality can be reduced compared to confocal imaging. The size of the effective PSF is an important parameter when photobleaching should be avoided. On the one hand, high STED intensities lead to a higher resolution (Harke et al., 2007) but also to more pronounced photobleaching. On the other hand, higher resolution and better localization makes a more accurate exposure possible and therefore offers a way to reduce the light dose on the sample. One of the ideas behind RESCue-STED is to reinvest the improved bleaching behaviour at higher STED intensities to push the resolution further. The resolution of the system was determined by imaging Nile red beads with a size of 21 nm (for preparation see appendix A.2.2)(Fig. 4.4a) which are well-characterized and offer stable and robust conditions for the measurement. The images were recorded with a pixel size of 12 nm in *x*- and *y*-directions and a pixel dwell time of 300 µs. It is obvious that the confocal image (Fig. 4.4a right side) provides no structural information of the bead distribution in the sample and does not display the real physical dimension of the fluorescent beads. However, the STED mode is clearly capable of resolving structures (Figure 4.4a left side) down to 30 nm and it can therefore be assumed that the resolution of the system is around 25 nm as the bead size of 21 nm convoluted with the PSF of the system would lead to sizes of around 30 nm. Compared to the confocal image, the STED image provides a 60-fold reduction of the spot size in the *xy*-plane.

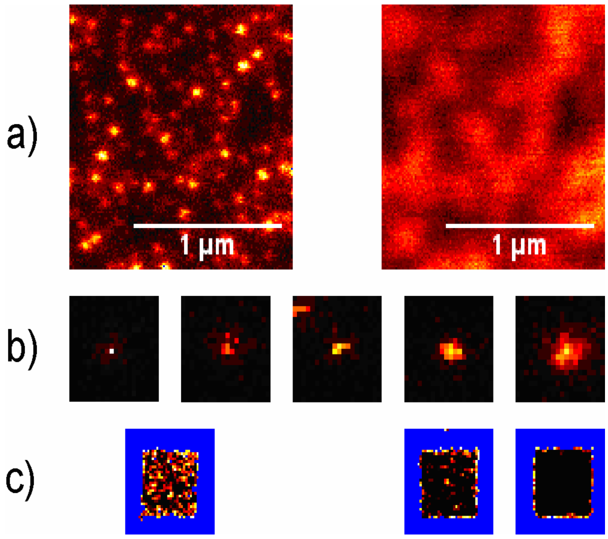

Fig. 4.4: The lower threshold and the cycle time influence the image appearance and photobleaching. In (**a**), a comparison of Nile red beads is shown in the STED mode (left) and the confocal mode (right). The apparent resolution enhancement is of vital importance for the effectiveness of the locally adapted sample exposure. (**b**) Increasing the cycle time (from left to right, cT = 90, 110, 200, 300, 500 µs , implemented by the circuit board; dT = 500 µs) leads to higher photobleaching (**c**) (area within the blue frame), the light dose affecting the sample gets higher according to cT/dT. Simultaneously, the number of pixels around the bead´s centroid reaching the kept constant lower threshold gets higher (**b**). At cT = 90 only one pixel reaches the lower threshold and is exposed for the full dwell time.

Two main parameters (lower threshold and cycle time) can be freely chosen to influence the image quality and to reduce photobleaching. To show the relations between the image appearance and the cycle time, Nile red beads were imaged with different settings for the cycle time (Fig. 4.4b from left to right: cT = 90, 110, 200, 300, 500 µs; dT = 500 µs). Decreasing the cycle time leads to a pronounced fluorescence conservation because the sample is exposed to a lower dose according to cT/dT (Fig. 4.4c) as discussed below. Simultaneously, the number of pixels around the bead´s center reaching the constant lower threshold during the cycle time gets smaller until no pixel at all reaches the lower threshold (Fig. 4.4b). The background in the images corresponds to pixels not reaching the lower threshold of 8 photons but representing the bead´s real size. A constant cycle time and an increasing lower threshold would lead to similar situation but better statistics because the time span for deciding the laser´s blanking can be chosen sufficiently long. As in every imaging modality the sample has to display a sufficiently high contrast allowing a reliable decision between the sub-diffraction localized object and no object at all. In the case of RESCue-

STED, the necessary cycle time is only a fraction of the dwell time and limits the SN and therefore complicates the decision whether an object is present or not.

The user or an automatic algorithm has to provide a reasonable lTh - cT combination which would include all objects of interest in the sample. The influence of the lower threshold parameter according to photobleaching during an image sequence of the same region of interest (ROI) turned out to be a fundamental point. As bleaching also occurs in the RESCue mode, later images exhibit reduced brightness. Ultimately, it is possible that the fluorescence could sink below the lower threshold. One has to decide whether this effect is desired. It would result in an adaptive RESCue effect to prevent the fluorophores from bleaching more and more and therefore sustain the fluorescence to more scans. However, it can be as important to track each and every object in every image even if it bleaches earlier. In this case the lTh - cT combination has to be adjusted for every scan according to the lower threshold of the last scan and the bleaching behavior of the specimen or the lower threshold is simply chosen in a way to include the objects even in the last scan. This can be achieved manually or by an adaptive algorithm. The cT must be long enough to allow a reliable decision whether the object of interest is present or not.

Different technical and biological specimen were measured to demonstrate the reduction of photobleaching due to the application of RESCue-STED compared to conventional STED. Therefore, a confocal overview of the sample was recorded. Within this overview two ROIs were scanned repeatedly. Each ROI represents different settings: conventional STED (no RESCue) and lower threshold enabled RESCue-STED (lTh). Afterwards a second confocal overview including these two ROIs was recorded displaying the bleaching behaviours according to the different (RESCue-)STED settings. In the case of the Nile red beads measurement an additional confocal series is recorded to proof the photobleaching caused by the excitation only.

4.3.2 RESCue-STED of fluorescent beads

A confocal overview of a Nile red bead sample (Fig. 4.5a) was taken. Each of the three ROIs was scanned 10 times in the corresponding STED, RESCue-STED or confocal mode (Fig. 4.5b). The ROIs were 4 x 4 µm in size, scanned with a pixel size of 15 x 15 nm and a pixel dwell time of 400 µs. The lower threshold was 5 photons and the cycle time 50 µs. After all ROIs were scanned, the second confocal overview scan was performed (Fig. 4.5c).

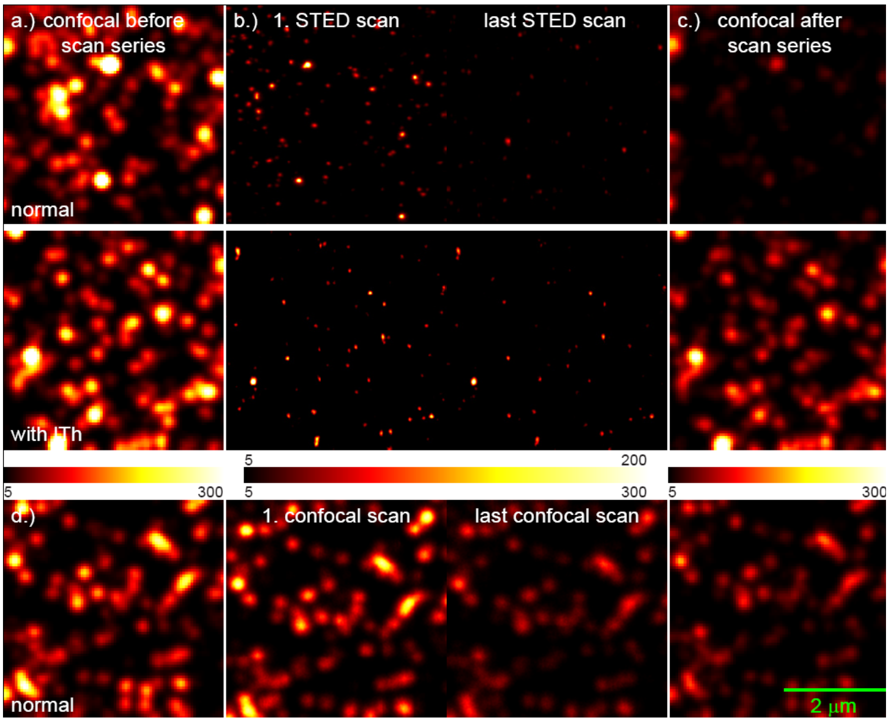

Fig. 4.5: Reduced bleaching in the RESCue mode by a factor of 4 exemplified by recording fluorescent Nile red nano-particles compared to the standard STED mode (normal), and a factor of 1.2 compared to the standard confocal mode (**d**). The confocal overview (**c**) presents the fluorescence of three ROIs, after a series of ten scans were performed in either STED or confocal mode (**b**). Each ROI is recorded with the same scan parameters but differs in its imaging mode. In the first ROI (normal) RESCue is disabled. The second ROI (lTh) is imaged with a lower threshold (FPGA implemented) of 5 photons and a cycle time of 50 µs. In the last row (**d**, normal) a series is shown to demonstrate the photobleaching caused by pure confocal imaging. The dwell time was set to 400 µs for all scans. The images of the first and the last STED (or confocal respectively) scan are shown for each parameter setting to demonstrate the preservation of the fluorescence due to RESCue.

The STED mode recognizes sharp dots of 30 nm FWHM while imaging the 21 nm beads. Compared to the confocal image, the STED image provides a 45-fold reduction of the spot size in the xy-plane. Photobleaching in the conventional STED mode is apparent by a 6-fold reduced fluorescent signal after ten scans (Fig. 4.5b normal). The high number of excitation and de-excitation cycles a dye molecule undergoes under STED conditions is associated with pronounced bleaching. Reduction of the excitation and STED beam dose by applying RESCue cuts back cycle numbers significantly. By introducing the lower threshold, an improvement of a factor of four was achieved (Fig. 4.5b lTh) regarding photobleaching. The deviations from the theoretical limit of the photobleaching reduction of dT/cT = 8-fold is mainly due to the limited resolution of the system and the dense dye distribution. A 4-fold reduction of photobleaching by applying RESCue in densely labelled samples was achieved. Comparing the photobleaching in the confocal mode (Fig.4.5d normal) to that of the RESCue mode taking advantage of the lower threshold, shows impressively the potential of instantaneously adapting the sample exposure to the high resolution information: 20% more fluorescence is saved in the RESCue mode compared to the confocal mode.

4.3.3 RESCue-STED of Atto565-labelled APP: sparse dye distributions benefit the most from the lower threshold

In the following, these promising results were transferred to biological questions. The amyloid precursor protein (APP) in primary mouse neurons (DIV8) was immunostained with Atto565 following a protocol which is described in the appendix A.2.1. APP is located in the dendritic and axonal compartment of neurons and essential for normal synaptic function and processing, which strongly depends on its intraneuronal localization (Back et al., 2007). APP plays a major role in the etiopathology of *Alzheimer's* Disease (AD). AD is the most common type of dementia in elderly people. Fig. 4.6 (first row) shows a confocal and a STED image of labelled APP located in the plasma membrane. The STED image displays well-separated APP spots in contrast to the confocal image. The resolution in the STED mode was around 45 nm and limited only by the available intensity of the STED laser.

Given the resolution of the microscope and the sparse structures of the immunostaining, a major impact of RESCue with a well-adjusted lower threshold is predictable (Fig.4.6, lTh). Six photons within 40 µs as lower threshold and cycle time respectively were chosen to be the best parameters. As before, a confocal overview was recorded with 50 nm pixel size and a dwell time of 500 µs. The two (RESCue-) STED ROIs were recorded with a dwell time of 300 µs and otherwise with identical settings to Fig. 4.5. As shown in the images, a 4-fold improvement regarding photobleaching between the RESCue measurement and the conventional STED measurement is obvious (Fig. 4.6d). It could be shown that APP is sparsely distributed over the specimen.

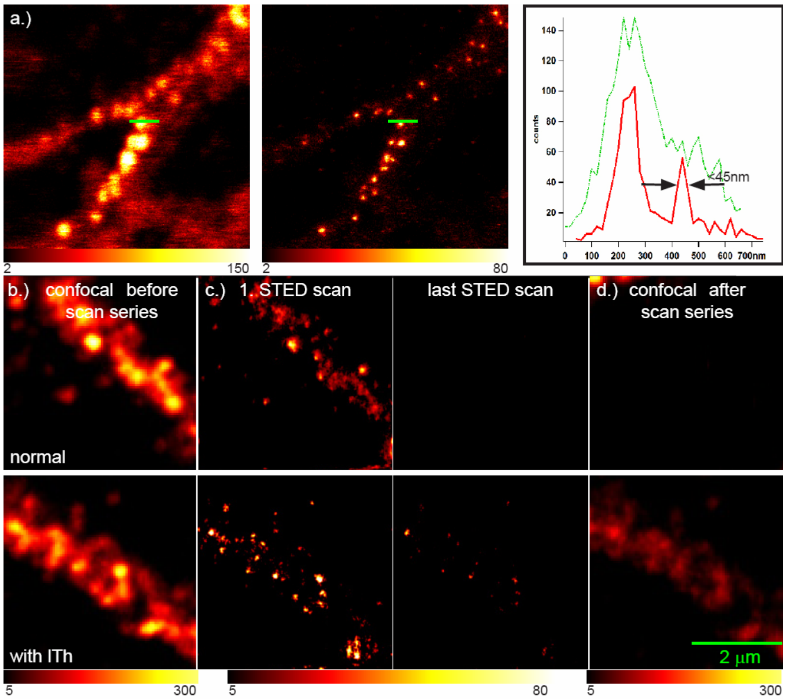

Fig. 4.6: Imaging in RESCue mode reduces the photobleaching of Atto565-labelled APP in fixed, permeabilized primary mouse neurons by a factor of 4. Confocal image (**a**, left side) of the APP distribution and STED data (raw) (**a**, middle). The line profile through the APP spot reveals a resolution of 50 nm (**a**, right side). The confocal images (**b**) represent the situation before all the STED scans were carried out. Without the RESCue mode enabled (**c**, normal), strong bleaching inhibits the data acquisition. Imaging under RESCue conditions leads to a convincing fluorescence preservation of fluorescence (**b**, lTh). The RESCue parameters were set to: lTh of 6 photons, cT of 40 µs implemented with the FPGA board. After all STED scans were performed, a final confocal overview scan was recorded (**d**) to show the remaining fluorescence within the corresponding ROIs. All images in the second and third row were deconvolved using a *Richardson-Lucy* algorithm.

Fig. 4.7 shows the results of a two-colour RECSue-STED experiment. The RESCue parameters were chosen as 50 µs for the cycle time and 4 photons for the lower threshold. The dwell time was 400 µs, the image size 5 x 5 µm and the pixel size 25 nm. APP in primary mouse neurons was immunostained with Atto565 (Fig. 4.7b, d) and excited with 532 nm, the synaptic vesicle marker synaptophysin was labelled with Dy485XL (Fig. 4.7c) and excited with 470 nm. Fig. 4.7e and 4.7f are the corresponding linear deconvolved images, Fig. 4.7a depicts an overview, Fig. 4.7b is the confocal APP image for comparison. Dy485XL exhibits a large stokes shift. The emission spectra of both dyes are similar, so the same STED line can be used. To distinguish between the two dyes, the different absorption spectra are utilized. The distribution discerned in the STED mode is completely different (Fig 4.7g). Compared to Atto565, Dy485XL bleached faster and profited more from the RESCue mode. Since there is always a given probability to excite Dy485XL by the 532 nm line and Atto565 by the 470 nm line, RESCue reduces the photobleaching of not only the dye currently delivering fluorescence photons, but also of the second label. One can imagine that if there is a third dye, for example GFP, which is efficiently excited by 470 nm and discernable from Dy485XL by the fluorescence emission spectra, the effect of preserving this label while scanning the Dy485XL label is even bigger. The effect of reducing the bleaching is extraordinary if one dye gets excited by the STED line suitable for the other dye. In this case, the dye absorbs the strong signal suppression intensity in the standard STED mode, whereas in the RESCue-STED mode, if the dyes are not co-localized, the second label is only exposed during the significantly reduced cycle time.

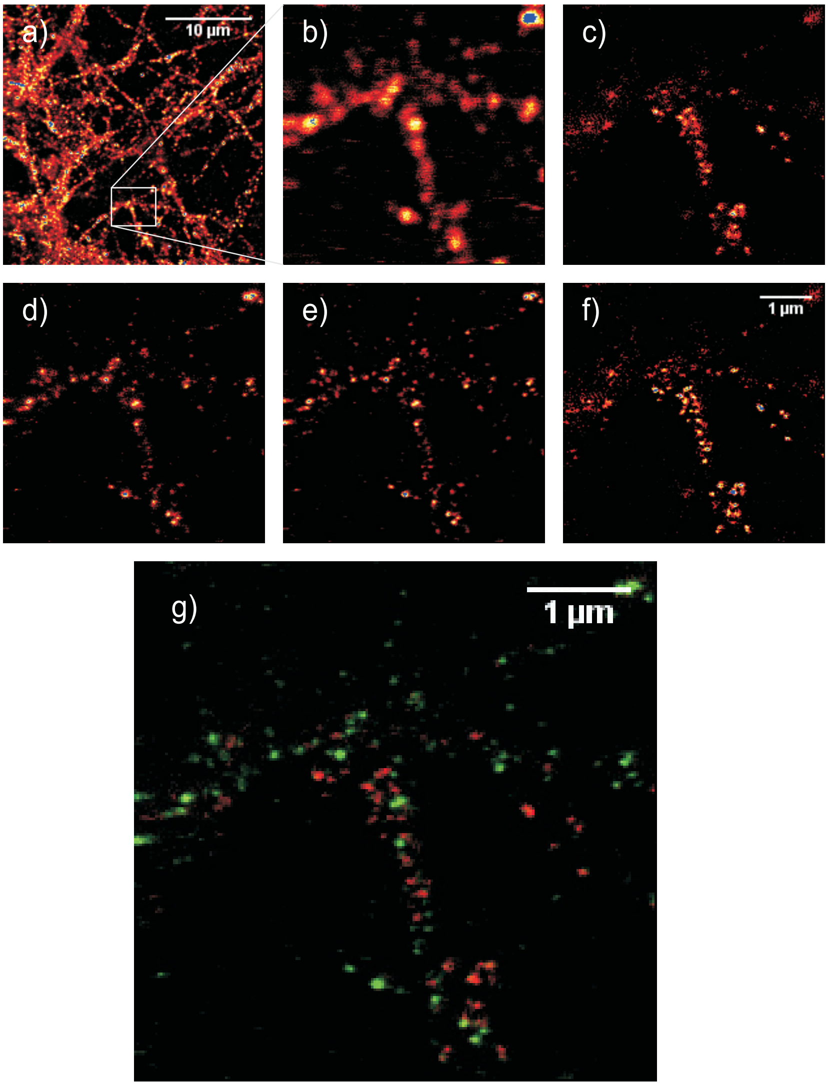

Fig. 4.7: Two-colour STED experiments benefit strongly from RESCue. In (**a**) an confocal overview of Atto565-immunostained APP is shown. (**b**) depicts a confocal image of the Atto565-APP distribution within the ROI (white box) investigated further in the RESCue-STED mode (**c**) and (**d**) implemented by the circuit board. Synaptophysin was also labelled by another dye (Dy485XL) (**c**) to co-localize APP (**d**) and synaptic vesicles. (**e**) and (**f**) are the linear deconvolved images of the corresponding STED images of APP and Synaptophysin. The overlay (**g**) demonstrates no significant co-localisation of APP (green) and Synaptophysin (red) which can not be concluded by the confocal image because of the insufficient resolution. To measure multicolour samples, more scans are necessary to gather all information. If dye A is affected by the wavelengths used for the dye B, a different distribution in combination with RESCue should significantly reduce photobleaching of dye A when measuring dye B if the dyes are sequentially read out. A background of 5% was subtracted in all images.

4.3.4 RESCue-STED of Atto565-labelled GFAP

To prove that also dense distributions of fluorescent spots exhibit a reasonable reduction of photobleaching with the aid of the lower threshold, the glial fibrillary protein (see appendix A.2.2 for preparation) (GFAP) immunostained with Atto565 was imaged. GFAP is an intermediary filament in the cytoplasm of glial cells. Here, the dye molecules are densely packed on a filament, as can be seen in the confocal image (Fig. 4.8a). All settings were identical to the settings used to gain the APP data (Fig. 4.6). In this case too, a positive influence on the bleaching behavior is apparent when applying RESCue, resulting in a 4-fold reduction of photobleaching.

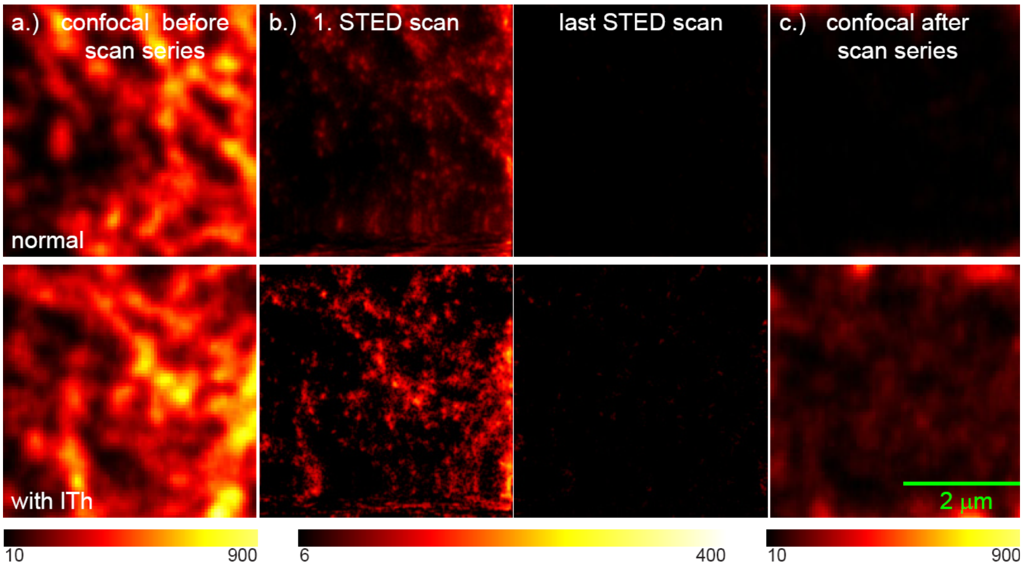

Fig. 4.8: The lower threshold leads to a bleaching reduction in Atto565 immunostained glial fibrillary proteins (GFAP) in glioblastoma cells (u373) by a factor of 4. Analogous to Fig. 4.5, the confocal image (**a**) represents the sample before the STED scans. Without the RESCue mode enabled, only one scan can be performed (**b**, normal). After the third scan, almost all the fluorescence was bleached. With a lower threshold of 6 photons and cycle time of 40 µs (FPGA implemented) the fluorescence of the densely labelled filaments can be preserved for significantly more scans (**b**, lTh). After a series of STED scans a confocal overview was recorded to demonstrate the affect of the RESCue mode in preserving the fluorescence (**c**).

The fluorescence of densely distributed dye molecules, as shown in Fig. 4.8, can be preserved even more by using an additional parameter. In all cases a certain SN is sufficient to obtain an interpretable image. For this purpose an upper threshold (uTh) can be specified as was already introduced in controlled light exposure microscopy (CLEM) measurements (Hoebe et al., 2006). In case the uTh is reached in a time shorter than the dwell time, the illumination can also be stopped or the scanner can move to the next volume immediately. This will conserve bright objects and not use up their complete fluorescence in one single read-out event thus further reducing the switching cycles in the diffraction neighborhood (Staudt et al., in preparation).

4.3.5 RESCue-STED of Atto647N-labelled lamina: enabling measurements in three dimensions

RESCue can not only be used to profit from a better bleaching behavior and thereby improve the image quality of a certain specimen compared to the normal STED mode. Some problems can be exclusively addressed by RESCue-STED. One example is shown in Fig 4.9 illustrating the RESCue-STED adoption to 3D measurements by imaging Atto647N-labelled lamina in 3D. The dwell time was 100 µs, cycle time was 30 µs, the lower threshold was 426 photons. The dye was excited with a 635 nm pulsed laser diode and for the STED pulses a Ti:Sapphire laser was employed. The Fig. 4.9 shows a 3D surface-rendered view of the nuclear lamina. On the left hand side the measurement in standard STED mode is presented. The 3D data stack was generated by sequential *xz* scans. After a few *xz*-sections the fluorescence was lost due to photobleaching. On the right hand side a measurement performed in the RESCue-STED mode taken with the same STED settings as in the previous measurement is shown. RESCue enables 3D data stacks, which could not be achieved otherwise. Especially in 3D applications, the fluorescence must be conserved in the close neighbourhood of the focus by blanking the lasers whenever possible.

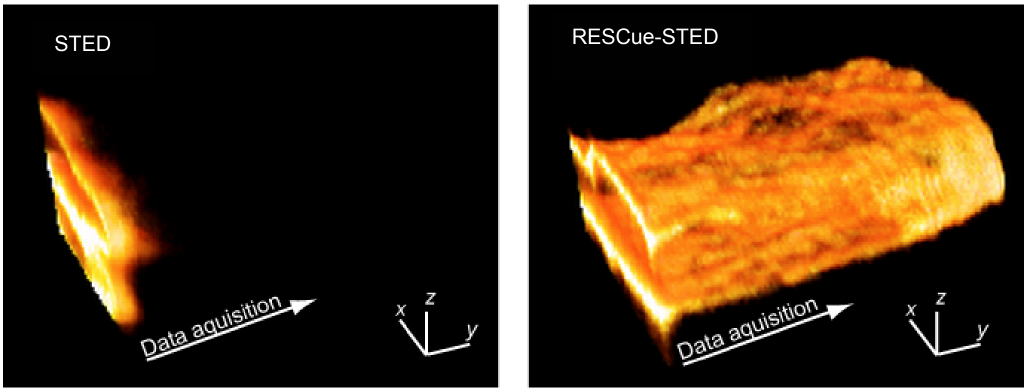

Fig. 4.9: RESCue makes it possible to measure A647N-immunostained nuclear lamina in neuroblastoma cells in 3D. The left image (STED) shows the attempt to image the lamina without RESCue enabled which fails because of pronounced bleaching. The image on the right side (RESCue-STED, implemented with the circuit board) demonstrates the possibility to record images with the aid of RESCue.

4.3.6 Coumarins in STED microscopy

All STED experiments carried out so far relied on dye molecules which are fluorescing above 550 nm. The spectral range from 400 to 550 nm has not been made accessible for STED microscopy yet. For multicolour experiments, it would be advantageous to expand the range of usable dyes to the blue-green spectral range. Furthermore, a STED beam with a shorter wavelength provides *per se* a smaller zero expecting a higher resolution. For these reasons, different coumarin derivatives were investigated. Coumarin derivatives are applied for a long time in dye lasers, therefore it is obvious to use them for STED microscopy since both applications rely on stimulated emission. For imaging, they have been the blue emitting dye used alongside fluorescein (green emission, around 520 nm) and rhodamine (orange emission, around 580 nm) derivatives in conventional multicolour applications. Each dye-class has some significant disadvantages. Coumarins have lower extinction coefficients compared to fluorescein and rhodamine derivatives. The number of survived excitation cycles before the photobleaching event is by a factor of 100 to 4000 smaller compared to rhodamine derivatives (Eggeling et al., 1998). As a rough rule of thumb one can conclude that the lower the wavelength for excitation and STED, the more must be done to prevent photobleaching. Another drawback of coumarins is associated with ultraviolet and blue excitation and signal suppression wavelengths in the blue to green range of the spectrum, namely phototoxicity. Therefore, the reduction of photobleaching and phototoxicity is a necessary premise to apply coumarins in STED microscopy.

Different coumarin derivatives were used for the following STED experiments, all of them are based on the structure shown in Fig. 4.10.

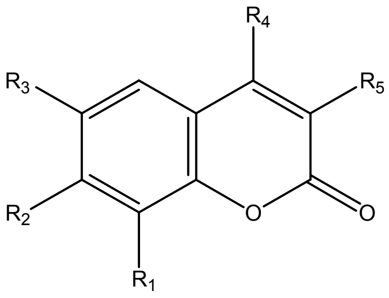

Fig. 4.10: Basic structure of the coumarin derivatives used for STED experiments.

The fluorescence of the coumarin derivatives C6H, C522, and Atto390 can be excited by a 405 nm diode and depleted by 514 nm in the cw as well as in the pulsed mode. The fluorescence depletion efficiency of the dyes dissolved in ethanol ranges from 83% to 91% in both modes. The dyes Atto425, Atto390 and Dy415 turned out to be most promising for STED experiments, because they are photostable enough and two-colour applications (Atto425 and Atto390) are predictable. The spectral characteristics of Atto425 are shown in Fig. 4.11. The fluorescence of the dye dissolved in *N,N*-dimethylformamide (DMF) can be excited by 440 nm (Fig 4.11, green line) and suppressed to 7% (Fig 4.11, red line) of the initial fluorescence intensity (Fig 4.11, black line) by the 514 nm Ar-Kr-laser line. By changing the solvent to water, the fluorescence is shifted towards longer wavelengths (from 475 nm to 485 nm, blue line). The efficiency to deplete the fluorescence follows the emission and can therefore be tuned to a certain extent by changing the solvent.

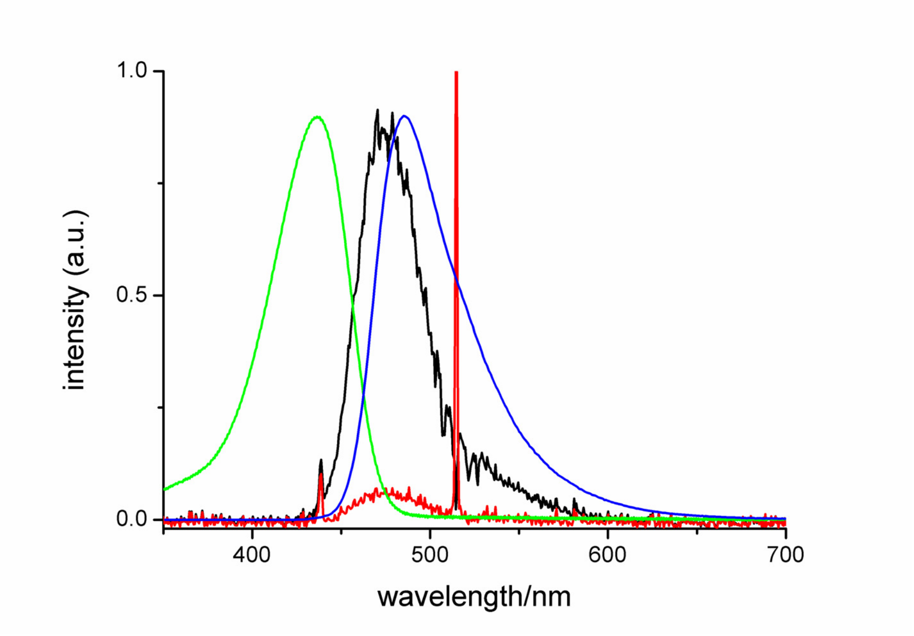

Fig. 4.11: Absorption (green line) and emission (black line) spectrum of the coumarin derivative Atto425 dissolved in DMF. Excitation was achieved by a pulsed 440 nm diode (spike in the black spectrum) and the fluorescence signal was depleted by a pulsed 514 nm Ar-Kr line (red spectrum, the spike marks the 514 nm line). The fluorescence can be depleted to 7%. The fluorescence spectrum in water is shifted by 10 nm to longer wavelengths (blue line) predicting a higher depletion efficiency.

Anti-fades suitable for coumarins in STED microscopy

To figure out strategies to prevent the pronounced photobleaching of coumarin derivatives exemplarily on Atto425, the dye was immobilized on amino-functionalized coverslips by reaction with Atto425-NHS ester. The covalently linked dye was embedded in different solutions of anti-fades for subsequent STED experiments. The STED-beam was not modified by a phase plate. Fig. 4.12 shows the results of the STED experiments on an Atto425 surface embedded in pure water (Fig. 4.12c, d), and embedded in water containing 20mM MEA. A field of 7 x 3 µm was scanned by the excitation beam (440 nm). The STED beam was switched on for the second half of the ROI (Fig. 4.12a, b). The fluorescence level was 15% higher in the case of the MEA containing embedding compared to the pure water embedding. (Fig 4.12a Exc. and b Exc.). In both cases, the fluorescence depletion efficiencies were around 90 % directly visualized in the Fig. 4.12a and c. After the STED experiment, the ROIs were scanned for a second time by the excitation beam only to determine the extent of photobleaching (Fig. 4.12 b, d).

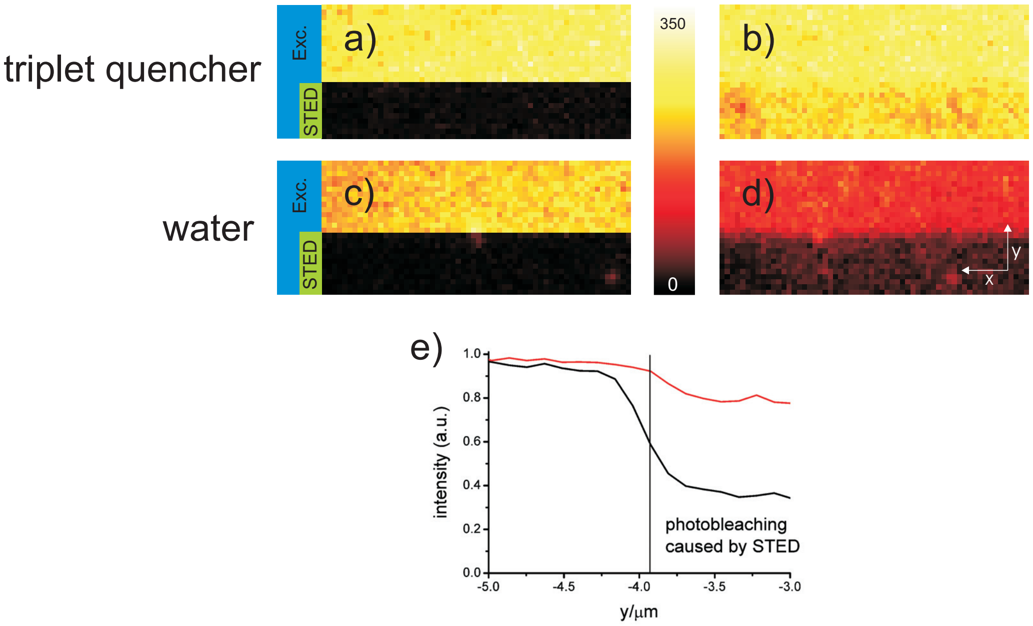

Fig. 4.12: The triplet quencher MEA reduces the photobleaching of the coumarin derivative Atto425 by a factor of four. The dye molecules immobilized on a glass surface were embedded in water (**c**) and (**d**) and in water containing 20mM MEA (**a**) and (**b**). A region of 3 x 7 µm on each of the two glass surfaces was scanned. The excitation (440 nm) was enabled for the whole region and the STED beam (514 nm, no phase plate installed) was switched on during the second half of the ROI. The fluorescence depletion efficiency can be seen by the decreased intensity ((**a**) and (**c**), marked with STED). After the first scans, second scans of the same ROIs were performed to determine the photobleaching relative to the first scans. It is obvious, that MEA preserves the fluorescence in the case of only the excitation, as well as in the STED case (**a**), (**b**). The dye molecules embedded in the MEA solution (**b**) exhibit a 15% higher fluorescence intensity and a four fold reduced photobleaching in the STED case due to faster triplet recovery compared to the dye molecules embedded in water (**d**). The graph (**e**) was derived by integrating the whole areas shown in (**b**) and (**d**). The red line corresponds to the fluorescence intensity of the dyes embedded in the MEA solution.

The embedding in the MEA solution led to a significant reduction of photobleaching in the STED case and in the pure excitation case compared to the water embedding (Fig 4.12b, d STED). Under comparable conditions, MEA reduces the photobleaching by a factor of four from 60% to 15% (Fig. 4.12e). If molecular oxygen is removed by an enzyme system based on glucoseoxidase and catalase (Harada et al., 1990) in addition, photobleaching can be further reduced by a factor of two resulting in an overall reduction of photobleaching by a factor of eight in water based embeddings. *p*-Phenylenediamine (PPD) is also among highly effective additives for the reduction of photobleaching, but it quenches also the fluorescence by a factor of three.

MEA is a well-known triplet quencher and very effective in reducing photobleaching. This fact underscores, that photobleaching occurs mainly from molecules in the triplet state. MEA rapidly recovers the singlet groundstate due to collisions with the fluorescent dyes preventing further bleaching pathways. After removal of oxygen, the dyes are even more prone to photobleaching, because oxygen also acts as an effective triplet quencher. Removing oxygen and recovering triplet quencher properties by a non-oxidizing triplet quencher is an effective strategy to prevent photobleaching of coumarins in STED related experiments. The signal intensity can be increased by 15% because the triplet state gets faster relaxed and the molecules are therefore more often available for excitation events.

The embedding of coumarin derivatives in DABCO containing Mowiol is also advantageous to avoid photobleaching. Fig. 4.13 shows the microtubuli network in glioblastoma cells immunostained with Atto390 and embedded in Mowiol containing DABCO (see appendix A.2.1 for preparation). Features in the range of 70 to 80 nm can be discerned.

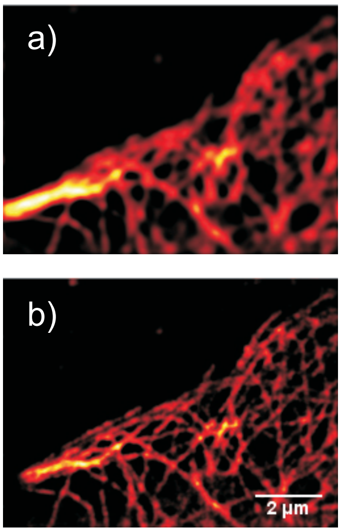

Fig. 4.13: Confocal (**a**) and STED measurement (**b**) of microtubuli in glioblastoma cells immunostained with Atto390 and embedded in Mowiol containing the singlet oxygen quencher DABCO. Features in the range of 70 to 80 nm can be discerned with the aid of the coumarin derivative Atto390. The resolution is limited by photobleaching.

RESCue-STED of coumarins: exploitation of the blue spectral range

The application of anti-fades for coumarin based STED microscopy is mandatory, but the resolution is still clearly limited by photobleaching. For this reason, additional strategies to tackle photobleaching have to be pursued. Recently, T-REX was applied on Atto425-filled silica beads embedded in Mowiol containing DABCO. In this approach, the STED measurements were performed with a passively Q-switched 532 nm microchip laser with a repetition rate of 60 kHz to relax triplet states (Rankin et al., 2008). However, the low repetition rate calls for long pixel dwell times (typically in the range of 15 to 30 ms). The RESCue mode in contrast provides a more general method to further reduce photobleaching without sacrificing data acquisition speed.

A comparison of self-made Atto425-filled silica beads (25 nm diameter) on a poly-L-lysine (PLL) coated coverslip (see appendix A.2.2 for more information about the bead preparation) recorded in the RESCue-STED mode (RESCue, first half of the images) and in the conventional STED mode (normal, second half of the images) is shown in Fig. 4.14. After a confocal scan (Fig. 4.14a), two STED scans were performed (Fig. 4.14b, c). In the RESCue mode, the background is significantly suppressed by a factor of 6 because of the lower threshold. The RESCue parameters were chosen to one photon for the lower threshold and 36 µs for the cycle time. The dwell time was set to 300 µs. During the first scan in the conventional STED mode, the dyes were already bleached to a high extent (Fig. 4.14b) compared to the recording under RESCue-STED conditions. The fluorescence spots in the white circles are comparable regarding the fluorescence intensity. After the second STED scan without RESCue enabled, the fluorescent bead is completely photobleached. However, the RESCue-STED mode preserves the fluorescence for repetitive scans. Each fluorescent bead can be localized even in the second scan (Fig 4.14c).

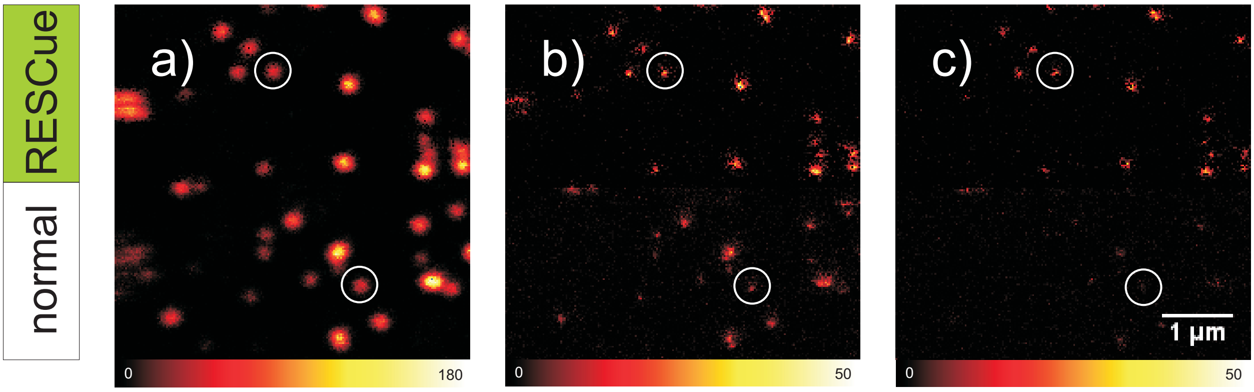

Fig. 4.14: The RESCue-STED mode in combination with a chemical anti-fade (DABCO) enables high resolution images of Atto425-filled silica beads with a diameter of 25 nm. In (**a**), a confocal image of the 30 nm silica beads is shown. During the first part of the following STED recordings (**b**) and (**c**), the RESCue mode was enabled (implemented by the circuit board). The white circles mark two beads of approximately the same fluorescence intensity. In the conventional STED mode, the photobleaching is distinct, and decreases the intensity and the resolution significantly. In the second STED scan (**c**), almost no fluorescence is left in the conventional mode, whereas the fluorescence is well preserved in the RESCue mode. Still, every bead present in the ROI can be localized.

If the fluorescent molecules within the silica beads are bleaching even before they reach the zero of the STED beam, the achievable resolution decreases, as can be seen in Fig. 4.14b. Fig. 4.14 clearly demonstrates the suitability of coumarins in STED microscopy due to the presence of singlet oxygen scavengers (DABCO) or triplet quenchers (MEA) in combination with RESCue.

The coumarin derivatives, especially Atto425, Atto390 and Dy415 can now be considered as alternatives in multicolour STED applications owing to chemical anti-fades and the RESCue approach. A descent resolution enhancement can be predicted (Fig. 4.15). It is even possible, to discriminate between Atto425 and Atto390 by excitation multiplexing (440 nm and 405 nm) for multicolour experiments.

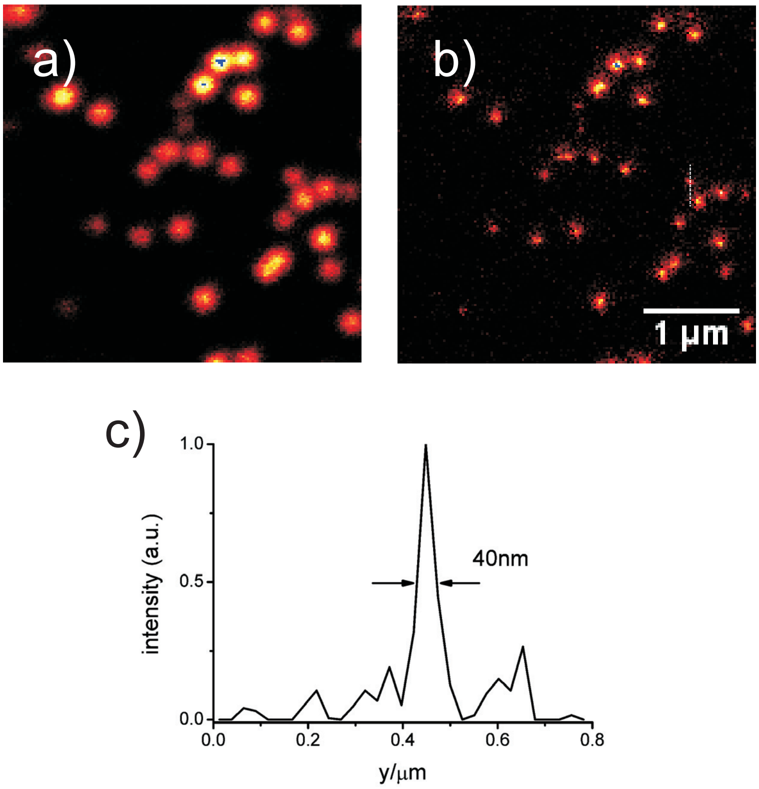

Fig. 4.15: Due to the consequent exploiting of anti-bleaching strategies, the coumarin derivatives can be considered as alternatives expanding the range of useful dyes for STED experiments to the blue-green region. The comparison of a confocal (**a**) and a STED image (**b**) of 25 nm A425-labelled silica beads is shown. The intensity profile (**c**) along the doted line in c) indicates a FWHM of 40 nm.

The RESCue-STED modality takes advantage of the high resolution information itself to locally adapt the sample exposure. This strategy results in a reduction of photobleaching even compared to the standard confocal imaging mode, if the pixelsizes are comparable. Higher resolution is no longer necessarily connected to higher photobleaching. The RESCue-STED mode enables experiments which are connected to high light doses such as 3D measurements, multicolour imaging, and time series. Furthermore, the so far unexploited dye class of coumarin derivatives in the blue to green emission range can now be considered as an alternative in STED experiments due to the RESCue-STED modality

Chapter 5

Direct light-driven modulation of luminescence from Mn-doped ZnSe quantum dots: a new contrast

5.1 Introduction

The fluorescence label and its susceptibility for manipulation is one of the most important parts in fluorescence microscopy. The optimization of the labels regarding photostability, brightness, robustness of switchability and other photophysical properties are critical in high resolution imaging. Quantum dots as fluorescent entities are known for their superior photostability. They are zero-dimensional systems in which the electronic structure can be precisely tuned by varying the size of the nanocrystal (Michalet et al., 2001). These attributes, along with recent advances in synthetic chemistry, have placed QDs at the forefront of fluorescence microscopy with the advantages of enhanced photostability, high quantum yield, wavelength tunability, and macromolecular size (Sukhanova et al., 2004; Reiss and Bleuse, 2002; Michalet et al., 2005). These benefits are particularly useful for single-molecule detection and tracking as well as time-domain imaging, and have even unlocked new concepts such as multimodal imaging and optical bar-coding (Dahan et al., 2003; Dahan et al., 2001; Santra et al., 2005; Huh et al. 2005; Han et al., 2001). The range of applications extends well beyond the realm of imaging, as QDs also play a major role in developing novel photonic devices including lasers, light emitting diodes, and displays (Klimov et al., 2007; Mattoussi et al., 1998; Song and Lee, 2007). Despite significant advancements in nanocrystal research, the continued failure to directly modulate fluorescence from QDs has precluded their implementation in several areas. In particular, emerging far-field diffraction-unlimited microscopy techniques (Hell, 2007) uniquely benefit from the capability to reversibly modulate/switch fluorescent ensembles from a bright “on” state to a dark “off” state. Moreover, this activation must occur as a response to optical stimuli, i.e. laser radiation, which does not contain spectral components within the excitation kernel of the fluorescent markers. Realizing the desperate need for optical control over QD fluorescence, indirect schemes have been conceived using QD hybrid structures that incorporate a photochromic activator/quencher (Zhu et al., 2005; Jares-Erijman et al., 2005; Medintz et al., 2004). Although the concept has been clearly established, QD hybrid structures suffer from inherent drawbacks such as inadequate photostability, limited fluorescence quenching, necessity of energetic UV photons for activation, and sensitivity to local environment/solvent. The direct manipulation of the fluorescence from conventional QDs via STED would be a straight consequence of the high photostability and superior brightness. However, the possibility to excite the QDs over a wide range even within the fluorescence band of the QDs prevented the application of QDs in STED microscopy so far (Fig. 5.1), because the intense signal suppression beam would efficiently excite the QDs.

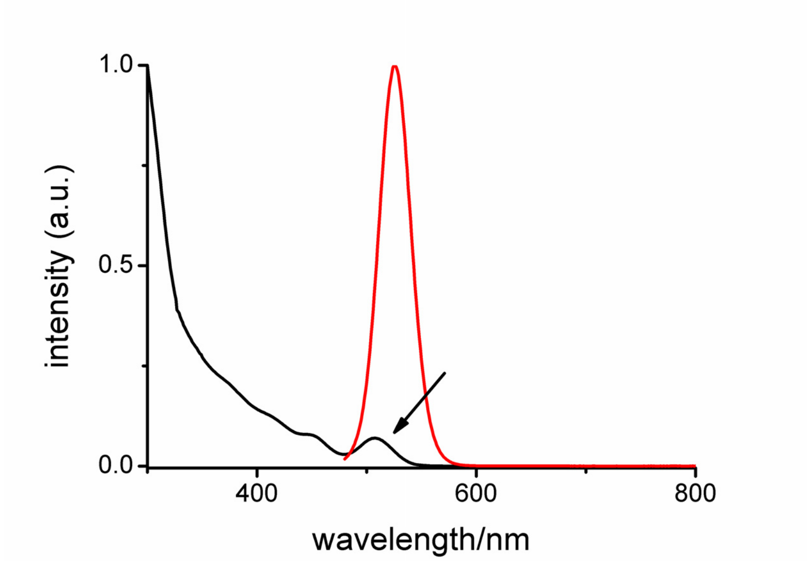

Fig. 5.1: Excitation and fluorescence spectrum of QDs (Qdot 525 streptavidin conjugated, Invitrogen). The excitation spectrum spans across a wide range and hinders their application in STED microscopy due to excitation by the intense STED beam.

The manganese-doped ZnSe quantum dots exhibit a fluorescence spectrum which is shifted towards higher wavelengths and would therefore be suitable for STED experiments (Fig 5.3). During investigations of the modulation behaviour depending on the modulation wavelength it was found, that it is possible to suppress the fluorescence by a wavelength located beyond the fluorescence spectrum. Therefore, since STED can not be responsible for the modulation, a new mechanism must be considered.

In the following, a new realization of a “dark” state by excited-state absorption (ESA) is introduced working with low signal suppression intensities in the case of zero based high resolution methods applying manganese-doped ZnSe quantum dots.

5.2 Emission switching in manganese doped ZnSe quantum dots

A schematic diagram of the electronic transitions involved in light-modulated fluorescence from Mn-QDs is shown in Fig. 5.2.

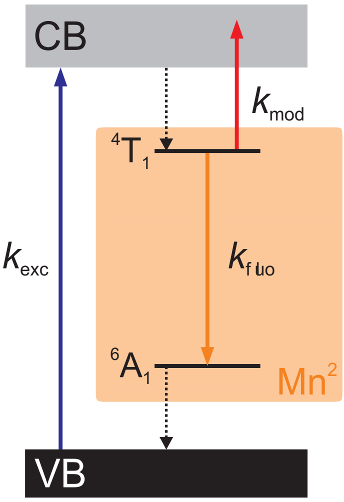

Fig. 5.2: Schematic diagram of the electronic transitions involved in modulating fluorescence from Mn-QDs. Initially electrons are pumped (k_{exc}) from the valence band (VB) to the conduction band (CB) of the ZnSe host, and are subsequently transferred to the $^4T_1$ level of the Mn^{2+} dopant. Here, the electrons can relax radiatively (k_{fluo}) to the $^6A_1$ level; however, they can also be pumped (k_{mod}) to higher levels via excited-state absorption (ESA) from $^4T_1$.

Initially, electrons are photoexcited from the valence band to the conduction band of the ZnSe semiconductor host. Within a short time in the picosecond timescale (Hefetz et al., 1986; Bhargava et al., 1994; Kuroda et al., 1997), the excited electrons are transferred to the $^4T_1$ upper florescent state of the Mn^{2+} ion and decay radiatively to the $^6A_1$ state within a measured fluorescence lifetime of $\tau_{fluo} \sim 90$ μs (see below). Generally speaking, direct fluorescence modulation requires active control over a process that competes with spontaneous emission. For doped semiconductors and glasses, excited-state absorption (ESA) can occur from the upper fluorescent level of the impurity ion to higher lying states either within the dopant or the conduction band of the host material. Depending on the specific density of states above $^4T_1$, red-shifted light (with respect to excitation) can be used to invoke the ESA mechanism to selectively pump electrons out of $^4T_1$ and inhibit spontaneous fluorescence emission, while avoiding further excitation from the ZnSe host.

Room temperature absorption and photoluminescent spectra of the Mn-QDs are shown in Fig. 5.3. Absorption due to the ZnSe host is clearly observed, with the first exciton peak occurring at a wavelength of ~400 nm. Fluorescent emission is centred at a wavelength of 580 nm with a full-width at half-maximum of ~50 nm and is a hallmark of the $^4T_1 \rightarrow {}^6A_1$ transition of the Mn^{2+} dopant (Pradhan et al., 2007).

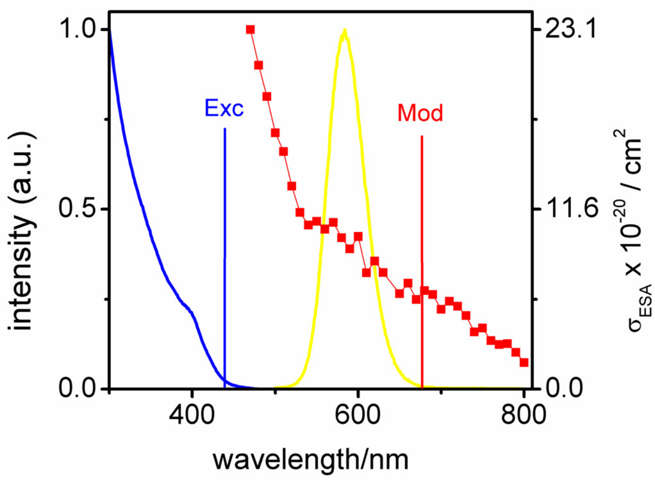

Fig 5.3: Absorption (blue line), emission (yellow line) and ESA spectra (red line and squares, right vertical scale) of the Mn-QDs. The spectral locations of the excitation and modulation wavelengths are also indicated with a blue and a red vertical line.

Measurement of the ESA spectrum of the Mn-doped quantum dots (NN-Labs, Fayetteville, AR) was carried using a two beam “pump-probe” arrangement (Rittweger et al., 2007).

Excitation radiation at a wavelength of 405 nm was provided by a laser diode (PicoQuant, Berlin, Germany) while associated ESA losses were determined from a co-propagating white-light continuum probe (Fianium, Southampton, United Kingdom). Lock-in discrimination (Signal Recovery, Wokingham, United Kingdom) was used to detect small losses in the white-light probe beam that resulted directly from the chopped excitation beam. The spectral variation of the ESA was determined by placing 10 nm band-pass filters (AHF Analysentechnik, Tübingen, Germany) before the sample to select a small portion of the continuum. In this case, the sample consisted of a concentrated solution of the Mn-doped quantum dots (20 µM in toluene) to ensure adequate signal level. Losses in the white-light continuum probe are converted to units of ESA cross-section, σ_{ESA}, using the following formula:

$$P_{trans} = P_{in}\, exp(-\sigma_{ESA} NL), \tag{5.1}$$

where P_{trans} is the power transmitted through the sample, P_{in} is the input power, N is the concentration of excited quantum dots, and L is the effective path length. This formula is rearranged to solve for σ_{ESA}:

$$\sigma_{ESA} = \frac{-ln\left(\frac{P_{trans}}{P_{in}}\right)}{NL} \tag{5.2}$$

The difference between input power and transmitted power can be expressed as an infinitesimal quantity, $P_{trans} = P_{in} - \Delta P$, which allows Eq 5.2 to be simplified according to a Taylor series expansion of the natural logarithm function:

$$\sigma_{ESA} = \frac{\Delta P}{P_{in} NL} \tag{5.3}$$

The density of excited quantum dots, N, within the focal volume of the excitation beam is estimated from the intensity of the excitation radiation, the absorption cross-section of the quantum dots, and their fluorescence lifetime, while the interaction length, L, is taken to be the *Rayleigh* range of the excitation beam.

The spectral dependence of the fluorescence depletion was also measured using the arrangement described above. In this case, however, the white-light probe beam was chopped and changes in the fluorescent level (collected at 90° from excitation) were measured by lock-in detection. Again, interchangeable filters (20 nm band-pass, AHF Analysentechnik) were used to gauge the spectral dependence. The fluorescence signal was additionally filtered before detection (60 nm band-pass centered at 575 nm, AHF Analysentechnik) to eliminate large amounts of scattered light, which also limited the spectral measurement range to 630-800 nm. Below ~545 nm, a large fluorescence signal overwhelmed the ESA signal, which is believed to stem from transient population of the $^6A_1$ level. The results of this are shown in Fig. 5.4 along with the results of the ESA measurement and indicate that fluorescence depletion follows the ESA. This provides strong evidence that the fluorescence depletion results from ESA transitions originating from the $^4T_1$ upper fluorescent state.

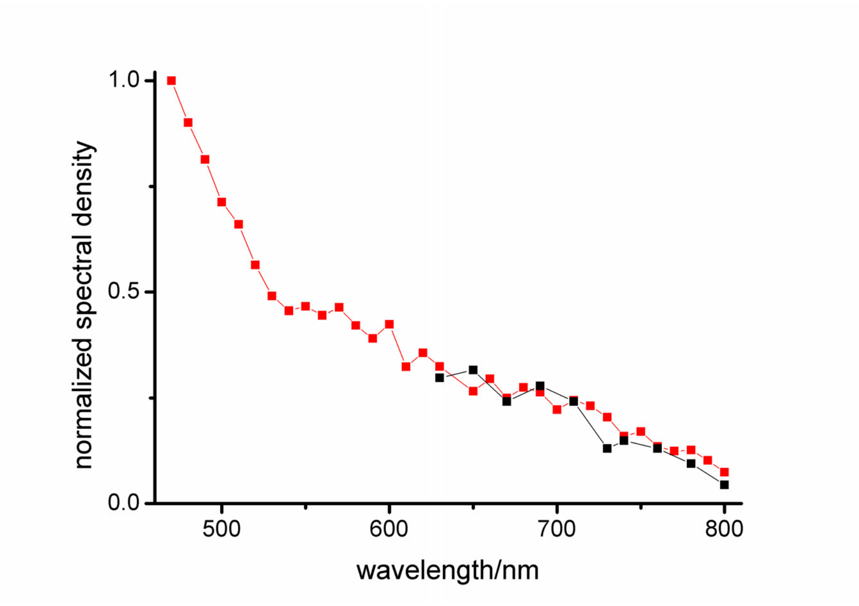

Fig. 5.4: Excited-state absorption (colored in red) and fluorescence quenching (colored in black) measurements of the luminescence from Mn-QDs.

Results of this measurement are shown also in Fig. 5.3, where it is observed that the ESA spectrum spans a large portion of the visible window. Similar results have also been obtained for bulk Mn-doped ZnSe (Dreyhsig et al., 1990) and Co-doped ZnSe. (Ehlert et al. 1994). Other rare-earth doped glasses (Lawson et al., 1993). also show broadband impurity-host transitions that exhibit a large dependence on the particular host material. In any case, an intensity-dependent loss channel that competes directly with the fluorescent emission can be introduced to efficiently modulate the luminescence originating from the ${}^4T_1 \rightarrow {}^6A_1$ transition. Experimentally, the spectral criteria for fluorescence imaging of the Mn-QDs are fulfilled using collinear laser sources at $\lambda_{exc} = 440$ nm and $\lambda_{mod} = 676$ nm for excitation and modulation, respectively. Radiation from the two sources is coupled into a scanning confocal microscope, and their corresponding intensities, I_{exc} and I_{mod}, are controlled using acousto-optic tunable filters. The extended lifetime (~90 µs) of the Mn^{2+} ${}^4T_1 \rightarrow {}^6A_1$ transition limits the number of excitation-emission sequences a single Mn-QD can perform within a given time frame. Thus, the fluorescent photon emission rate is lifetime-limited, challenging optical imaging of single isolated Mn-QDs. As a favourable alternative, multi-QD ensembles were prepared on a glass coverslip to reach adequate fluorescence intensity levels, I_{fluo} (for the preparation of the QD ensembles see appendix A.3.1). Atomic force microscopy of the Mn-QD ensembles indicate a large distribution of sizes ranging from 20 to 300 nm.

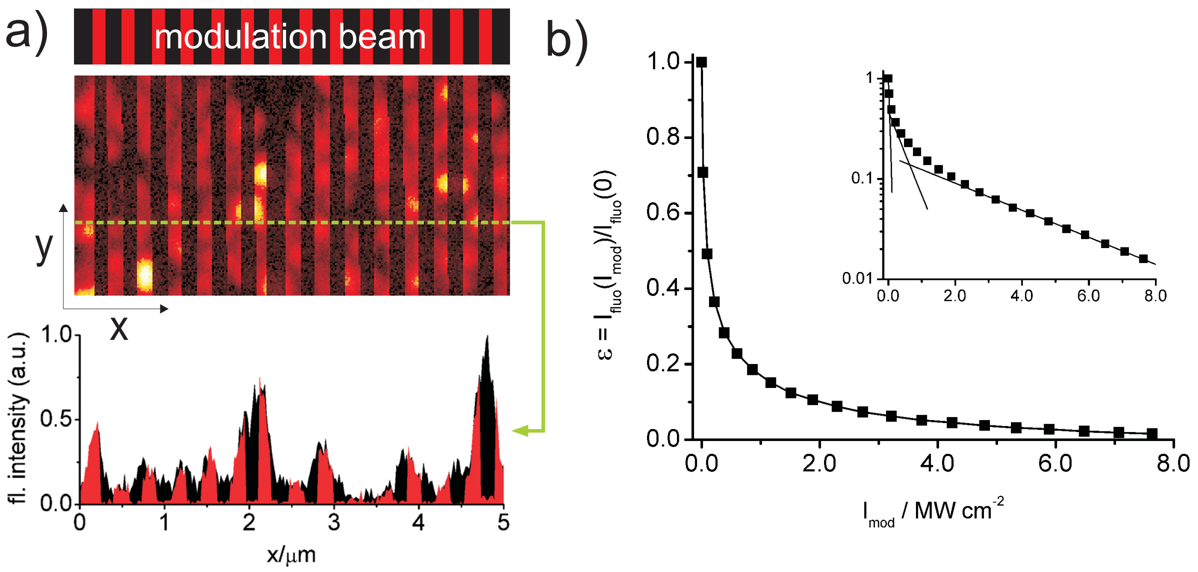

Fig. 5.5: (**a**) Confocal images of Mn-QD ensembles. Dark lines along the y-direction demonstrate the capability to actively and reversibly control fluorescence emitted from solid-state nanocrystals. Intensities of $I_{exc} = 50$ W cm^{-2} and $I_{mod} = 9$ MW cm^{-2} are utilized. A line section through the confocal image shows the fluorescence response and the high efficiency of modulation (red) overlaid with a similar line cut (black) through the corresponding image having $I_{mod} = 0$ (not shown). (**b**) Depletion curve indicating the normalized residual fluorescence, ε as a function of modulation intensity, I_{mod}. At $I_{mod} = 1.9$ M cm^{-2}, the fluorescence level is reduced to 10% of its original value. Logarithmic representation (inset) indicates a multi-exponential fluorescence depletion process. A triple exponential has been fit to the data and has characteristic decay constants of 0.043, 0.52, and 3.22 MW cm^{-2}, each of which have been illustrated by solid lines.

Confocal images of the ensembles are shown in Fig. 5.5a for $I_{exc} = 50$ W cm^{-2} and $I_{mod} = 9$ MW cm^{-2}. Here, I_{mod} was toggled with every 10th scan step along the x-axis, resulting in dark lines along the vertical direction where the fluorescence was selectively inhibited. This emphasizes the degree of optical control over the QD luminescence as well as its reversible nature. Measurement of the degree of fluorescence inhibition was carried out through acquisition of several of confocal images of Mn-QDs for various values of I_{mod}. As I_{mod} is incremented, interleaved confocal images with $I_{mod} = 0$ were also acquired to gauge bleaching effects. Results of this experiment are illustrated in Fig. 5.5b in terms of the residual fluorescence $\varepsilon = I_{fluo}(I_{mod})/I_{fluo}(0)$ as a function of I_{mod}. The effectiveness of the fluorescence inhibition process is clear as $\varepsilon < 10\%$ can be achieved for $I_{mod} = 1.9$ MW cm^{-2}. Over the course of the measurement, the fraction of bleached Mn-QDs was <17%. The inset of Fig. 5.5b contains a logarithmic plot of the fluorescence depletion and reveals the existence of multiple depletion channels, which is consistent with the large density of state above $^4T_1$ provided by the ZnSe conduction band as well as the upper manifold of the Mn^{2+} impurity (Clausen et al., 1988; Petermann et al., 1989).

Depending on the non-radiative decay across the ZnSe bandgap, it is possible that electrons which are momentarily shelved above $^4T_1$ by the modulation radiation are allowed to cycle between the conduction band of the host and the $^4T_1$ fluorescent state of the Mn^{2+} dopant. The degree of cycling can be readily ascertained by comparing the ESA cross-section, σ_{ESA}, determined directly from transient absorption measurements (Fig. 5.3) with the net ESA cross-section calculated via the fluorescence depletion curve (Fig. 5.5b). The net cross-section for ESA, ζ_{ESA}, for raising electrons from $^4T_1$ to the conduction band of the ZnSe host can be determined from the competition between the fluorescence decay rate, k_{fluo}, and ESA-induced pump rate, k_{mod}. Given $k_{mod} = \zeta_{ESA} I_{mod}$ and $k_{fluo} = 1/\tau_{fluo}$, ζ_{ESA} can be calculated from the fact that at $\varepsilon = 50\%$ the condition $k_{mod} = k_{fluo}$ is satisfied. Thus, a value of $\zeta_{ESA} = 2.1\times10^{-20}$ cm^2 is estimated and compares well with the value of $\sigma_{ESA} = 6.1\times10^{-20}$ cm^2 (at 676 nm) shown in Fig. 5.3 and those determined previously for other Mn^{2+} ion-host systems (Clausen et al., 1988). The fact that ζ_{ESA} and σ_{ESA} have the same order of magnitude indicates that a significant amount of electronic cycling does not occur. Furthermore, no up-converted emission from the terminal states of the ESA transition could be detected in the spectral region between 420-1100 nm. Based on this evidence, it is concluded that non-radiative transitions dominate electron relaxation to the valence band during fluorescence depletion.

To ascertain the modulation photostability of Mn-QDs, the excitation and modulation beams are focused on an isolated ensemble, without scanning, and the modulation beam is interrupted at frequency of ~25 Hz. The resultant time-domain fluorescence signal is shown in Fig. 5.6, which provides clear evidence of the robustness of the ESA-mediated fluorescence inhibition process.

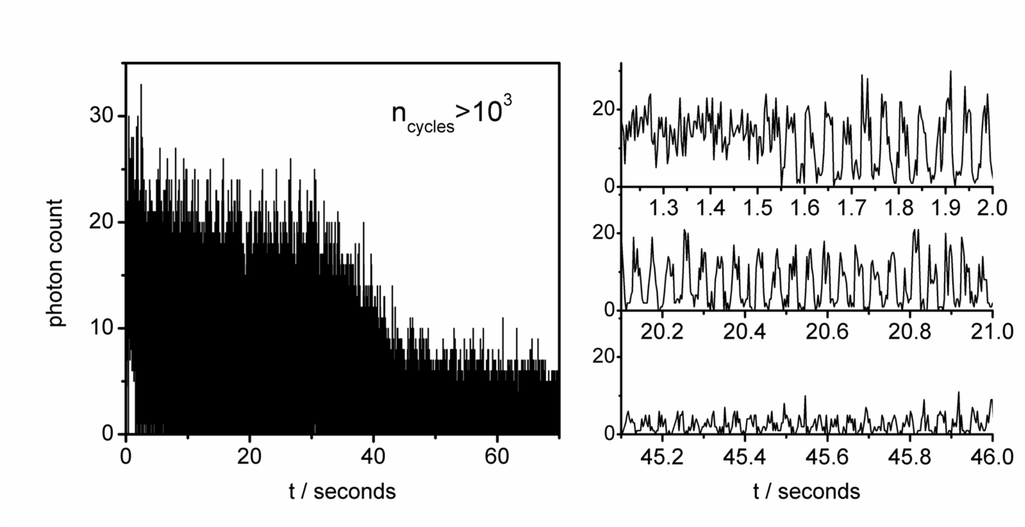

Fig. 5.6: Temporal fluorescent response from an Mn-QD ensemble under conditions of steady-state excitation at 100 W cm^{-2} and transient depletion at $I_{\mathrm{mod}} = 1.9$ MW cm^{-2}, in which I_{mod} is interrupted at a frequency of 25 Hz. Fluorescent modulation persists for nearly 40 seconds (~10^3 cycles) before the cluster photobleaches significantly. Several smaller panels illustrate the digital-like switching over timescales comparable to the modulation period.

Continuous excitation and depletion of the fluorescence persists for nearly 40 seconds before the quantum efficiency degrades substantially as a result of photobleaching. Within this measurement time frame, the single Mn-QD cluster has undergone on average 10^3 fluorescence modulation cycles.

5.3 Application of manganese doped ZnSe quantum dots in RESOLFT experiments

Efficient switching and stable on-off modulation are highly desirable attributes for advanced microscopy techniques. A primary example for which the Mn-QDs are ideally suited is RESOLFT imaging, which relies on reversibly photoswitchable luminescent compounds to achieve optical resolutions below the diffraction limit (Westphal et al., 2005). This is realized in a two-beam scanning confocal arrangement: one laser source is used to excite the photomarkers, while another spatially overlapped beam featuring an intensity null selectively inhibits fluorescence everywhere except regions near the null. Such a zero region is engineered through the introduction of a suitable phase-mask in the back focal plane of the objective (Keller et al., 2007). In this particular case, the resulting intensity distribution features a zero line in the focal plane, where the fluorescence is effectively “squeezed” along one axis that is perpendicular to the zero line.

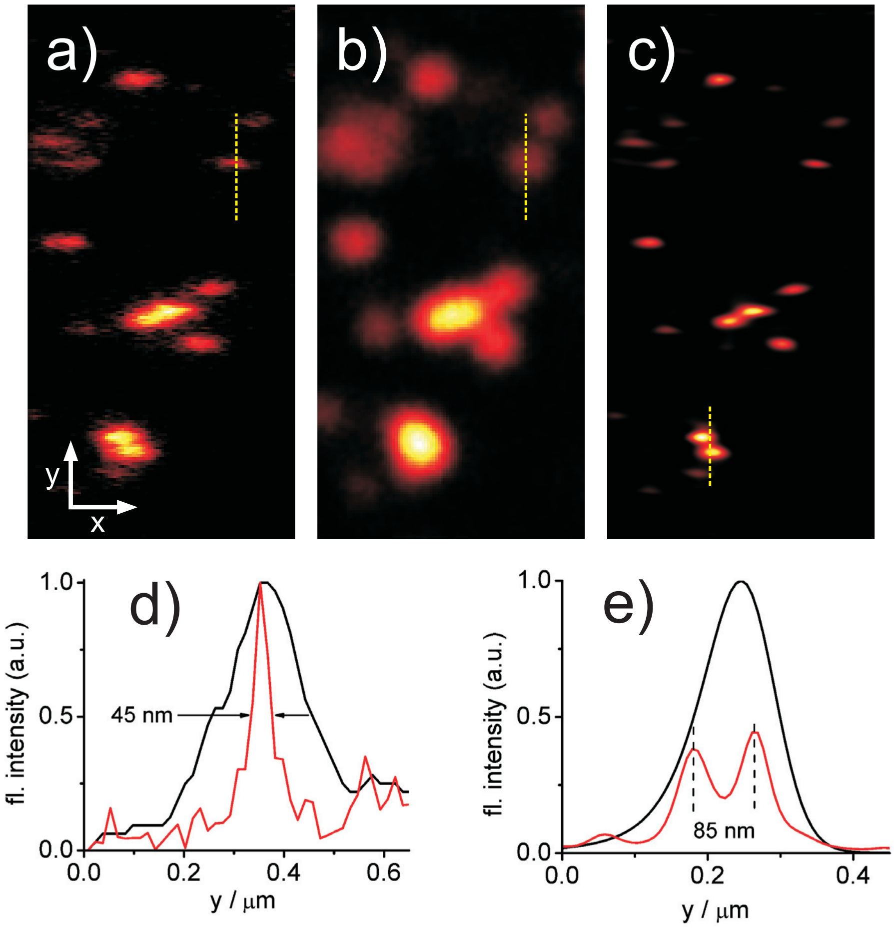

Fig. 5.7: Image acquired using the RESOLFT technique is shown in (**a**), which has a clear improvement in resolution along the *y*-direction in comparison to the purely confocal counterpart shown in (**b**). *Richardson-Lucy* deconvolution is applied to (a) and the result is shown (**c**). For comparison, a one-dimensional line section (indicated by a yellow dashed line) through a representative RESOLFT PSF (**a**) and its diffraction-limited counterpart (**b**) are plotted separately in panel d). The enhanced resolution is obvious as the 200 nm diffraction-limited PSF is effectively reduced to 45 nm. A similar section from (**c**) and its corresponding deconvoluted confocal counterpart (not shown) are illustrated in (**e**), revealing that structures separated by 85 nm can be distinguished using RESOLFT, which otherwise appear as a single peak in the confocal reference.

A reference confocal image of clusters of Mn-QDs is shown in Fig. 5.7b. Several isolated clusters are present and exhibit diffraction limited full-width at half-maxima of 200 nm. Larger features are also present, indicated by their relative brightness, though no information can be obtained regarding the sub-structure. RESOLFT images of the same region are shown in Fig 5.7a. Whereas single isolated clusters appear as nearly spherically symmetric intensity distributions in the confocal image, the corresponding PSF in the RESOLFT image have been substantially reduced along the *y*-axis by the spatially structured modulation beam.

A cross-section through a representative PSF is shown in Fig. 5.7d, which has a full-width at half-maximum of 45 nm; a factor of 4.4 improvement over the corresponding confocal PSF and nearly a factor of 10 smaller than λ_{exc}. The size of the PSF can be compared to the theoretical resolution as determined from (Hell, 2007),

$$\Delta r \approx \frac{\lambda}{2n\sin(\alpha)\sqrt{1+I_{\max}/I_s}} \tag{5.4}$$

where n is the index, α is the aperture angle of the objective, and λ and I_{max} are the wavelength and maximum intensity of the modulation beam, respectively. Here I_s is defined to be the depletion intensity required to reduce the fluorescence to one half of original value, which is determined from Figure 5.5b to $I_s = 0.1$ MW cm^{-2}. Given a local intensity of $I_{max} = 2.5$ MW cm^{-2}, in addition to $n = 1.5$ and $\alpha = 60^\circ$, $\Delta r = 51$ nm is calculated and compares well with the measured value of 45 nm. Non-linear deconvolution of the RESOLFT image results in the data shown in Fig. 5.7c, where clear sub-diffraction structure becomes apparent. Resolving such features was only possible after significantly expanding the microscope's optical transfer function via the optical modulation. Clear evidence of this is shown also in Fig. 5.7e. Two clusters separated by 85 nm can be clearly distinguished in the RESOLFT image, but appear as a single peak within the corresponding confocal scan.

For the resolution enhancement in two dimensions a vortex phase plate was applied instead of the two optical flats (described in chapter 3). The vortex phase plate generates a doughnut-shaped point spread function in the focus. A confocal image of the Mn-QD clusters is shown in Fig. 5.8a featuring a high size dispersion and some diffraction limited spots. The corresponding RESOLFT image of the same region (Fig. 5.8b) clearly discerns accumulations of the clusters. A linear deconvolution (Fig. 5.8c, d) enhances the image quality further.

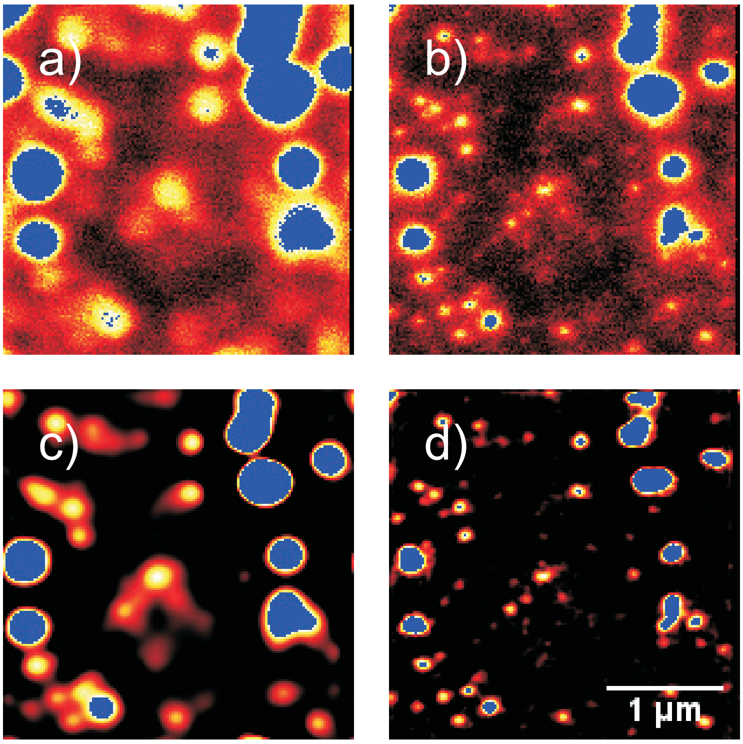

Fig. 5.8: The RESOLFT technique applied to Mn-QD clusters clearly proves the practicability of quantum dots and the ESA mechanism for high resolution imaging. In the upper row (**a**) and (**b**) the raw data is shown after a back ground subtraction of 10%. The RESOLFT image (**b**) suggests a resolution of 50 to 60 nm compared to the confocal image (**a**). The lower row (**c**) and (**d**) shows the linear deconvoluted counterparts.

For biological and medical applications these quantum dots can easily be coupled to antibodies, streptavidin or other relevant molecules taking advantage of the high affinity of the quantum dots to mercapto groups.

The introduction of standard quantum dots, which are not for example doped with manganese atoms in high resolution microscopy was hindered for a long time by their broad excitability. The laser beam for signal suppression excites also the labels prohibiting the application in STED experiments. The realization and maintenance of the "off" state has to be done far red relative to the excitation of the quantum dots. The implementation of a new mechanism to suppress the fluorescence (ESA) and the manganese doped quantum dots with additional electronic states lead to applications in RESOLFT experiments. The signal suppression via ESA can be performed far red relative to the excitability and therefore preventing excitation with the signal suppression beam. Another important consequence of the spectral separation between the signal suppression wavelength and the emission spectrum lies in filtering issues.

A larger fluorescence band can be collected leading to a sufficient SN at lower light doses reducing photobleaching.

The $^4T_1 \rightarrow ^6A_1$ transition is multiplicity forbidden and therefore the lifetime of the upper electronic state is long (90 µs) and the absorption of an additional photon probable. Because of the long lifetime of the upper state of the fluorescence system ($^4T_1 \rightarrow ^6A_1$) the intensities for signal suppression are low. Compared to STED microscopy, the intensities are 10 to 100 times lower. A lower photodamage can therefore be predicted. Another advantage is the possibility to shift the signal suppression into the red and infrared (IR) region because of the independence on stimulated emission, minimizing also photoinduced damaging. The manganese-doped ZnSe quantum dots exhibit similar properties as labels with stable “off states” (switchable proteins or switchable organic dyes) regarding the low switching intensities, but instantaneous switching kinetics, because a molecular rearrangement is not necessary. An essential disadvantage of the high fluorescence lifetime is the need for long integration times to collect enough photons, which in turn increases the light dose.

The results show that Mn doped ZnSe QDs can be applied in RESOLFT experiments in the same way as any other organic photoswitcher suggesting a more than fourfold resolution enhancement compared to confocal microscopy. The fluorescence from Mn doped ZnSe QDs can be reversibly inhibited with over 90% efficiency using a cw laser by an excited state absorption process. The modulation is achieved directly by light and does not need an external photochromic activator or quencher. It relies only on internal electronic transitions.

5.4 Experimental section

5.4.1 *Setup*

Quasi-continuous excitation of the Mn-doped quantum dots (NN-Labs) was achieved using a laser diode source at a wavelength of $\lambda_{exe} = 440$ nm, which had an inter-pulse dwell time (200 ns) much shorter than the lifetime of the Mn-doped quantum dots (~90 µs). Fluorescence depletion at $\lambda_{mod} = 676$ nm was accomplished using cw Ar-Kr-laser. Collected fluorescence passed through an additional band-pass filter (40 nm band-pass centred at 580 nm, AHF Analysentechnik, Tübingen, Germany). As a phase plate two identical adjacent optical flats are a placed in the modulation beam, and one is tilted slightly to adjust the path length in one half of the beam. When focused, the resulting point-spread function (PSF) contains a line through its center that can be used to selectively inhibit Mn-QD fluorescence. Alternatively, a vortex phase plate (RPC Photonics, NY, USA) was used in the modulation beam path to generate a donut shaped point spread function in the focus. The diffraction-limited PSFs of the excitation and modulation beams are characterized by scanning nanometric gold particles (80 nm suspended in Canada-Balsam) through their foci while detecting the back-scattered laser light. Results of this measurement are shown in Fig. 5.9.

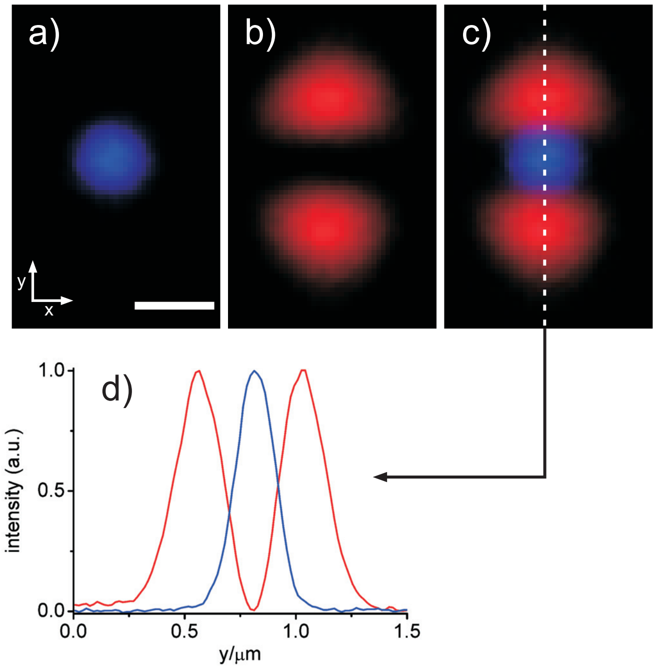

Fig. 5.9: Point-spread functions of the (**a**) excitation and (**b**) modulation beam. Panel (**c**) illustrates the spatial overlap of the two beams in the x-y directions. A line cut through the vertical center of (**c**) is shown in panel (**d**). The scale bar in (**a**) corresponds to 400 nm.

5.4.2 Lifetime measurement

Pulsed laser radiation (PicoQuant) at 405 nm was used to excite Mn-QDs in solution (20 µM dissolved in toluene) and the resultant time-domain fluorescence signal was processed with a time-correlated single-photon counting module (Picoquant). Data from this experiment is shown in Fig. 5.10 where it is observed that the fluorescent decay is multi-exponential in nature. A triple exponential fit to the data and indicates three decay regimes of 2 µs, 21 µs, and 90 µs. For the calculation of the net ESA cross-section, ζ_{ESA}, τ_{fl} = 90 µs was used for the fluorescence lifetime as it is the longest observed component.

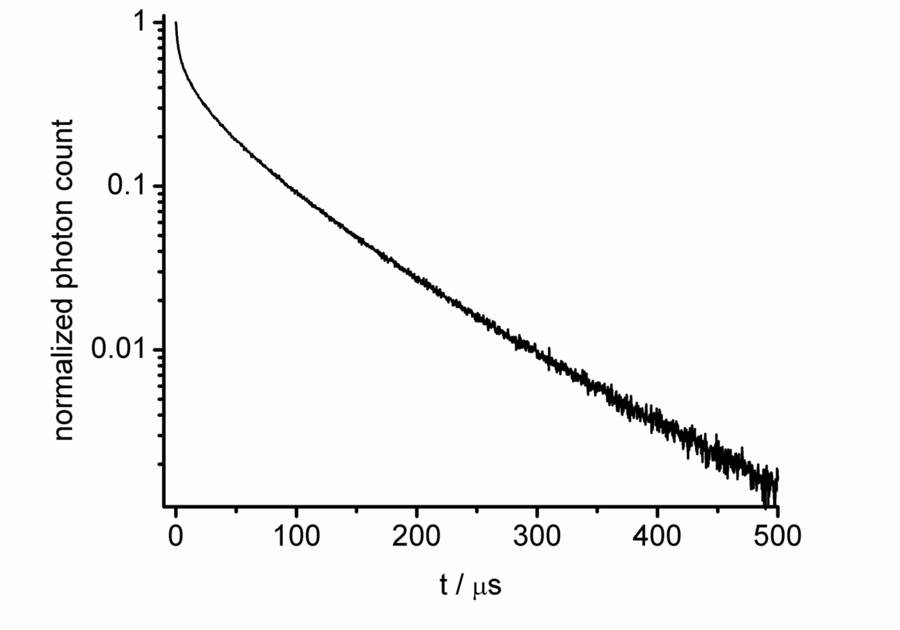

Fig. 5.10: Fluorescence decay curve for Mn-doped quantum dots.

Chapter 6

2,2´-Thiodiethanol (TDE) as an embedding medium

6.1 Introduction

In this chapter, another chemical based strategy to establish best optical conditions by matching the sample´s refractive index to that of the immersion system using a novel embedding media is described. This is mandatory to prevent spherical aberrations and to render the probe scanning the sample as small as possible according to diffraction theory. The signal-to-noise ratio (SN) can therefore be enhanced and furthermore, the excitation intensity and the photobleaching can be minimized. Matching the refractive index is of vitally importance in all optical high resolution modalities, especially when imaging deeply in the sample (Fig. 6.7). The here introduced embedding media features antioxidant properties and can be effective due to its high concentration.

Diffraction theory dictates that the lateral width of the main maximum of the PSF of a lens decreases linearly in size with its numerical aperture (*NA*); along the optic axis (*z*) the decrease is even quadratic (Eq. 2.3, 2.4). Since the *NA* is given by $n*sin\alpha$, optical microscopy has struggled to accommodate semi-aperture angles α and refractive indices n to be as large as possible. Due to the relatively large n that is close to that of glass coverslips (1.515), optical–grade oil has become the standard immersion liquid for high aperture lenses and, by the same token, oil immersion lenses have become the gold standard for high resolution optical microscopy. The glass-oil immersion system offers a well-matched, optically homogenous system that yields a focal spot that is ideally only limited by diffraction. Unfortunately, the situation deteriorates if the converging spherical wave fronts are focused into a sample with a different index of refraction, such as a sample that is mounted in a glycerol-based medium (n = 1.43-1.47) or into a sample that is kept in an aqueous buffer. In this case, the focal spot is blurred due to the spherical aberrations resulting from the mismatch in n (Hell et al., 1993) (Fig. 6.1).

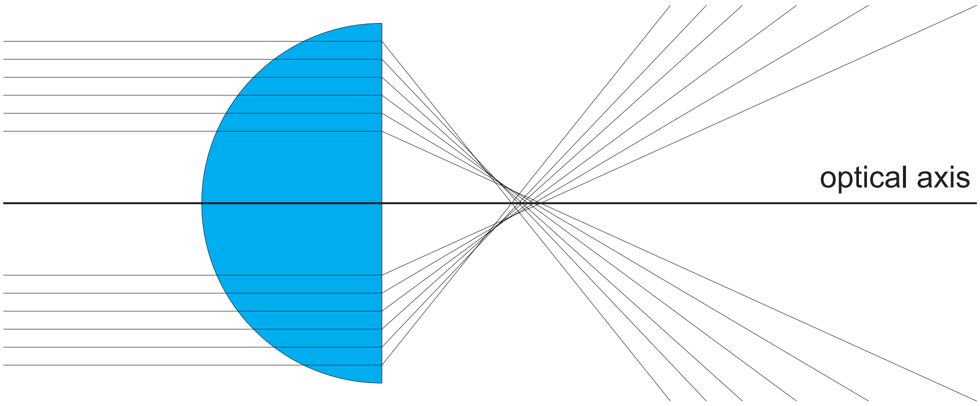

Fig 6.1: Spherical aberration describes the effect that rays close to the optical axis exhibit a different focal length as peripheral rays. The focal spot becomes blurred due to a mismatched refractive index.

The problems arising from mismatched *n* are prevalent both in conventional and confocal microscopy (Pawley, 1995), but in the latter, they are clearly manifested as a loss of image brightness and poorer optical sectioning (Egner et al., 1998; Hell et al., 1993). Therefore, during the last decade, most microscope manufacturers have developed high aperture water immersion lenses of $NA = 1.2$, i.e. $\alpha = 64°$, that are essential for 3D high resolution imaging of live cells.

In order to account for the fact that most fixed cells are mounted in glycerol-based media, coverslip-corrected glycerol immersion lenses have also been developed. Featuring an angle of $\alpha = 68.5°$, the most sophisticated version of these lenses ($NA = 1.35$) enable the nearly aberration-free high resolution imaging of glycerol mounted samples (Martini et al., 2002), in the conventional, confocal, as well as in the 4Pi mode (Gugel et al., 2004). However, besides being expensive, a limitation of the $NA = 1.35$ glycerol lenses is that they require the use of fused silica coverslips of non-standard thickness and glycerol as an immersion medium.

A common way to increase the refractive index in an aqueous mounting medium is to add proteins such as bovine serum albumine or glucose (Müller, 1956). However, the adjustable range of the refractive index is here limited from 1.33 to about 1.43.

Increasing the *NA* by increasing the aperture angle as well as the refractive index of the mounting medium pays off in many regards. For example, water immersion lenses with $NA = 1.2$, i.e. $\alpha = 64°$, have a 40% poorer axial resolution as compared to the 1.46 oil immersion lenses featuring $\alpha = 75°$ (Fig. 6.2). The larger α of the latter also leads to about a 30% larger fluorescence collection. However, a simple consideration based on geometrical optics shows that if the n of the mounting medium varies by 0.001, the marginal rays at $\alpha = 75°$ already miss the focal point by about the wavelength of light, at a sample depth of 30 µm. This departure is 4 times smaller at $\alpha = 59°$ of a 1.3 NA oil immersion objective. This simple example illustrates the importance of refractive index matching when high angle lenses are to be employed.

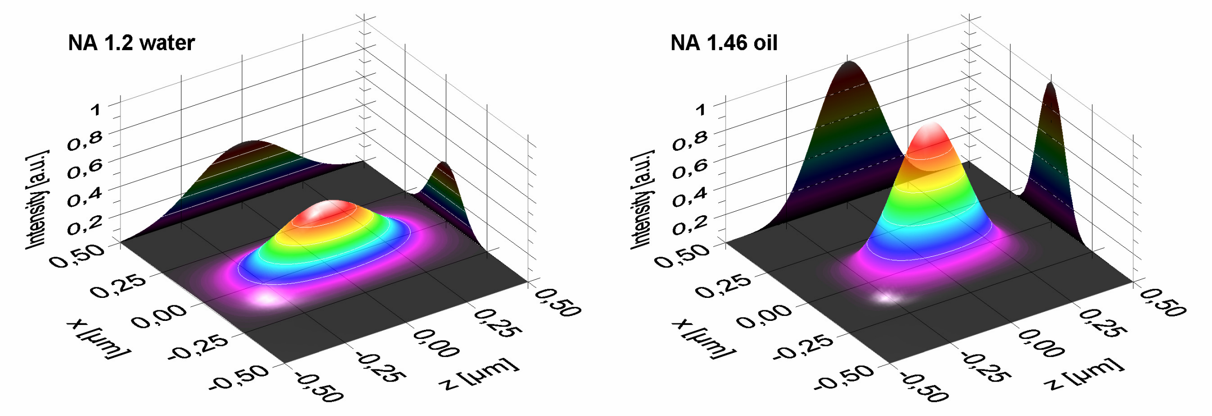

Fig. 6.2: Surface plots of an axial section (*xz*) of the main maximum of the PSF of a confocal microscope for a water immersion lens with $NA = 1.2$ (left) and an oil immersion lens with $NA = 1.46$ (right); excitation: 488 nm, emission: 525 nm. The PSF of the oil immersion lens is narrower by 30% along the *z*-axis. Additionally, the 30% larger collection and excitation efficiency results in an almost doubled peak intensity.

The use of high angle lenses therefore calls for an embedding medium whose refractive index can be precisely controlled. Ideally, it is miscible with water at any concentration, non-toxic and easily applicable to biological samples. It should quickly immerse all the structures without destroying or deforming them and must not quench the fluorescence notably.

Recently, ultramicroscopy was combined with a special procedure to clear tissue for the investigations of whole mouse brains (Dodt et al., 2007). In this kind of microscopy, the specimen is illuminated from the side with a thin light sheet. The parts of the specimen which are located above and below the light sheet are not illuminated. Therefore no out-of-focus light is generated, and no light has to be excluded to reach the detector as it is the case in confocal microscopy. Large objects can be investigated by ultramicroscopy, but they have to be optically transparent. To ensure transparency, the refractive index has to be matched over the whole tissue. This was achieved by embedding in a benzylalcohol/benzylbenzoat (BABB) (1:2) mixture. However, the BABB mixture is not water-soluble and the tissue has to be dehydrated in an elaborate and time-consuming procedure, which may disturb the 3D structure. A water-soluble embedding medium would simplify the procedure.

6.2 Application of TDE in confocal microscopy

In order to identify mounting media with the proper refractive index, the properties of 12000 substances were screened in Weast, 1974, with regard to refractive index, solubility in water, pH value, toxicity and stability. TDE (2,2'-thiodiethanol), a glycol derivative, was identified as a very promising candidate (Fig. 6.3). Used as an antioxidant for the chromatography of amino acids (Moore and Stein, 1951), it should display similar antioxidant properties in fluorescent microscopy. Highly reactive radical species generated by light are often responsible for the fading of fluorescence because they react with the fluorescent dyes. TDE is an inexpensive and almost odorless chemical. It is classified as being irritating but non-toxic. Further mounting media candidates are also to be found among the organic iodides, sulfides (thioles), and aromatic compounds featuring strongly polarizable groups. Derivatives of TDE with higher chain lengths, bearing a certain number of ethylene glycol, mercapto ethanol or dimercapto ethane groups, are also among highly promising substances for the sample embedding. However, toxicity, reactivity and low solubility in water may limit the number of useful ones. Therefore, this study was limited to TDE.

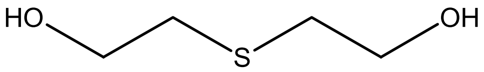

Fig. 6.3: TDE (2,2'-thiodiethanol) is a non-toxic glycol derivative which, owing to the sulfur atom, exhibits a large polarizability and hence a high refractive index. It is soluble in water at any concentration.

The data in Fig. 6.4 shows that adjusting the amount of water in TDE allows a precise control of the refractive index of the medium (for measurements of the refractive indices, see appendix A.4.10). Therefore, it is possible to tune the refractive index of the sample to that of the immersion oil (n_D = 1.518 at 23°C).

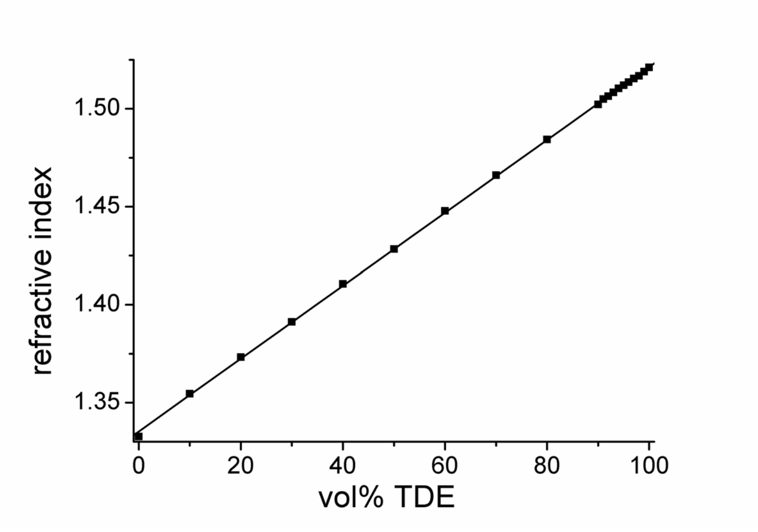

Fig. 6.4: TDE (2,2'-thiodiethanol) is miscible with water in any proportion. The refractive index (n_D) of the solution can be precisely tuned to any value between 1.333 (water) and 1.521. The latter is even slightly larger than that of immersion oil ($n_D = 1.518$ at 23°C).

The precision of the refractive index tuning is further evidenced in Fig. 6.5 showing the range around 1.51 in detail. A 97% TDE volume yields a refractive index which perfectly matches that of immersion oil at room temperature. By the same token, it is possible to match the refractive index for different ambient temperatures.

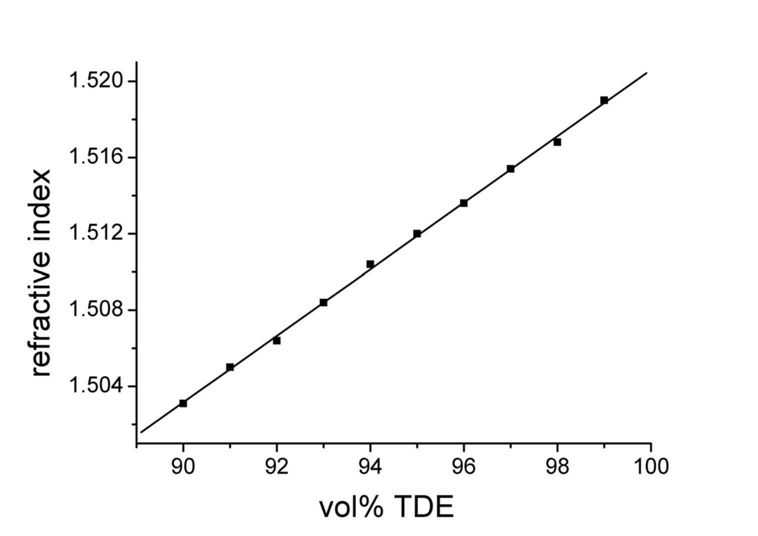

Fig. 6.5: TDE allows a precise setting of the refractive index by adjusting the water content. For use with an oil immersion lens, a TDE concentration of 97% in water was employed.

As expected, embedding cells in a 97% TDE solution significantly reduces the phase contrast which demonstrates the improvement of the optical properties of fixed samples for high resolution imaging (Fig.6.6).

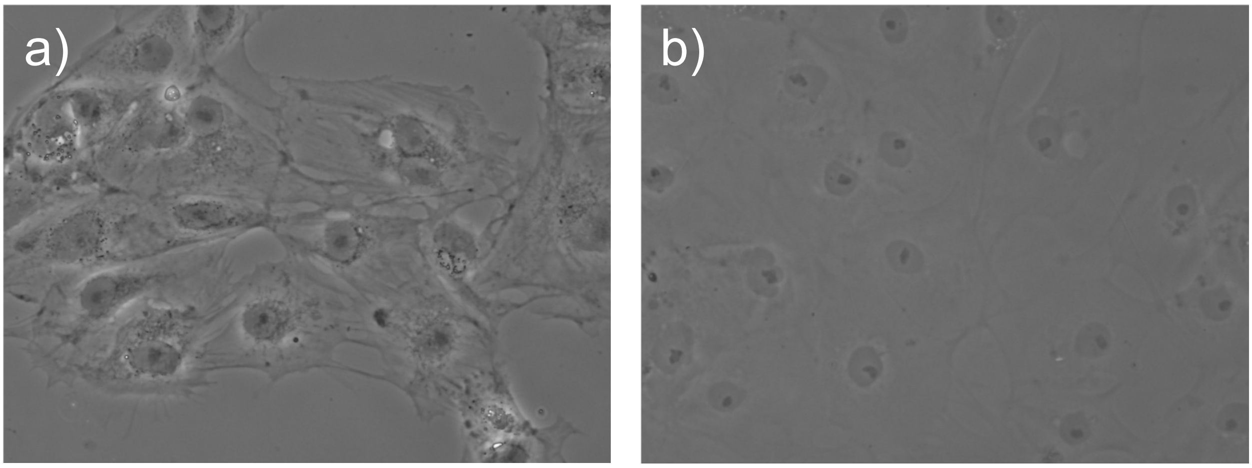

Fig. 6.6: Phase contrast images of PtK2 cells. a) Cells mounted in buffer solution. b) Cells mounted in 97% TDE solution. As expected, the contrast generated by local refractive index changes is greatly reduced in TDE.

The effect of spherical aberrations caused by refractive index mismatch in the mounting medium is easily measured by evaluating an *xz*-scan of a homogeneous dye solution in a confocal microscope. We recorded such an *xz*-scan using a 100x NA1.46 oil immersion lens featuring $\alpha = 75°$. The fluorophore Rhodamine 6G was dissolved in PBS buffer containing different amounts of TDE to set certain refractive indices in the mounting medium. Fig. 6.7 shows the measured intensity along the optical axis. The intensity drops quickly after a few µm in depth if the refractive index does not match that of the immersion system. The loss of resolution and intensity is most dramatic at $n = 1.33$ (water) and $n = 1.45$ corresponding to 20/80 Water/Glycerol solution. But there is still a significant effect at $n = 1.50$ which is closer to glass than polymer-mounted samples such as PMA or Mowiol (n = 1.49). Evidently, only the correct setting of the refractive index at $n = 1.515$ at 97% TDE avoids aberrations in the sample and optimizes the fluorescence collection.

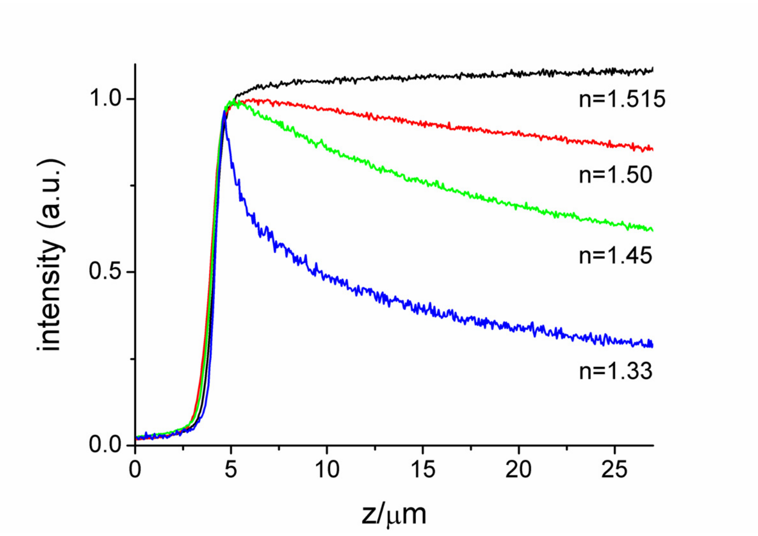

Fig. 6.7: Confocal axial (*z*-) scans at the interface of a dye solution with the glass coverslip using an oil immersion lens of 1.46 *NA*, $\alpha = 75°$. The coverslip is located at $z = 4.0$ µm. At positions $z < 4$ µm is glass and dye solution at $z > 4$ µm. The curves correspond to 4 different refractive indices set by using different TDE concentrations, as indicated. The deeper the beam is focused into the sample, the fewer photons are collected due to spherical aberrations introduced by refractive index mismatch. In case of matching refractive index the signal is constant along the optic axis.

One has to point out, that TDE is hygroscopic. This must be taken into account during preparation and for handling the stock solutions.

To provide an overview about the general applicability and behavior of popular classes of dyes, the fluorescence efficiencies of dyes have been measured in phosphate buffered saline (PBS) and TDE using a fluorescence spectrometer. The results are summarized in Tab. 6.1 showing the relative absorption (*Abs*), emission (*Em*) and quantum yields (QY_{rel}) of the dyes as defined by

$$QY_{rel} = \frac{Em_{TDE}}{Em_{PBS}} \cdot \frac{Abs_{PBS}}{Abs_{TDE}}. \tag{6.1}$$

Tab 6.1 allows a quick and practical comparison of the fluorescence yields of the dyes mounted in TDE or PBS. We selected representative derivatives of coumarins, rhodamines, carbopyronines, cyanines, and boradiazaindacenes. In addition, we also investigated the behavior of fluorescent proteins and quantum dots.

		PBS (Ref.)				**TDE**					
		Abs.	λ_{Abs}[nm]	Em. [a. u.]	λ_{Em}[nm]	Abs.	λ_{Abs}[nm]	Em. [a. u.]	λ_{Em}[nm]	rel. QY	
Coumarins	Coumarin 120	0.092	342	580	444	0.119	342	315	438	0.42	
	Coumarin 153	0.029	434	75	550	0.055	434	348	539	2.45	
Rhodamines	FITC Isomer I	0.135	495	812	518	0.154	505	560	532	0.60	
	Oregon Green 488	0.047	493	800	518	0.057	506	595	530	0.61	
	Texas Red mixed Iso.	0.025	586	820	605	0.027	590	830	607	0.94	
	Atto565	0.031	567	210	586	0.049	567	460	589	1.39	
	A532	0.027	532	317	550	0.034	542	240	559	0.60	
Oxazines	Atto655-NHS	0.039	661	590	676	0.051	666	720	686	0.93	
Cyanines	Cy3	0.037	551	135	563	0.036	563	595	576	4.53	
Boradiazaindacenes	Bodipy 650/665-x	-	-	-	-	0.072	662	900	677	-	1*
	Bodipy FL-SE	0.016	502	536	510	0.030	510	488	518	0,49	
Fluor. Proteins	EGFP	0.008	489	277	520	0.014	490	343	510	0.71	2*
	mRFP	0.081	586	505	606	0.088	587	467	608	0.85	

Tab. 6.1: Absorption (*Abs.*) and fluorescence intensities (*Em.*) of dye solutions in PBS buffer and TDE (97%) were measured as well as the wavelengths λ of the absorption and emission maxima. To compare the effective fluorescence behavior of the dyes in TDE with PBS buffer, the relative quantum yields (QY_{rel}) according to Eq. 6.1 are shown in the last column. Values >1 indicate stronger fluorescence in TDE. For further information see appendix A.4.8. (*1* Bodipy is quenched in buffer due to dimerisation; 2* in 80% TDE)*

The data shows that in some cases the fluorescence brightness is slightly lower in TDE as compared to PBS. However, in practical microscopy, this minor effect is usually compensated by the larger collection efficiency of the high *NA* lens. Nevertheless, also the opposite effect, i.e. stronger fluorescence is observed in a number of cases.

Absorption and emission spectra (see appendix A.4.9 for further information) were found to be slightly altered by the mounting medium, which is a quite common phenomenon when dye molecules are embedded into media with different polarizability. The absorption spectra also appear slightly red-shifted in accordance with Kundt's rule and other related effects (LeRosen and Reid, 1952). Fig. 6.8 gives an example with the commonly used fluorescent marker Oregon Green. The excitation and emission filters of the microscopes may therefore require slight adaptations. On the other hand, no significant differences have been observed when using different buffers such as PBS, HEPES, TRIS, or HBS-buffer for index adjustment of the TDE-based medium.

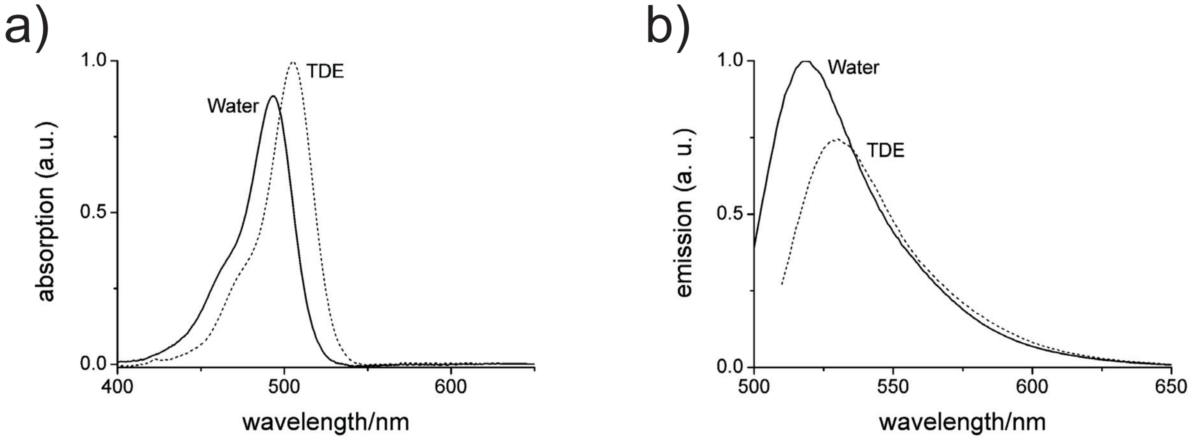

Fig. 6.8: Comparison of the absorption (**a**) and emission (**b**) spectra of Oregon Green measured in water and in 97% TDE. The spectra are red shifted by 12 nm.

Cell membranes are permeable for TDE; hence, permeabilization with detergents such as Triton X-100 is not required. Virtually all standard procedures of labelling with exogenous fluorophores, such as immunostaining or chromatine labelling with DAPI worked flawlessly. As the only exceptions, phalloidin-conjugated fluorophores used to stain the actin cytoskeleton and bungarotoxin-conjugated dyes used to stain the acetylcholin receptors have been destabilized in TDE. A remedy may be a strong post-fixation after phalloidin incubation. Even after the exchange of the TDE with water and renewed addition of the bungarotoxin-dye conjugate, a specific labelling was not achieved.

Interestingly, the brightness of fluorescent proteins (FP) increases with increasing fraction of TDE in the medium up to a certain TDE concentration. Mammalian cells (PtK2 cell line) were prepared in which a matrix-resident mitochondrial protein was fused with the enhanced green fluorescent protein (EGFP). We found that EGFP was quenched if the TDE fraction was > 80-85%. In contrast, the fluorescence of the monomeric red fluorescent protein (mRFP) is not affected by high TDE concentrations. At a 97% TDE concentration ($n = 1.515$), mRFP performs virtually as in PBS. Hence, while it seems to be difficult to match EGFP mounted fixed samples to a refractive index $n > 1.48$, it possible to embed mRFP labelled samples in a strongly concentrated TDE based medium with large refractive index. Semiconductor quantum dots and fluorescent beads performed well in the TDE based solution at all TDE concentrations.

It was also observed that some dyes, e.g. Cy3, Coumarin153 and Atto565 displayed increased brightness while other dyes became dimmer in TDE compared to PBS. Interestingly, Cy3 emitted over 4 times more intensely in TDE, which may be attributed to the stabilizing of this photoisomerizable molecule in the fluorescent trans-state of the cis-trans system (Heilemann et al., 2005), (Widengren and Schwille, 2000). It is quite probable, that radical reactions with the double bonds creating a single bond are involved in the isomerization of cyanin dyes because of the free rotability of the single bonds. TDE might quench this radical reaction predominately reacting with radicals.

The general applicability of TDE as a mounting medium for fluorescence imaging is exemplified in Figs. 6.9-6.13. Here, different cellular structures in PtK2 cells are stained following the protocols described in appendix A.4.3 and A.4.4.

6.2.1 Preparation

At first, the staining and fixation of cells was performed as in conventional or confocal fluorescence microscopy (see appendix A.4.3 - A.4.7). When using TDE in biological samples, one must consider that 1) by adding an adequate buffer (for example, pH 8), the pH is set to the value required for optimum performance of the used dye. 2). The exchange of water with TDE (97% for oil immersion) must be slow enough to prevent cell shrinkage due to osmotic shock (TDE enters the cell or nucleus slower than water leaves it due to their different permeabilities).

6.2.2 Mounting procedure

After fixation of the cells and depending on the sample, various dilutions with increasing TDE content were used to exchange the water with TDE in a continuous or stepwise manner. Good results have been obtained with the following steps:

10% TDE (100µl TDE, 50 µl PBS5x, 850µl water),
25% TDE (250µl TDE, 50µl PBS5x, 700µl water),
50% TDE (500µl TDE, 50µl PBS5x, 450µl water),
three times 97% TDE (970µl TDE, 30µl PBS1x).

The pH value of all stock solutions was controlled by a pH meter (see appendix A.4.13). Because of the viscosity of TDE, it is important to wait for an hour for the settling to the final measurement value of the pH.

The samples were successively immersed in the above solutions with increasing TDE concentrations for about 5 to 10 minutes each. Then the coverslips of the samples were sealed with pink nail polish. It was ascertained that the silicon-based glue Twinsil (Picodent, Wipperfürth, Germany) is not polymerizing with TDE. The refractive index of the solution was examined with a refractometer (see appendix A.4.10). At the microscope, the correction collar of the objective lens was adjusted to maximum fluorescence brightness. This corrects for residual spherical aberrations due to temperature or coverslip thickness mismatches. To observe potential quenching effects of TDE, micromolar dye solutions in TDE were examined in a Varian fluorescence spectrometer (see Tab. 6.1).

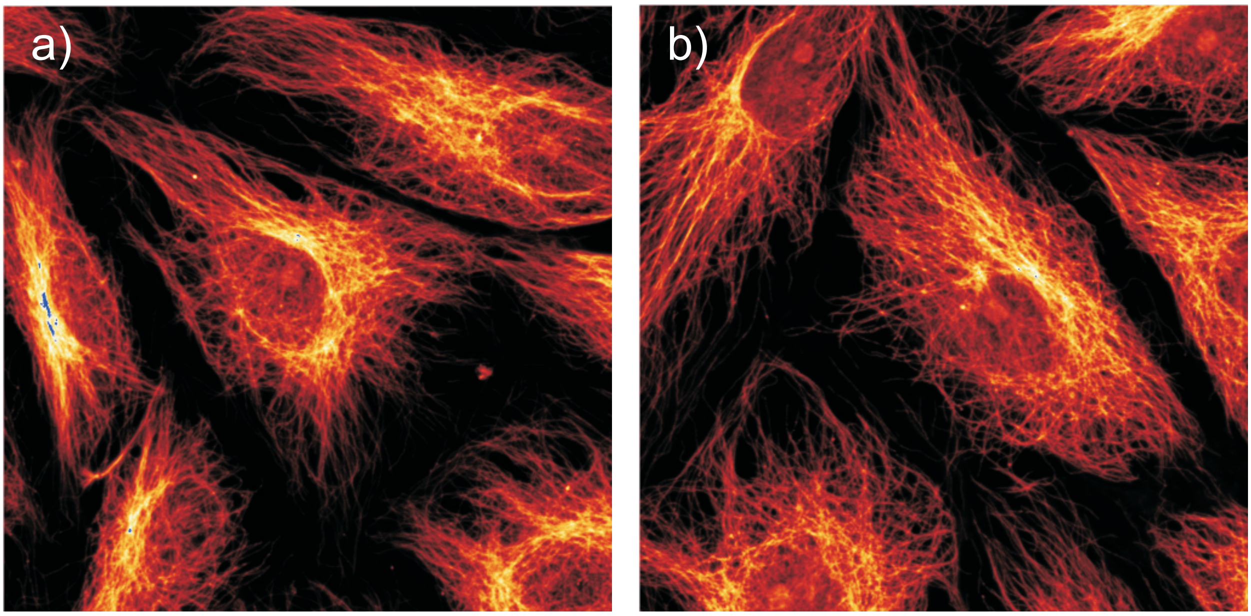

Fig. 6.9: PtK2 cells with immunolabelled microtubules mounted in PBS (**a**) and in 97% TDE (**b**) demonstrate the viability of TDE as an embedding medium. Immunolabelling with the fluorophore Dy-485XL. No structural difference or substantial difference in image brightness is observed.

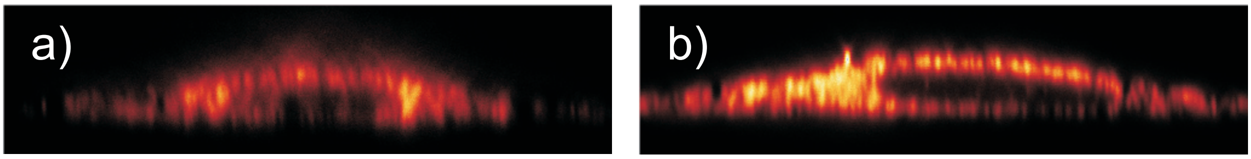

Fig. 6.10: PtK2 cells as in Fig. 6.9; confocal *xz*-sections show the conservation of the 3D-structure in 97% TDE.

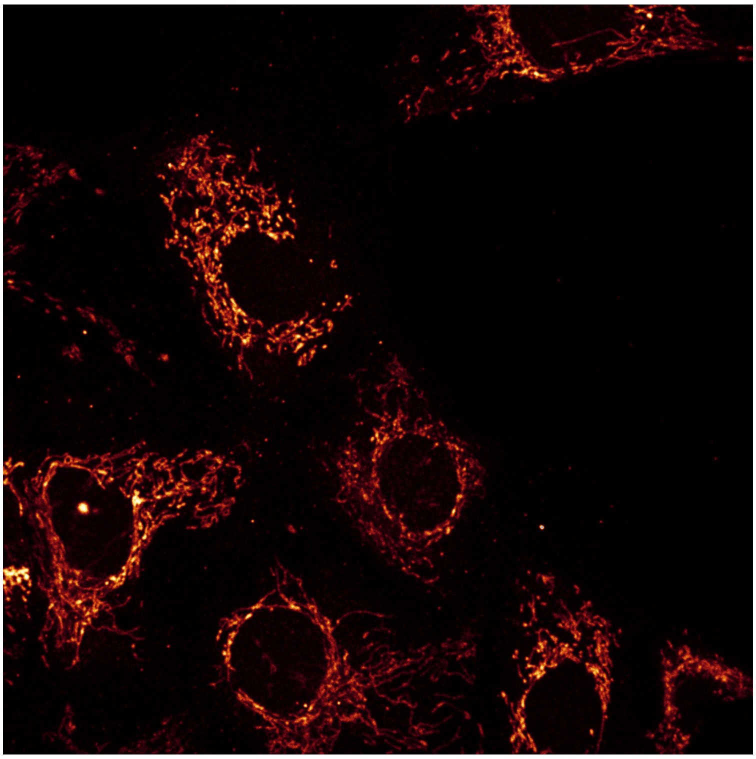

Fig. 6.11: PtK2 cells in 97% TDE. ATP-Synthase immunostained with ALEXA546.

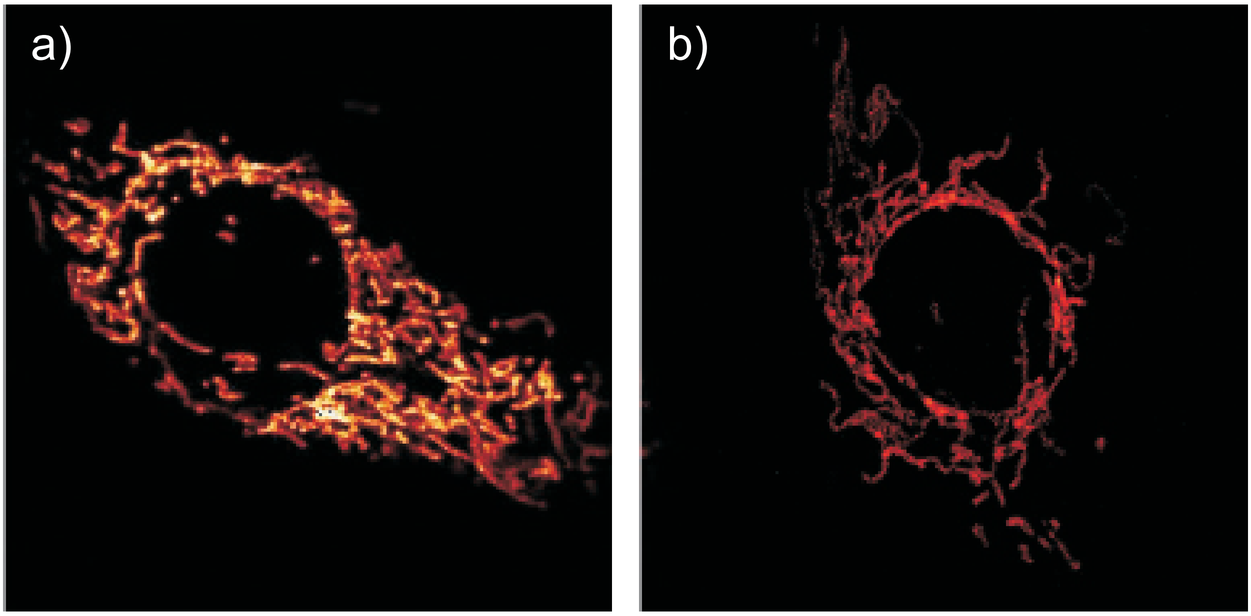

Fig. 6.12: (**a**) PtK2 cell in 97% TDE. Mitochondrial matrix stained with DsRed. (**b**) PtK2 cell in 85% TDE: Mitochondrial matrix stained with EGFP.

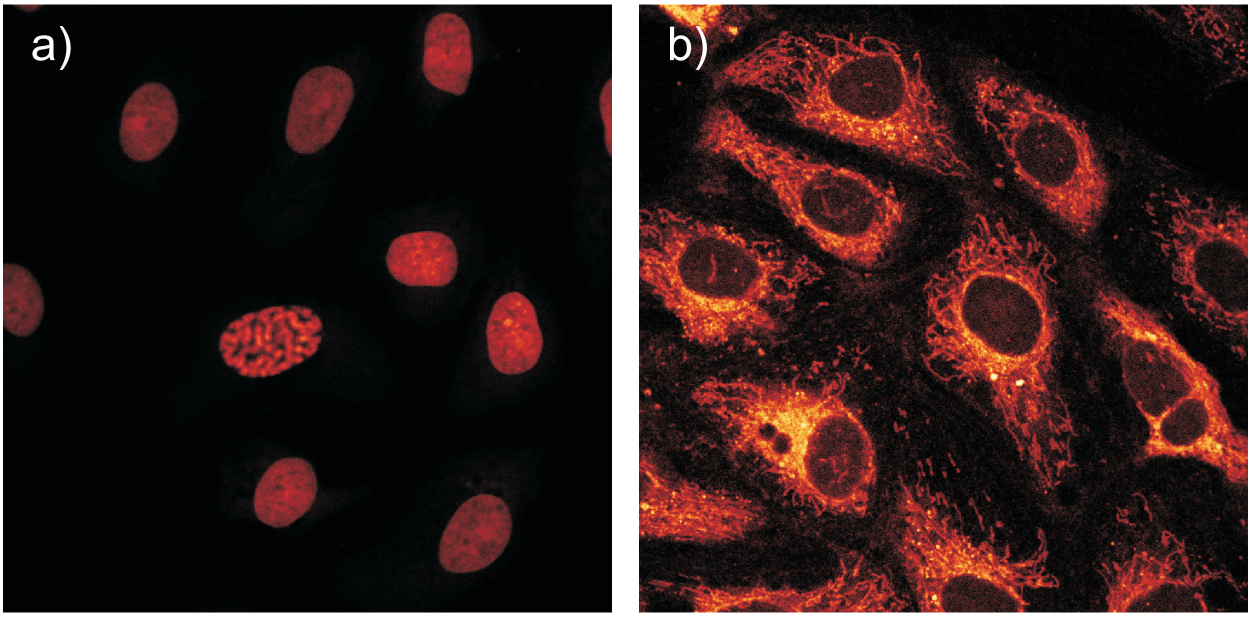

Fig. 6.13: PtK2 cells embedded in 97% TDE. (**a**) DAPI staining of nuclei. (**b**) Mitochondria stained with DIOC6.

Unless the exchange process is too fast, the replacement of water by TDE does not disturb the 3D structure of the cell. Water can obviously penetrate cellular or nuclear membranes much faster than TDE, but this can be easily accounted for by a stepwise or continuous solution exchange as described. The usefulness of TDE is further supported by the fact that immunostaining and DNA staining using DAPI is possible, as well as the imaging with quantum dots and fluorescent proteins. If nuclear stains are used showing an increased quantum yield upon binding on DNA, it is recommended to supply the TDE used for the last water exchange step with the nuclear stain to compensate for the loss due to the exchange steps. The only exceptions with regard to applicability is that, unlike the fluorescence of mRFP, that of EGFP is quenched for TDE concentrations larger than 80%, that is for refractive indices >1.48 This observation might give further hints to the fluorescence properties of EGFP and will be investigated in the future. Two toxins have been tested in TDE, phalloidin- and bungarotoxin, but both are not working. Toxins are highly specific and their binding is dependent on the conformation of the epitope-bearing protein. The binding properties of most of the used antibodies are not strictly depending on the conformation but also detect the denatured epitope (e.g. in Western Blotting). Changes of the protein conformations after TDE embedding are highly probable because of dehydration or interactions with the hydroxy groups and the sulfur of the TDE itself. This might explain the different performances of the toxins compared to the antibodies in TDE. A hint for conformational changes after TDE embedding is the fluorescence quenching of GFP in higher

TDE concentrations. Maybe there are additional restrictions regarding toxins or conformation-dependent applications in TDE.

The observed spectral shifts by a few nanometers are in accordance with the fact that the change in fluorophore-solvent interactions influences the electronic transitions of the fluorophore. For the same reason, the fluorescence quantum yield of a number of dyes is slightly modulated. However, in most cases, these changes are surprisingly subtle and do not compromise the usefulness of TDE as a mounting medium. Last but not least, the reducing property of TDE helps to reduce photobleaching. A positive effect was found on light-induced strand breaks of YOYO-1 labelled Lambda DNA, which was combed on a vinylated glass surface (Akerman et al., 1996), but was not further quantified. The highly reactive radicals and oxygen species generated by the dye molecules in the excited state are maybe quenched by TDE and therefore not able to attack the DNA. A similar result was found applying moderate concentrations of β-mercaptoethanole or ascorbic acid on preventing strand breaks of combed lambda DNA and reconstituted DNA (Akerman et al., 1996, Yoshikawa et al., 2006).

Another interesting application is the use of TDE as an immersion fluid. The unavoidable change of the refractive index in the immersion oil can be compensated in TDE by adjusting the proper concentration. Of course it must be ensured that the last optical element of the objective lens is not harmed by the TDE based medium.

6.3 Physical properties of TDE

Fortunately, other physical properties of TDE are advantageous for microscopy proved by the following measurements. The dispersion of TDE (97% + 3% PBS buffer) is similar to that of the regular immersion medium. Hence, TDE does not induce chromatic aberrations in multicolor imaging or when imaging fluorophores with a large Stokes shift (see Fig. 6.14). The temperature dependence of the refractive index is displayed in Fig. 6.15 showing that TDE features a more moderate temperature dependence compared to that of immersion oil. This is an advantage if TDE is also used as an immersion fluid, because temperature differences within the immersion-sample system are better tolerated and not leading to stronger refractive index inhomogeneities.

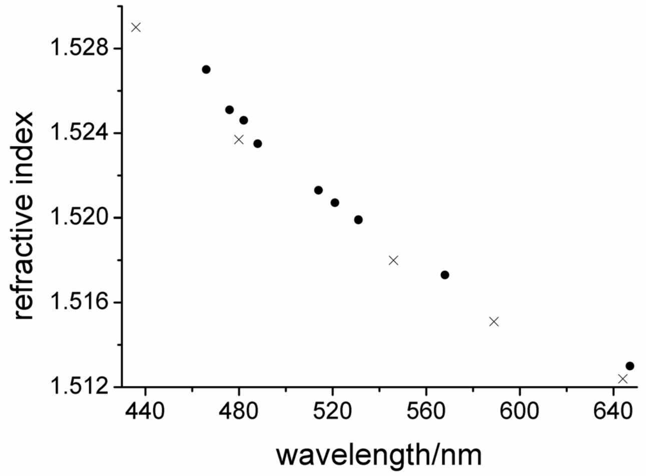

Fig. 6.14: The dispersion of TDE (dot) is close to the dispersion of standard immersion oil (Leica Microsystems) (cross). This avoids the chromatic aberrations otherwise introduced by the mounting medium.

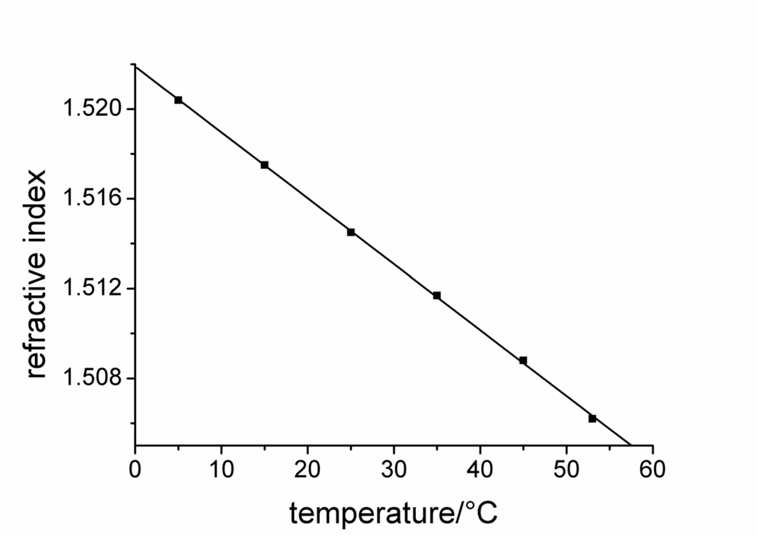

Fig. 6.15: The temperature dependence of the refractive index of TDE ($3*10^{-4}$/°C) is slightly less than that of the immersion oil ($3.8*10^{-4}$/°C).

The investigation of TDE in the bulk measured with a fluorescence spectrometer shows weak autofluorescence around 430 nm and 570 nm for excitation at 350 nm and 510 nm, respectively. However, the autofluorescence is so low that it is hardly noticeable in conventional fluorescence microscopy applications and can be regard as irrelevant in confocal recordings.

The optical absorption of TDE in the visible range is low and can be neglected for all microscopy applications. This is evidenced in Fig. 6.16, showing the optical transmission through a 10 mm thick layer of TDE.

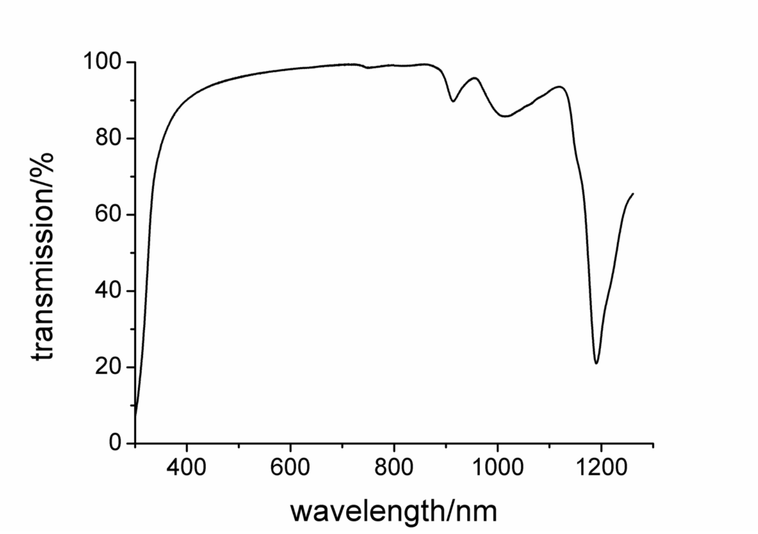

Fig. 6.16: The transmission spectrum of TDE (10 mm thickness) shows minimal absorption over the entire visible and near infrared range. For a microscope sample of 100 µm thickness, the transmission in the 360-1100 nm spectral range is >99%.

6.4 TDE in 4Pi microscopy

In every microscopy mode using high *NA* objective lenses matching the refractive index is a crucial step. A difference between the refractive indices of the immersion system and the sample embedding, or within the sample embedding itself leads to a spherical aberrated PSF featuring a degraded and displaced peak amplitude, increased lobes, a blurred maximum, a change in phase at the maximum and a shifted focus. The intensity of the aberrations ultimately depend on the amount of the refractive index mismatch, the penetration depth and the aperture angle of the used objective (Egner et al., 1998). These effects become exacerbated for confocal and multi-photon microscopes (Hell et al., 1993; Jacobsen et al., 1994), since the imaging properties of these systems are governed by a squared or higher order intensity PSF. The same holds for 4Pi-imaging, a method for improving far-field resolution through combining the aperture of two objective lenses. The effective PSF for 4Pi of type C is given by:

$$h_{eff}(\vec{r}\,) = h_{exc}(\vec{r}\,) \cdot h_{det}(\vec{r}\,) = \left|\vec{E}_{exc}(\vec{r}\,) + \hat{M}\vec{E}_{exc}(\hat{M}\vec{r}\,)\right|^{2m} \cdot \left|\vec{E}_{det}(\vec{r}\,) + \hat{M}\vec{E}_{det}(\hat{M}\vec{r}\,)\right|^{2} \otimes p(\vec{r}\,) \qquad (6.2)$$

$\vec{E}_{exc}$ and $\vec{E}_{det}$ denote the focal fields describing the illumination and the detection by a single lens at the excitation (λ_{exc}) and fluorescence wavelength (λ_{fl}) respectively; $\vec{r}$ is a spatial coordinate originating at the focal point; $h_{exc}(\vec{r}\,)$ and $h_{det}(\vec{r}\,)$ are referred to as the excitation and detection PSF respectively. The transformation matrix $\hat{M}$ considers the orientation of the counter propagating light fields. The function $p(\vec{r}\,)$ describes the opening of the detector that is conjugate to the focal plane, e.g. the area of a confocal pinhole. If no pinhole is used, $p(\vec{r}\,) = 1$. The parameter $m = 1, 2,\ldots$ gives the number of photons involved in the excitation process, e.g. $m = 2$ for two-photon excitation.

The maximum semi-aperture angle provided by standard high angle lenses of 68° is significantly smaller than the 90° which are needed to form a half sphere. Hence, the focal spot features high order lobes above and below the focal plane in axial direction. For lenses with $\alpha = 68°$ the first order lobes are occurring with 50% of the intensity of the main peak and are therefore to prominent to be neglected. The decrease of these side lobes is the primary concern in the 4Pi microscopy because side lobes lead to periodic artefacts in the image formation. To remove the side lobes the images gained in the 4Pi mode have to be processed mathematically applying a so called linear deconvolution with the whole effective PSF (Tikhonov et al., 1977). Deconvolution is always challenged by noise, so the generation of a nearly spherical spot by pure physics to probe the sample is preferable also in terms of the system´s alignement and recognizing constructive interference (Lang et al., 2008). A sharp spot with negligible lobes can be realized by two-photon excitation 4Pi microscopy of type C with novel oil-immersion lenses featuring an enlarged semi-aperture angle of $\alpha = 74°$ (Lang et al., 2007a, Lang et al. 2007b). But as mentioned above, in two-photon excitation 4Pi microscopy using high *NA* lenses, the importance of refractive index matching is exponentiated to ensure low spherical aberrations and a sharp spot. The embedding in TDE is mandatory to generate such a sharp spot with insignificant side lobes. This is confirmed in a *xz*-imaging experiment on microtubules in PtK2 cells stained with Alexa 488 (Fig. 6.17) following a protocol described in the appendix A.4.3. The side lobe effects in the raw data are already in the range of the background (10%). A profile through an inherently line-shaped microtubule shows that a single sharp central spot with an axial FWHM of about 120 nm is formed (Fig. 6.17c), indicating an axial resolution increase by a factor of 4.2 compared with the confocal measurement. The confocal data were recorded by blocking one of the arms of the 4Pi microscope at $\lambda_{exc} = 488$ nm. The low side lobes indicate the good match between the average refractive indices of the sample and the embedding medium TDE. Another indication of the match is the negligible variation in phase difference when scanning the focal spot through the sample. The imaged microtubules in PtK2 cells are located close to the nucleus (Fig. 6.17a, b). The line profile through the nucleus (indicated in blue) shows that the phase shift due to refractive index mismatch is negligible (Fig. 6.17c). Both the microtubules above and below the nucleus indicate constructive (c/c) interference between both counterpropagating wavefront pairs. The results confirm that no deconvolution is necessary to interpret the data obtained by two-photon 4Pi microscopy of type C using these high *NA* lenses. Another 4Pi mode is enabled by the TDE embedding and the application of high numerical aperture lenses, namely the one-photon excitation 4Pi of type C. Here the side lobes are low enough to make the two photon excitation redundant (Lang et al., 2007b).

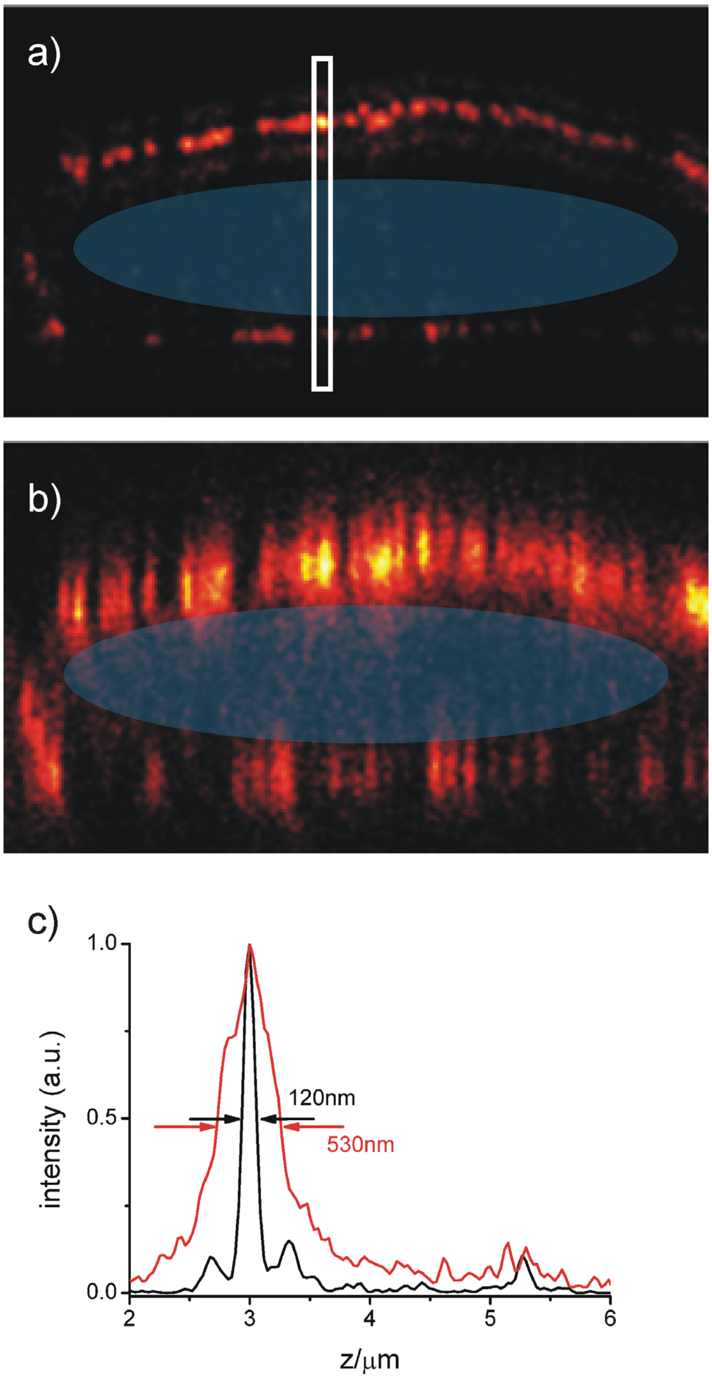

Fig. 6.17: 4Pi imaging of the microtubular network in a mammalian cell (PtK2) stained with Alexa 488. An *xz*-section ((**a**) 4Pi, (**b**) confocal) through the nucleus (indicated in blue) of an Alexa 488-stained microtubular network demonstrates that the embedding medium TDE allows precise matching of the refractive index to that of the immersion system: no significant phase shift due to the focusing through the cell nucleus was found (**c**). The deconvolution is not necessary, since the lobe-induced effects in the 4Pi raw data are weak, as confirmed by the *z*-profile (**c**) derived by integrating in the boxed area in (**a**).

6.5 TDE in STED microscopy

The requirements on dye molecules for high resolution microscopy are high compared to standard confocal microscopy in terms of the realization of a non-fluorescent state and the more important photostability. In RESOLFT modes using stable, long lived “off” states, the embedding ideally should not increase the switching fatigue, fluorescence intensities of the molecules in the “off” state or the times to switch on or off the dye molecules. Apparently, one has to count on interactions of the dye molecules with the embedding media, making the problem rather complex. Suitable dyes for high resolution experiments have to be tested individually. In STED microscopy, which is based on metastable “off” states, the sample embedding has to ensure good antifade properties to tolerate the higher light doses and must not decrease the efficiency for suppressing the fluorescence signal. To demonstrate the performance of different fluorescent dyes in combination with the embedding media TDE under STED conditions, the following images are shown.

Fig. 6.18 shows NK51-labelled SC35 splicing factors within the nucleus of MCF7 cells embedded in TDE to provide ideal optical properties. The nucleus of a cell is highly compartmentalized (Spector et al., 2001; Misteli et al. 2001). Speckles are one of these distinct subnuclear, dynamical structures located in the interchromatin regions of the nucleoplasm of mammalian cells, and are enriched in pre-messenger RNA splicing factors (Lamond et al., 2003). SC35 is a non snRNP and involved in the splicing process. Splicing is a fundamental step within the data flux from DNA to protein. After the transcription of the DNA, pre-mRNA is formed which is spliced, capped and tailed to form mRNA. Translation of mRNA leads to proteins (Alberts et al., 2002). The splicing factor SC35 is found to co-localize with snRNP aggregates in a speckled distribution (Sahlas et al., 1993). This factor plays a role in spliceosome assembly and initiates the splicing process (Fu and Maniatis, 1990; Spector et al., 1991). Its distribution can be described as an extensive, 3D network corresponding to interchromatin granules (ICGs) as assessed by electron microscopy (Spector et al., 1991). In the confocal microscope they appear as irregular punctuate structures varying in size and shape (Fig. 6.18a, b). The ICGs seen in electron microscopy range in size from one to several micrometers in diameter and are composed of 20 to 25 nm granules that are connected in places by a thin fibril, resulting in a beaded chain appearance (Thiry, 1995). The nuclear architecture of the MCF7 cells is additionally challenged by macromolecular crowding caused by a hypertonic treatment of the living cells with sucrose before fixation. Molecular crowding provokes structural re-organizations such as chromatin compactions and invasions or regeneration of nuclear components into newly emerged peripheral space between nuclear lamina and detached chromatin (Richter et al., 2007). The molecular crowding effect is not further discussed in the following. Fig. 6.18 directly compares the confocal image (a raw data, b linear deconvolved data) with the image recorded under STED conditions (Fig 6.18c, d). The STED mode clearly discerns features in the range of 50 nm in size, almost revealing the size of the granules assembling the speckles proofed by electron microscopy. The confocal image does not disclose any substructure within the speckles. This experiment proofs that the fluorescent dye NK51 is suitable for STED microscopy of TDE embedded samples. The refractive index mismatches near or within the nucleus are well compensated yielding a decent resolution. The resolution is mostly limited by the STED laser´s maximum power and the extensive dye distribution in the optical axis. An unmatched refractive index would lead to increased light scattering and spherical aberrations resulting in high intensities in the zero of the depletion beam, a worse resolution and a lower signal. Photobleaching is not of any concern in this case.

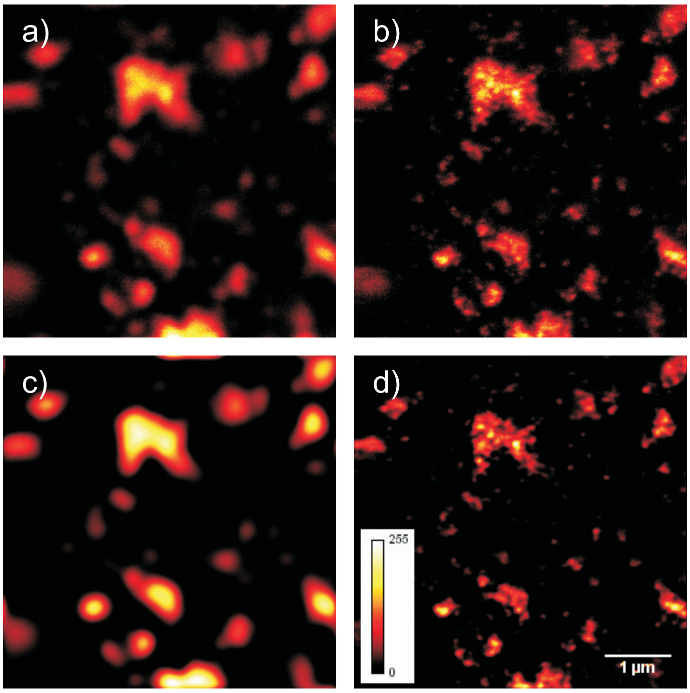

Fig. 6.18: STED measurement of NK51 labelled SC35 splicing factor in MCF7 cells which were crowded in 320 mM sucrose and embedded in TDE reveals substructures within nuclear speckles. In the first row the raw data of the STED image (**b**) and the confocal image (**a**) is shown. The second row (**c**) and (**d**) depicts the corresponding images after a linear deconvolution.

Another application of TDE embedding in STED microscopy is demonstrated in Fig. 6.19. Here, synaptophysin was labelled with Atto565 and NK51 to localize synaptic vesicles in the neuromuscular junction (MJ) within a fixed tringularis sterni muscle prepared out of a five days old mouse (for preparation see appendix A.4.5). The signal for muscle contraction is conducted from the axon terminal of a motor neuron to the muscle via the MJ. The muscle has a thickness of around 100 µm and was embedded in TDE. In order to analyze the density of synaptic vesicles dependent on the knockouts of APP and the related family members, STED recordings (10 x 10 µm) were taken from the preparations (Fig. 6.19 and 6.20). APP plays a major role in the etiopathology of *Alzheimer´s* disease (AD). The possible knockout-dependent vesicle density will not be further highlighted here. For imaging the MJs, it was necessary to focus approximately 20 µm into the tissue. Because of the high penetration depth it was very important to match the refractive index. Applying oil immersion lenses, the embedding in Mowiol did not match the refractive index satisfactorily to prevent a significant loss in resolution (Fig. 6.19a, b) in depth. This is on one hand caused by stray light filling up the zero of the depletion beam and on the other hand caused by spherical aberrations. Of course, the STED PSF is also limited by diffraction, and spherical aberrations smear out the PSF resulting in less steep edges of the zero and decreased resolution. Even a refractive index mismatch of 0.025 can lead to a remarkable decline of the resolution directly compared to the resolution gained in the TDE embedded sample (Fig. 6.19c, d). Parts of the improvement may also originate from better dye properties in TDE, but the performance of the dye directly on the coverslip is similar in both embedding media. Fig. 6.20 shows additional images of the MJ of different knockout mice. The distinct vesicular structures within the MJ are clearly resolved in the STED mode compared to the confocal images. The resolution is only limited by the samples extension in the optical direction and the laser power.

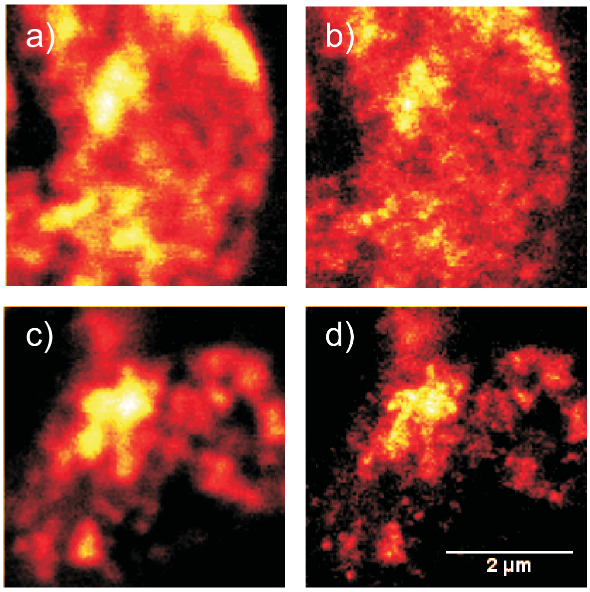

Fig. 6.19: The sample embedding in TDE ensures suitable optical properties for STED microscopy focusing deeply (20 µm) into tissue. The second row shows a confocal (**c**) and the corresponding STED image (**d**) of the synaptic vesicles in the MJ embedded in TDE and labelled with NK51. Features of 70 nm can be resolved. The first row (**a**) and (**b**) depicts the MJ of the muscle embedded in Mowiol. The STED image (**b**) appears more blurred out compared to the STED image of the TDE embedded sample (**d**). Both images are recorded in approximately the same depth of 20 µm.

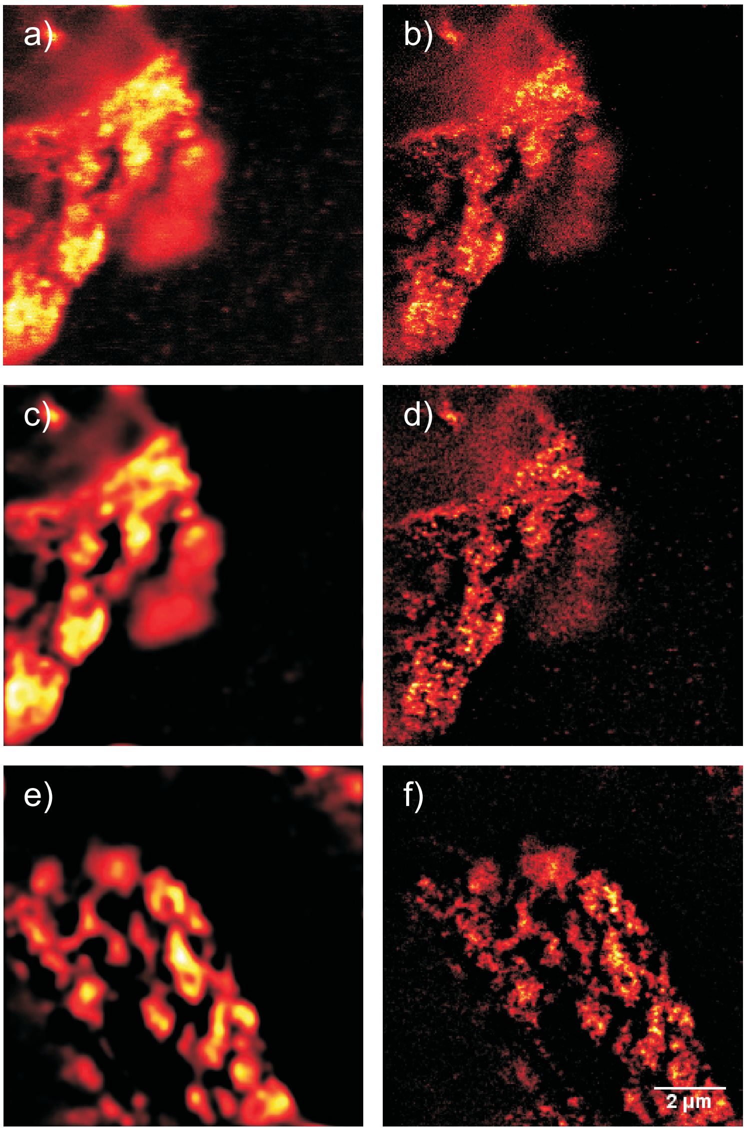

Fig. 6.20: Vesicular structures labelled with Atto565 can be resolved in MJs of 100 µm thick muscle preparations embedded in TDE. Left side confocal images ((**a**), (**c**), (**d**)), right side STED images ((**b**), (**d**), (**f**)). Row 2 and 3 are linear deconvolved. The first and the second row show vesicles in MJs prepared out of APP single knock out mice, the third row (**e**) and (**f**) depicts vesicles of double knockout mice.

The experiments are demonstrating that Atto565 and NK51 are both performing well in STED measurements of samples embedded in TDE for advanced optical properties. According to Tab. 6.1, Atto565 even shows a 40% higher fluorescence intensity in TDE compared to PBS. In combination with the dye Dy485XL high resolution two colour measurements are possible in TDE. This was shown impressively in measurements combining 4Pi and stimulated emission depletion to form a isotropic 3D focal spot (Schmidt et al., 2008). The dyes Atto647, Atto633, Atto590 and Dy480XL are also performing satisfactorily in TDE. Also Atto590 fluoresces brighter if embedded in TDE.

It could be shown, that matching the refractive index is crucial in confocal, and especially in 4Pi microscopy using high NA objective lenses or zero based optical high resolution microscopy deeply inside the sample. A refractive index mismatch causes spherical aberrations which counteracts the recording of high resolution information.

Chapter 7

Conclusion and outlook

This thesis addressed important obstacles in high resolution optical techniques, namely photobleaching, dark state transitions, and phototoxicity. A higher resolution calls for a more precise scanning of the object i.e. a larger pixel number, since the PSF as a probe decreases in size. A higher pixel number is connected to a higher light dose affecting the sample if the dwell time is kept constant. The high resolution approaches based on stochastical read-out (STORM, PALM, GSDIM, dSTORM, PAINT) require high photon counts to gather the coordinates of the single molecules accurately. If the molecule bleaches to fast, the localization accuracy is poor ($\sim\sqrt{N}$). For targeted read-out (STED, GSD, ESA), high signal suppression intensities have to be applied to separate the signals. However, high signal suppression intensities enable additional photobleaching pathways. In either case, photobleaching hinders high resolution imaging because it limits the maximal count rate or the maximal signal suppression intensities in zero based high resolution techniques. All possibilities have to be exploited to tackle photobleaching or to increase the number of detected photons, especially for experiments relying on image series such as 3D imaging, multicolour imaging, or recordings of dynamical processes. Biology, chemistry and physics are providing approaches to reduce the photobleaching. In this thesis, different strategies to prevent photobleaching, dark state transitions, and phototoxicity have been introduced.

The application of different fluorophores and laser lines calls for a setup, which is characterized by a high flexibility. The development of new fluorescent dyes is a highly active field and the ability to adopt fluorophores featuring advanced photostability (Mn-QD) as well as conditions helping to prevent photobleaching (RESCue) are basic requirements for a reliable and efficient optical setup. To apply a variety of different fluorophores or laser lines, many parts of the zero based subdiffraction microscope should ideally be tunable regarding the wavelength: clean up filters, the phase filter, the dichroic mirrors and the emission filter. A tunable solution to all these parts with their fixed properties is described in this thesis.

The multitude of laser lines provided by the Ar-Kr-laser can be perfectly exploited by the quadruple AOTF arrangement serving as a tunable beam splitter. Additionally, it is part of an adaptive filter system in combination with a prism based spectrometer. The adaptive filter system can be set as a notch or bandpass filter and can be adapted for every dye to maximally exploit the emission spectrum of a fluorophore. This can make thin film interference filters with their fixed properties redundant and may help to reduce the excitation intensity and therefore the photobleaching. Especially if an intense signal suppression beam is used for subdiffraction imaging with a wavelength located within the emission spectrum (STED), the filtering premises become severe. The signal and the background-levels of the adaptive and the thin film interference filters are comparable. One drawback of the adaptive filter system is the elaborate alignment procedure. To circumvent this, important parts like the plates, strip and mirrors can be motorized, and the whole procedure including the AOTF adjustment can be automated. The adaptive filter system will be applied to multicolour measurements without the usage of thin film interference filters in the future.

A new tunable phase plate principle was characterized, which is based on two identical adjacent optical flats, which are slightly tilted in respect to each other. By turning the whole optical flat arrangement every wavelength can be matched to feature a $\lambda/2$ phase step in one half of the beam relative to the other due to dispersion. This leads to a zero line PSF after focusing. Concomitant with that results an interesting simplification. Both, the excitation and the signal suppression beam can be provided by the same laser without the need for alignment of the two laser beam foci. By turning the two flats, the PSFs can be tuned to match different sets of excitation and signal suppression beam wavelengths provided by the Ar-Kr-laser in the cw mode. This approach was applied to resolve Nile red beads in one dimension. The next step is to provide a resolution enhancement in x and y direction by installing a second set of optical flats passed by the crossed polarization. This offers a very convenient way of subdiffraction imaging without the need for alignment of the foci or time delays between the excitation and signal suppression beam.

The quadruple AOTF arrangement enables the complete control of sample exposure, which is a basic requirement for the reduction of excitation and signal suppression cycles (RESCue) in zero based high resolution methods using metastable “off” states. The photobleaching in zero based high resolution techniques was decreased by a factor of about four applying the lower threshold (lTh). A better resolution opens up the possibility for a more accurate exposure of the sample minimizing the dyes excitation and signal suppression cycle numbers. If the resolution enhancement is based on long-lived or stable “off” states, phototoxicity can be reduced due to the diminishment of the light dose on cells. The measurements of a Nile red beads sample demonstrate impressively that the RESCue mode preserves the fluorescence by 20% more than the confocal mode with the aid of the high resolution information. The impact on relevant fixed biological samples is analyzed concerning the APP labelled neurons and GFAP labelled glial cells. RESCue opens up new options. It enables the 3D measurement of lamina labelled neuroblastoma cells. It reduces the light dose without giving up localization capability or imaging speed and therefore the number of switching cycles which leads to photobleaching and dark state population in all zero based high resolution ensemble methods. Anti-bleaching agents, which are interfering with life cell imaging can be avoided.

The crucial point of RESCue is to locate the presence of an object by a feedback with the detection. Coincident photons on two detectors would allow a fast decision on the presence of an object not being prone to a higher background. An object of interest is labelled with several dyes making coincidence on the detector probable.

The major impact of RESCue lies in enabling zero based high resolution measurements that are connected to higher photobleaching such as 3D STED measurements, application of coumarin derivatives in biological samples, STED measurements in the cw mode, multicolour STED measurements and fluorescent proteins in high resolution microscopy. In the STED case the reduced bleaching in standard applications can be reinvested in higher intensities and therefore higher resolution. The RESOLFT techniques should gain a reduction of phototoxicity.

But most importantly, the high resolution live cell microscopy based on targeted read-out should benefit from the RESCue modality because the examination of dynamical processes within the cells calls for repeated scans. Here the impact of photobleaching of the fluorescent dyes is most crucial as well as the phototoxicity caused by high light doses eventually leading to artefacts and cell death. However, this can be minimized by applying RESCue.

Another strategy to circumvent photobleaching related problems is the screening for new photostable fluorophores or alternative “on” and “off” states which can be controlled under milder conditions. Quantum dots feature an outstanding photostability. Reversible and wavelength selective optical modulation of fluorescence from Mn^{2+}-doped ZnSe quantum dots was demonstrated. This process relies on excited-state absorption (ESA) and its direct control of quantum dot fluorescence by light. Experiments demonstrate that all-optical switching efficiencies above 90% can be achieved using continuous-wave lasers source operating near 1 mW, a hundred times less intense compared to STED intensities. The ability to invoke the fluorescence modulation using a continuous-wave radiation, as well the advanced on-off photostability afforded by quantum nanocrystals, opens new avenues of research and application of optically activated quantum dots. As a primary example, Mn-QDs can be implemented for nanoscale imaging. This underscores the relevance of these photoswitchable QDs to contemporary nanoscopy as well as to other future applications, such as biological assays that necessitate the stability afforded by quantum dots and the direct control of their fluorescence capability by light. One major drawback of the Mn doped QDs is their long luminescence lifetime (90 µs) resulting in long data acquisition times.

The ruthenium complex $[Ru(bPy)_2(dcsubpy)][PF_6]_2$ exhibit fluorescence lifetimes dependent on the chemical surrounding around 250 ns to 500 ns and is characterized as a fluorophore to measure rotational motions of proteins via the anisotropy of the emitted light when the sample is excited with polarized light (Terpetschnik et al., 1995). This metal-ligand complex display emission from charge-transfer states in fluid solutions with a reasonable quantum yield (Demas et al., 1977). The coupling of these complexes to a system including a (valence and) conduction band may enable ESA RESOLFT experiments with these complexes opening up the lifetime range of few 100 ns to high resolution microscopy. This would be desirable since I_{sat} is inversely proportional to both the fluorescence lifetime of the fluorophore and its cross-section for excited state absorption.

The optical properties of the “last lens”, namely the sample embedding and the immersion system are crucial in the aim to provide an optimal focused PSF. A PSF, which is blurred out due to refractive index mismatches decreases the signal-to-noise ratio significantly. To compensate for that, higher excitation intensities have to be applied leading to pronounced photobleaching. The new mounting medium TDE is suitable for high resolution imaging of fixed specimens using objective lenses with the highest angles available. The refractive index in the sample can be adjusted from 1.333 (water) to 1.521 (beyond that of immersion oil) by adjusting the concentration of TDE to the required value. Unlike glycerol based mounting media, TDE allows to employ high angle oil immersion lenses of > 68° semiaperture angle without compromising image formation by refractive index induced spherical aberration. The benefits are deeper sample penetration, an increase in the image brightness, and better resolution. TDE may also be used to clear tissue prior to light sheet microscopical measurements making the clearance with hydrophobic BABB redundant.

A further important benefit is the improved spatial invariance of the effective PSF of the conventional or confocal microscope which is particularly important for increasing the resolution by image deconvolution (Holmes et al., 1995). Since the coherent use of opposing high angle spherical wavefronts is the essential physical ingredient in 4Pi and I^{5}M microscopy, index matching by TDE to substantially advance the optical performance of these axially superresolving techniques is recommended. In STED microscopy, the zero gets filled up by scattered light when focusing deep into unmatched tissue. The concomitant broadening of the PSF due to spherical aberrations counteracts subdiffraction imaging. Refractive index matching of thick samples is therefore mandatory for high resolution imaging. A major drawback is the destabilisation of GFP in TDE concentrations above 80%. Since the amount of water is crucial, a solution to this problem can be provided by an alternative mounting medium with a significantly higher refractive index compared to TDE. The concentration of water needed to match the desired refractive index of 1.518 would be higher, therefore enabling GFP embeddings with matched refractive index. Derivatives of TDE are among highly promising water soluble alternatives for the sample embedding.

In the past, TDE was applied as an antioxidant in amino acid analytics. Embedding the sample in TDE introduces a reductive agent in a high concentration and may recover the dye from reactive radical cations or quench reactive oxygen species.

In the future, further strategies to attack problems caused by photobleaching will be investigated because of their growing importance in high resolution imaging. One possibility to deal with photobleaching in high resolution optical microscopy is to ensure a huge label density on the structure of interest. The amino- or thiol-groups of fixed cellular structures can be marked directly with fluorophore-NHS-esters or maleimides respectively. This labelling procedure is not specific, but the desired structure can be marked additionally by a subsequent specific immuno-labelling process (already tested). The advantage besides a high label density is the fact, that the structures are not “blown up” by primary/secondary-antibody conjugates, which becomes a resolution limiting factor in far field nanoscopy (Heilemann et al., 2008). Information about structures in the proximity of the desired, additionally labelled structure are also gained, similar to EM studies. If the labelling is to dense and background from out of focus regions is hindering a sufficient signal-to-noise ratio, sections can be made.

A specific “direct” labelling may be achieved by blocking the amino- or thiol-groups of the desired structure with antibodies. All the other groups, which are not blocked by antibodies and therefore accessible are afterwards labelled by a non fluorescent molecule via reaction with the corresponding NHS-ester and maleimide. After removing of the bound antibody by lowering the pH value for example, the remaining and now accessible amino- and thiol-groups can be labelled directly with fluorophores.

To achieve highest resolutions possible, or if a third (or even fourth) dimension have to be considered in terms of time, z-axis, colour, so that repetitive scans and higher light doses are necessary, photobleaching, phototoxicity and dark state transitions have to be prevented. The combination of photostable dyes, RESCue, T-REX and chemical anti-fades can be the enabling factor to accomplish such measurements. The chemical and physical anti-bleaching methods presented here are therefore of vital importance.

Bibliography

Abbe, E. (1884) Note on the proper definition of the amplifying power of a lens or a lens- system. *J Royal Microsc Soc.* **4**:348-351

Abbe, E. (1873) Beiträge zur Theorie des Mikroskops und der mikroskopischen Wahrnehmung. *Arch f Mikroskop Anat.* **9**:413-420

Akerman, B. & Tuite, E. (1996) Single- and double-strand photocleavage of DNA by YO, YOYO and TOTO. *Nucleic Acids Res.* **24**(6):1080-1090

Alberts, B., Johnson, A., Lewis, J., Raff, M., Roberts, K. & Walter, P. (2002) Molecular Biology of the Cell. *Garland Science*

Anbar, M. & Hart, E. (1964) The Reactivity of Aromatic Compounds toward Hydrated Electrons. *J Am Chem Soc.* **6**:5633-5637

Ando, R., Mizuno, H. & Miyawaki, A. (2004) Regulated fast nucleocytoplasmic shuttling observed by reversible protein highlighting. *Science* **306**(5700):1370-1373

Aristov, A. (1994) Dependence of the activation energy of rhodamine 6G phototransformation into an irreversible photoproduct on the excitation wavelength. *Opt Spectrosc.* **77:**856-857

Back, S., Haas, P., Tschäpe, J.-A., Gruebl, T., Kirsch, J., Müller, U., Beyreuther, K. & Kins, S. (2007) beta-amyloid precursor protein can be transported independent of any sorting signal to the axonal and dendritic compartment. *J Neurosci Res.* **85**(12):2580-2590

Bates, M., Huang, B., Dempsey, G.T. & Zhuang, X. (2007) Multicolor super-resolution imaging with photo-switchable fluorescent probes. *Science* **317**(5845):1749-1753

Benson, D.M., Bryan, J., Plant, A.L., Gotto, A.M. & Smith, L.C. (1985) Digital imaging fluorescence microscopy: spatial heterogeneity of photobleaching rate constants in individual cells. *J Cell Biol.*, **100**(4):1309-1323

Bernas, T., Zarebski, M., Cook, R.R., Dobrucki, J.W. & Cook, P.R. (2004) Minimizing photobleaching during confocal microscopy of fluorescent probes bound to chromatin: role of anoxia and photon flux. *J Microsc.* **215**(Pt 3):281-296

Betzig, E. (1995) Proposed method for molecular optical imaging. *Opt Lett.* **20**:237-239

Betzig, E., Patterson, G.H., Sougrat, R., Lindwasser, O.W., Olenych, S., Bonifacino, J.S., Davidson, M.W., Lippincott-Schwartz, J. & Hess, H.F. (2006) Imaging intracellular fluorescent proteins at nanometer resolution. *Science* **313**(5793):1642-1645

Bhargava, R.N., Gallagher, D., Hong, X. & Nurmikko A. (1994) Optical properties of manganese-doped nanocrystals of ZnS. *Phys Rev Lett.* **72**(3):416-419

Born, M. & Wolf, E. (1999) Principles of Optics. *Cambridge University Press*

Bossi, M., Belov, V., Polyakova, S. & Hell, S.W. (2006) Reversible red fluorescent molecular switches. *Angew Chem Int Ed Engl.* **45**(44):7462-7465

Bretschneider, S., Eggeling, C. & Hell, S.W. (2007) Breaking the diffraction barrier in fluorescence microscopy by optical shelving. *Phys Rev Lett.* **98**(21):218103

Chalfie, M., Tu, Y., Euskirchen, G., Ward, W.W. & Prasher, D.C. (1994) Green fluorescent protein as a marker for gene expression. *Science* **263**(5148):802-805

Clausen, R. & Petermann, K. (1998) Mn+as a potential solid-state laser ion. *IEEE J Quantum Elect.* **24**(6):1114-1117

Coons, A.H., Creech, H.J., Jones, R.N. & Berliner, E. (1942) The Demonstration of Pneumococcal Antigen in Tissues by the Use of Fluorescent Antibody. *J Immunol.* **45**:159-170

Dahan, M., Laurence, T., Pinaud, F., Chemla, D.S., Alivisatos, A.P., Sauer, M. & Weiss, S. (2001) Time-gated biological imaging by use of colloidal quantum dots. *Opt Lett.* **26**(11):825-827

Dahan, M., Lévi, S., Luccardini, C., Rostaing, P., Riveau, B. & Triller, A. (2003) Diffusion dynamics of glycine receptors revealed by single-quantum dot tracking. *Science* **302**(5644):442-445

Demas, J.N., Harris, E. & McBride, R. (1977) Energy transfer from luminescent transition metal complexes to oxygen. *J Am Chem Soc.* **99**:3547-3551

Denk, W., Delaney, K.R., Gelperin, A., Kleinfeld, D., Strowbridge, B.W., Tank, D.W. & Yuste, R. (1994) Anatomical and functional imaging of neurons using 2-photon laser scanning microscopy. *J Neurosci Methods.* **54**(2):151-162

Denk, W., Strickler, J.H. & Webb, W.W. (1990) Two-photon laser scanning fluorescence microscopy. *Science* **248**(4951):73-76

Deschenes, L.A. & Bout, D.A.V. (2002) Single molecule photobleaching: increasing photon yield and survival time through suppression of two-step photolysis. *Chem Phys Lett.* **365**:387-395

Dittrich, P. & Schwille, P. (2001) Photobleaching and stabilization of fluorophores used for single-molecule analysis with one- and two-photon excitation. *Appl Phys B* **73**:829-837

Dodt, H.-U., Leischner, U., Schierloh, A., Jährling, N., Mauch, C.P., Deininger, K., Deussing, J.M., Eder, M., Zieglgänsberger, W. & Becker, K. (2007) Ultramicroscopy: three-dimensional visualization of neuronal networks in the whole mouse brain. *Nat Methods* **4**(4):331-336

Donnert, G., Keller, J., Medda, R., Andrei, M.A., Rizzoli, S.O., Lührmann, R., Jahn, R., Eggeling, C. & Hell, S.W. (2006) Macromolecular-scale resolution in biological fluorescence microscopy. *Proc Natl Acad Sci USA* **103**(31):11440-11445

Donnert, G., Keller, J., Wurm, C.A., Rizzoli, S.O., Westphal, V., Schönle, A., Jahn, R., Jakobs, S., Eggeling, C. & Hell, S.W. (2007) Two-color far-field fluorescence nanoscopy. *Biophys J.* **92**(8):L67-L69

Dotti, C.G. & Simons, K. (1990) Polarized sorting of viral glycoproteins to the axon and dendrites of hippocampal neurons in culture. *Cell* **62**(1):63-72

Dreyhsig, J., Stutenbäumer, U., Gumlich, H.-E. & Allen, J. (1990) Excited state absorption (ESA) of Mn in ZnS and ZnSe. *J Cryst Growth* **101**:443

Dyba, M. & Hell, S.W. (2002) Focal spots of size lambda/23 open up far-field fluorescence microscopy at 33 nm axial resolution. *Phys Rev Lett.* **88**(16):163901

Dyba, M., Keller, J. & Hell, S. (2005) Phase filter enhanced STED-4Pi fluorescence microscopy: theory and experiment. *New J Phys.* **7**:134

Eggeling, C., Brand, L. & Seidel, C. (1997) Laser-induced fluorescence of coumarin derivatives in aqueous solution: Photochemical aspects for single molecule detection. *Bioimaging* **5**:105-115

Eggeling, C., Widengren, J., Rigler, R. & Seidel, C. (1998) Photobleaching of fluorescent dyes under conditions used for single molecule detection: Evidence of two step photolysis. *Anal Chem.* **70**:2651-2659

Egner, A., Geisler, C., von Middendorff, C., Bock, H., Wenzel, D., Medda, R., Andresen, M., Stiel, A.C., Jakobs, S., Eggeling, C., Schönle, A. & Hell, S.W. (2007) Fluorescence nanoscopy in whole cells by asynchronous localization of photoswitching emitters. *Biophys J.* **93**(9):3285-3290

Egner, A. & Hell, S.W. (2005) Fluorescence microscopy with super-resolved optical sections. *Trends Cell Biol.* **15**(4):207-215

Egner, A., M.S. & Hell, S.W. (1998) Refractive index mismatch induced intensity and phase variations in fluorescence confocal, multiphoton and 4Pi-microscopy. *Opt Commun.* **153**:211-217

Ehlert, A., Dreyhsig, J., Gumlich, H.-E. & Allen, J. (1994) Excited state absorption of ZnSe doped with cobalt. *J Lumin.* **60+61**:21-25

Encinas, M., Iglesias, M., Liu, Y., Wang, H., Muhaisen, A., Ceña, V., Gallego, C. & Comella, J.X. (2000) Sequential treatment of SH-SY5Y cells with retinoic acid and brain-derived neurotrophic factor gives rise to fully differentiated, neurotrophic factor-dependent, human neuron-like cells. *J Neurochem.***75**(3):991-1003

Fu, X.D. & Maniatis, T. (1990) Factor required for mammalian spliceosome assembly is localized to discrete regions in the nucleus. *Nature* **343**(6257):437-441

Fölling, J., Bossi, M., Bock, H., Medda, R., Wurm, C.A., Hein, B., Jakobs, S., Eggeling, C. & Hell, S.W. (2008) Fluorescence nanoscopy by ground-state depletion and single-molecule return. *Nat Methods.* **5**(11):943-945

Gu, M. (1999) Advanced Optical Imaging Theory. *Springer-Verlag*

Gugel, H., Bewersdorf, J., Jakobs, S., Engelhardt, J., Storz, R. & Hell, S.W. (2004) Cooperative 4Pi excitation and detection yields sevenfold sharper optical sections in live-cell microscopy. *Biophys J.* **87**(6):4146-4152

Gustafsson, M.G., Agard, D.A. & Sedat, J.W. (1999) I5M: 3D widefield light microscopy with better than 100 nm axial resolution. *J Microsc.* **195**(Pt 1):10-16

Gustafsson, M.G.L. (2005) Nonlinear structured-illumination microscopy: wide-field fluorescence imaging with theoretically unlimited resolution. *Proc Natl Acad Sci USA* **102**(37):13081-13086

Han, M., Gao, X., Su, J.Z. & Nie, S. (2001) Quantum-dot-tagged microbeads for multiplexed optical coding of biomolecules. *Nat Biotechnol.* **19**(7):631-635

Harada, Y., Sakurada, K., Aoki, T., Thomas, D.D. & Yanagida, T. (1990) Mechanochemical coupling in actomyosin energy transduction studied by in vitro movement assay. *J Mol Biol.* **216**(1):49-68

Harke, B., Keller, J., Ullal, C.K., Westphal, V., Schönle, A. & Hell, S.W. (2008) Resolution scaling in STED microscopy. *Opt Express* **16**(6):4154-4162

Hefetz, Y., Goltsos, W., Nurmikko, A., Kolodziejski, L. & Gunshor, R. (1986) Exciton formation and energy exchange with d-electron states in ZnSe/(Zn,Mn)Se multiple quantum wells. *Appl Phys Lett.* **48**:372

Heilemann, M., van de Linde, S., Schüttpelz, M., Kasper, R., Seefeldt, B., Mukherjee, A., Tinnefeld, P. & Sauer, M. (2008) Subdiffraction-resolution fluorescence imaging with conventional fluorescent probes. *Angew Chem Int Ed Engl.* **47**(33):6172-6176

Heilemann, M., Margeat, E., Kasper, R., Sauer, M. & Tinnefeld, P. (2005) Carbocyanine dyes as efficient reversible single-molecule optical switch. *J Am Chem Soc.* **127**(11):3801-3806

Hein, B., Willig, K.I. & Hell, S.W. (2008) Stimulated emission depletion (STED) nanoscopy of a fluorescent protein-labeled organelle inside a living cell. *Proc Natl Acad Sci USA* **105**(38):14271-14276

Heintzmann, R., Jovin, T.M. & Cremer, C. (2002) Saturated patterned excitation microscopy--a concept for optical resolution improvement. *J Opt Soc Am A Opt Image Sci Vis.* **19**(8):1599-1609

Hell, S. (2004) Strategy for far-field optical imaging and writing without diffraction limit. *Phys Lett A* **326**:140-145

Hell, S., Jakobs, S. & Kastrup, L. (2003) Imaging and writing at the nanoscale with focused visible light through saturable optical transitions. *Appl Phys A* **7**:859-860

Hell, S. & Kroug, M. (1995) Ground-state depletion fluorescence microscopy, a concept for breaking the diffraction resolution limit. *Appl Phys B* **60**:495-497

Hell, S., Reiner, G., Cremer, C. & Stelzer, E. (1993) Aberrations in confocal fluorescence microscopy induced by mismatches in refractive index. *J Microsc.* **169**:391-405

Hell, S. & Wichmann, J. (1994) Breaking the diffraction resolution limit by stimulated emission: stimulated emission depletion microscopy. *Opt Lett.* **19**:780-782

Hell, S.W. (2007) Far-field optical nanoscopy. *Science* **316**(5828):1153-1158

Hell, S.W. (2003) Toward fluorescence nanoscopy. *Nat Biotechnol.* **21**(11):1347-1355

Hell, S.W. (1994) Improvement of lateral resolution in far-field light microscopy using two-photon excitation with offset beams. *Opt Commun.* **106**:19-24

Hell, S.W., Dyba, M. & Jakobs, S. (2004) Concepts for nanoscale resolution in fluorescence microscopy. *Curr Opin Neurobiol.* **14**(5):599-609

Hink, M.A., Bisselin, T. & Visser, A.J.W.G. (2002) Imaging protein-protein interactions in living cells. *Plant Mol Biol.* **50**(6):871-883

Hirschfeld, T. (1976) Quantum efficiency independence of the time integrated emission from a fluorescent molecule. *Appl Opt.* **15**:3135–-3139

Hoebe, R.A., Oven, C.H.V., Gadella, T.W.J., Dhonukshe, P.B., Noorden, C.J.F.V. & Manders, E.M.M. (2007) Controlled light-exposure microscopy reduces photobleaching and phototoxicity in fluorescence live-cell imaging. *Nat Biotechnol.* **25**(2):249-253

Hofmann, M., Eggeling, C., Jakobs, S. & Hell, S.W. (2005) Breaking the diffraction barrier in fluorescence microscopy at low light intensities by using reversibly photoswitchable proteins. *Proc Natl Acad Sci USA* **102**(49):17565-17569

Hoogenboom, J.P., van Dijk, E.M.H.P., Hernando, J., van Hulst, N.F. & García-Parajó, M.F. (2005) Power-law-distributed dark states are the main pathway for photobleaching of single organic molecules. *Phys Rev Lett.* **95**(9):097401

Huang, B., Wang, W., Bates, M. & Zhuang, X. (2008) Three-dimensional super-resolution imaging by stochastic optical reconstruction microscopy. *Science* **319**(5864):810-813

Huh, Y.-M., wook Jun, Y., Song, H.-T., Kim, S., sil Choi, J., Lee, J.-H., Yoon, S., sup Kim, K., Shin, J.-S., Suh, J.-S. & Cheon, J. (2005) In vivo magnetic resonance detection of cancer by using multifunctional magnetic nanocrystals. *J Am Chem Soc.* **127**(35):12387-12391

Irvine, S.E., Staudt, T., Rittweger, E., Engelhardt, J. & Hell, S.W. (2008) Direct light-driven modulation of luminescence from Mn-doped ZnSe quantum dots. *Angew Chem Int Ed Engl.* **47**(14):2685-2688

Jacobsen, H., Hänninen, P. & Hell, S. (1994) Refractive-index-induced aberrations in two-photon confocal fluorescence microscopy. *J Microsc.* **176**:226-230

Jares-Erijman, E.A. & Jovin, T.M. (2003) FRET imaging. *Nat Biotechnol.* **21**(11):1387-1395

Jares-Erijman, E., Giordano, L., Spagnuolo, C., Lidke, K. & TM., T.J. (2005) Imaging quantum dots switched on and off by photochromic fluorescence resonance energy transfer (pcFRET). *Mol Cryst Liq Cryst.* **430**:257-265

Kastrup, L., Blom, H., Eggeling, C. & Hell, S.W. (2005) Fluorescence fluctuation spectroscopy in subdiffraction focal volumes. *Phys Rev Lett.* **94**(17):178104

Keller, J., Schönle, A. & Hell, S. (2007) Efficient fluorescence inhibition patterns for RESOLFT microscopy. *Opt. Express* **15**:3361-3371

Khoroshilova, E.V. & Nikogosyan, D.N. (1990) Photochemistry of uridine on high intensity laser UV irradiation. *J Photochem Photobiol B.* **5**(3-4):413-427

Klar, T.A., Engel, E. & Hell, S.W. (2001) Breaking Abbe's diffraction resolution limit in fluorescence microscopy with stimulated emission depletion beams of various shapes. *Phys Rev E Stat Nonlin Soft Matter Phys.* **64**(6 Pt 2):066613

Klar, T.A., Jakobs, S., Dyba, M., Egner, A. & Hell, S.W. (2000) Fluorescence microscopy with diffraction resolution barrier broken by stimulated emission. *Proc Natl Acad Sci USA* **97**(15):8206-8210

Klimov, V.I., Ivanov, S.A., Nanda, J., Achermann, M., Bezel, I., McGuire, J.A. & Piryatinski, A. (2007) Single-exciton optical gain in semiconductor nanocrystals. *Nature* **447**(7143):441-446

Korobov, V. & Chibisov, A. (1978) Primary processes in the photochemistry of rhodamine dyes. *J Photochem.* **9**:411-424

Kural, C., Kim, H., Syed, S., Goshima, G., Gelfand, V.I. & Selvin, P.R. (2005) Kinesin and dynein move a peroxisome in vivo: a tug-of-war or coordinated movement? *Science* **308**(5727):1469-1472

Kuroda, T., Ito, H., Minami, F. & Akinaga, H. (1997) Ultrafast energy transfer in manganese doped ZnSe. *J Lumin.* **72-74**:106-107

Lakowicz, J.R. (2006) Principles of fluorescence spectroscopy. *Springer*

Lamond, A.I. & Spector, D.L. (2003) Nuclear speckles: a model for nuclear organelles. *Nat Rev Mol Cell Biol.* **4**(8):605-612

Lang, M., Müller, T., Engelhardt, J. & Hell, S. (2007a) 4Pi microscopy of type A with 1-photon excitation in biological fluorescence imaging. *Opt Express* **15**:2459-2467

Lang, M., Staudt, T., Engelhardt, J. & Hell, S. (2008) 4Pi microscopy with negligible sidelobes. *New J Phys.* **10**:1-13

Lang, M.C., Engelhardt, J. & Hell, S.W. (2007b) 4Pi microscopy with linear fluorescence excitation. *Opt Lett.* **32**(3):259-261

Lawson, J.K. & Payne, S.A. (1993) Excited-state absorption of Eu2+-doped materials. *Phys Rev B Condens Matter* **47**(21):14003-14010

LeRosen, A.L. & Reid, C.E. (1952) An Investigation of Certain Solvent Effect in Absorption Spectra. *J Chem Phys.* **20**:233-236

Lewis, A., Isaacson, M., Harootunian, A. & Muray, A. (1984) Development of a 500 Å spatial resolution light microscope: I. light is efficiently transmitted through lambda/16 diameter apertures. *Ultramicroscopy* **13**:227-231

Lukyanov, K.A., Fradkov, A.F., Gurskaya, N.G., Matz, M.V., Labas, Y.A., Savitsky, A.P., Markelov, M.L., Zaraisky, A.G., Zhao, X., Fang, Y., Tan, W. & Lukyanov, S.A. (2000) Natural animal coloration can be determined by a nonfluorescent green fluorescent protein homolog. *J Biol Chem.* **275**(34):25879-25882

Martini, N., Bewersdorf, J. & Hell, S.W. (2002) A new high-aperture glycerol immersion objective lens and its application to 3D-fluorescence microscopy. *J Microsc.* **206**(Pt 2):146-151

Mattoussi, H., Radzilowski, L.H., Dabbousi, B.O. & Thomas, E.L. (1998) Electroluminescence from heterostructures of poly(phenylene vinylene) and inorganic CdSe nanocrystals. *J Appl Phys.* **83**:7965

Medintz, I.L., Trammell, S.A., Mattoussi, H. & Mauro, J.M. (2004) Reversible modulation of quantum dot photoluminescence using a protein- bound photochromic fluorescence resonance energy transfer acceptor. *J Am Chem Soc.* **126**(1):30-31

Menzel, R. & Thiel, E. (1998) Intersystem crossing rate constants of rhodamine dyes: influence of the amino-group substitution. *Chem Phys Lett.* **291**:237-243

Merkel, P.B. & Kearns, D.R. (1972) Radiationless decay of singlet molecular oxygen in solution. *J. Am. Chem. Soc.* **94**: 7244-7253

Michalet, X., Pinaud, F., Lacoste, T., Bruchez, M.D.M., Alivisatos, A. & Weiss, S. (2001) Properties of Fluorescent Semiconductor Nanocrystals and their Application to Biological Labeling. *Single Mol.* **3**:261-267

Michalet, X., Pinaud, F.F., Bentolila, L.A., Tsay, J.M., Doose, S., Li, J.J., Sundaresan, G., Wu, A.M., Gambhir, S.S. & Weiss, S. (2005) Quantum dots for live cells, in vivo imaging, and diagnostics. *Science* **307**(5709):538-544

Minsky, M. (1957) Microscopy Apparatus. U.S. Patent #3013467

Misteli, T. (2001) Protein dynamics: implications for nuclear architecture and gene expression. *Science* **291**(5505):843-847

Moore, S. & Stein, W. (1951) Chromatography of amino acids on sulfonated polystyrene resins. *J Biol Chem.* **192**(2):663-681

Müller, R. (1956) Zur Verbesserung der Phasenkontrast-Mikroskopie durch Verwendung von Medien optimaler Brechungsindices. *Mikroskopie* **11**:36-46

Nie, S., Chiu, D.T. & Zare, R.N. (1994) Probing individual molecules with confocal fluorescence microscopy. *Science* **266**(5187):1018-1021

van Oijen, A., Köhler, J., Schmidt, J., Müller, M. & Brakenhoff, G. (1999) Far-field Microscopy beyond the Diffraction limit. *J Opt Soc Am A* **16**:909

Ormö, M., Cubitt, A.B., Kallio, K., Gross, L.A., Tsien, R.Y. & Remington, S.J. (1996) Crystal structure of the Aequorea victoria green fluorescent protein. *Science* **273**(5280):1392-1395

Osborn, M., Franke, W.W. & Weber, K. (1977) Visualization of a system of filaments 7-10 nm thick in cultured cells of an epithelioid line (Pt K2) by immunofluorescence microscopy. *Proc Natl Acad Sci USA* **74**(6):2490-2494

Pavlopoulos, T.G. & Golich, D.J. (1988) Triplet extinction coefficients of some laser dyes I. *J Appl Phys.* **64**:521

Pawley, J.B. (2006) Handbook of Biological Confocal Microscopy. *Plenum Press*

Pendry, J.B. (2000) Negative refraction makes a perfect lens. *Phys Rev Lett.* **85**(18):3966-3969

Petermann, K., Clausen, R., Heumann, E. & Ledig, M. (1989) Time resolved excited state absorption of Mn2+. *Opt Commun.* **70**:483-486

Podolskiy, V.A. & Narimanov, E.E. (2005) Near-sighted superlens. *Opt Lett.* **30**(1):75-77

Pohl, D.W., Denk, W. & Lanz, M. (1984) Optical stethoscopy: Image recording with resolution lambda/20. *Appl Phys Lett.* **44**:651

Pradhan, N., Battaglia, D.M., Liu, Y. & Peng, X. (2007) Efficient, stable, small, and water-soluble doped ZnSe nanocrystal emitters as non-cadmium biomedical labels. *Nano Lett.* **7**(2):312-317

Rankin, B.R., Kellner, R.R., Hell, S.W. (2008) Stimulated-emission-depletion microscopy with a multicolour stimulated-Raman-scattering light source. *Opt Lett.* **33**(21):2491-2493

Reiss, P., Bleuse, J. & Pron, A. (2002) Highly Luminescent CdSe/ZnSe Core/Shell Nanocrystals of Low Size Dispersion. *Nano Lett.* **2**:781-784

Reuther, A., Nikogosyan, D. & Laubereau, A. (1996) Primary photochemical processes in thymine in concentrated aqueous solution studied by femtosecond UV spectroscopy. *J Phys Chem.* **100**:5570-5577

Richter, K., Nessling, M. & Lichter, P. (2007) Experimental evidence for the influence of molecular crowding on nuclear architecture. *J Cell Sci.* **120**(Pt 9):1673-1680

Rittweger, E., Rankin, B., Westphal, V. & Hell, S. (2007) Fluorescence depletion mechanisms in super-resolving STED microscopy. *Chem Phys Lett.* **442**:483-487

Rust, M.J., Bates, M. & Zhuang, X. (2006) Sub-diffraction-limit imaging by stochastic optical reconstruction microscopy (STORM). *Nat Methods* **3**(10):793-795

Sahlas, D.J., Milankov, K., Park, P.C. & Boni, U.D. (1993) Distribution of snRNPs, splicing factor SC-35 and actin in interphase nuclei: immunocytochemical evidence for differential distribution during changes in functional states. *J Cell Sci.* **105** (Pt 2):347-357

Santra, S., Yang, H., Holloway, P.H., Stanley, J.T. & Mericle, R.A. (2005) Synthesis of water-dispersible fluorescent, radio-opaque, and paramagnetic CdS:Mn/ZnS quantum dots: a multifunctional probe for bioimaging. *J Am Chem Soc.* **127**(6):1656-1657

Schmidt, R., Wurm, C.A., Jakobs, S., Engelhardt, J., Egner, A. & Hell, S.W. (2008) Spherical nanosized focal spot unravels the interior of cells. *Nat Methods* **5**(6):539-544

Schwentker, M.A., Bock, H., Hofmann, M., Jakobs, S., Bewersdorf, J., Eggeling, C. & Hell, S.W. (2007) Wide-field subdiffraction RESOLFT microscopy using fluorescent protein photoswitching. *Microsc Res Tech.* **70**(3):269-280

Schwille, P., Haupts, U., Maiti, S. & Webb, W.W. (1999) Molecular dynamics in living cells observed by fluorescence correlation spectroscopy with one- and two-photon excitation. *Biophys J.* **77**(4):2251-2265

Sharonov, A. & Hochstrasser, R.M. (2006) Wide-field subdiffraction imaging by accumulated binding of diffusing probes. *Proc Natl Acad Sci USA* **103**(50):18911-18916

Shroff, H., Galbraith, C.G., Galbraith, J.A. & Betzig, E. (2008) Live-cell photoactivated localization microscopy of nanoscale adhesion dynamics. *Nat Methods* **5**(5):417-423

Song, H. & Lee, S. (2007) Red light emitting solid state hybrid quantum dot–near-UV GaN LED devices. *Nanotechnology* **18:**255-259

Song, L., Varma, C.A., Verhoeven, J.W. & Tanke, H.J. (1996) Influence of the triplet excited state on the photobleaching kinetics of fluorescein in microscopy. *Biophys J.* **70**(6):2959-2968

Spector, D.L. (2001) Nuclear domains. *J Cell Sci.* **114**(Pt 16):2891-2893

Spector, D.L., Lark, G. & Huang, S. (1992) Differences in snRNP localization between transformed and nontransformed cells. *Mol Biol Cell.* **3**(5):555-569

Staudt, T., Engler, A., Harke, B., Engelhardt, J. & Hell, S.W. Reduction of excitation and signal suppression cycles (RESCue) in zero based high resolution optical microscopy. *in preparation*

Staudt, T., Lang, M.C., Medda, R., Engelhardt, J. & Hell, S.W. (2007) 2,2'-thiodiethanol: a new water soluble mounting medium for high resolution optical microscopy. *Microsc Res Tech.* **70**(1):1-9

Steinhauer, C., Forthmann, C., Vogelsang, J. & Tinnefeld, P. (2008) Superresolution microscopy on the basis of engineered dark States. *J Am Chem Soc.* **130**(50):16840-16841

Stöber, W., Fink, A., Bohn, E. (1968) Controlled growth of monosized silica spheres in the micron size range. *Journal of Colloid and Interface Science.* **26**:62-69

Sukhanova, A., Devy, J., Venteo, L., Kaplan, H., Artemyev, M., Oleinikov, V., Klinov, D., Pluot, M., Cohen, J.H.M. & Nabiev, I.(2004) Biocompatible fluorescent nanocrystals for immunolabeling of membrane proteins and cells. *Anal Biochem.* **324**(1):60-67

Terpetschnig, E., Szmacinski, H., Malak, H. & Lakowicz, J.R. (1995) Metal-ligand complexes as a new class of long-lived fluorophores for protein hydrodynamics. *Biophys J.* **68**(1):342-350

Thiry, M. (1995) The interchromatin granules. *Histol Histopathol.* **10**(4):1035-1045

Tikhonov, A. & Arsenin, V. (1977) Solutions of Ill-Posed Problems. *Halsted Press*

Vogelsang, J., Kasper, R., Steinhauer, C., Person, B., Heilemann, M., Sauer, M. & Tinnefeld, P. (2008) A reducing and oxidizing system minimizes photobleaching and blinking of fluorescent dyes. *Angew Chem Int Ed Engl.* **47**(29):5465-5469

Weast, R. (1974) Handbook of Chemistry and Physics. *CRC Press*

Weston, K.D., Dyck, M., Tinnefeld, P., Müller, C., Herten, D.P. & Sauer, M. (2002) Measuring the number of independent emitters in single-molecule fluorescence images and trajectories using coincident photons. *Anal Chem.* **74**(20):5342-5349

Westphal, V. & Hell, S. (2005) Nanoscale Resolution in the Focal Plane of an Optical Microscope. *Phys Rev Lett.* **94**:143903

Westphal, V., Rizzoli, S.O., Lauterbach, M.A., Kamin, D., Jahn, R. & Hell, S.W. (2008) Video-rate far-field optical nanoscopy dissects synaptic vesicle movement. *Science* **320**(5873):246-249

Widengren, J., Chmyrov, A., Eggeling, C., Löfdahl, P.-A. & Seidel, C.A.M. (2007) Strategies to improve photostabilities in ultrasensitive fluorescence spectroscopy. *J Phys Chem A* **111**(3):429-440

Widengren, J. & Schwille, P. (2000) Characterization of photoinduced isomerization and back-isomerization of cyaninie dye Cy5 by fluorescence correlation spectroscopy. *J Phys Chem A* **104**:6416-6428

Wildanger, D., Rittweger, E., Kastrup, L. & Hell, S.W. (2008) STED microscopy with a supercontinuum laser source. *Opt Express* **16**(13):9614-9621

Willig, K.I., Harke, B., Medda, R. & Hell, S.W. (2007) STED microscopy with continuous wave beams. *Nat Methods* **4**(11):915-918

Wilson, T. (1990) Confocal Microscopy. *Academic Press Ltd*

Yoshikawa, Y., Hizume, K., Oda, Y., Takeyasu, K., Araki, S. & Yoshikawa, K. (2006) Protective effect of vitamin C against double-strand breaks in reconstituted chromatin visualized by single-molecule observation. *Biophys J.* **90**(3):993-999

Zhu, L., Zhu, M.-Q., Hurst, J.K. & Li, A.D.Q. (2005) Light-controlled molecular switches modulate nanocrystal fluorescence. *J Am Chem Soc.* **127**(25):8968-8970

Appendix

A.1 Adaptive filtering and Simple STED

A.1.1 Fluorescent bead sample preparation

Nile red filled polystyrene micro spheres (specified diameter, 21 nm; 2% solids in distilled water; Molecular Probes) were sowed on poly-L-lysine (PLL) (Sigma, Germany) coated coverslips and mounted in DABCO containing Mowiol (Sigma, Germany) to avoid molecular diffusion.

A.1.2 SupT1 cell preparation

A total of $5*10^{-5}$ SupT1 cells were plated on a coverslip precoated with 0.1% polyethylene imine (PEI) in water. After 60 min of incubation at 37°C and 5% CO_2, cells were fixed with 4% paraformaldehyde (PFA) in PBS. The cells were washed with PBS and subsequently stained with Atto565-phalloidin conjugates at the appropriate dilution for 40 minutes at room temperature. After washing the cells with PBS, they were mounted in Mowiol containing DABCO.

A.2 Reduction of excitation and signal suppression cycles (RESCue) in zero based high resolution optical microscopy

A.2.1 Cell culture and immunocytochemistry

Glioblastoma: GFAP; microtubuli

For immunocytochemistry, the U373 glioblastoma cells were seeded on standard glass coverslips to a confluency of 50-80% and permeabilized with cold methanol (-20ºC) for 4-6 min. The cells were subsequently washed in PBS with 1% bovine serum albumin (BSA) (blocking buffer) and incubated with primary antibodies (anti GFAP mouse IgG, Sigma, Germany; anti α-Tubulin rabbit IgG, 1 µg/ml, Abcam, Cambridge, UK;). After 1 h of incubation, the cells were washed with blocking buffer for 10 min and incubated with secondary antibodies (Atto565 goat anti-mouse IgG; Atto390 goat anti-mouse IgG) for 1 h after the protocol from Molecular Probes, Carlsbad. For imaging, the cells were mounted in Mowiol (Sigma, Germany) containing DABCO (Sigma, Germany) as an antioxidant.

APP: primary mouse neurons (DIV8)

Embryos (E14) from wt (C57BL/6NCrl; Charles River) mice were separated and dissociated mixed cortical neuron cultures were prepared as described previously (Dotti et al., 1990). Neurons were grown on poly-L-lysine-coated 15 mm coverslips (Marienfeld, Germany) in serum-free Neurobasal Media (Gibco, Germany) with B-27 supplement (Gibco, Germany), 25 µM glutamate (Sigma, Germany), and 0.5 mM glutamine (Sigma, Germany). For immunocytochemical analysis, primary neurons were fixed with 4% PFA (Sigma, Germany) and permeabilized 10 min with 0.1% NP-40/Nonidet (Fluka, Germany) in PBS. Cells were incubated with primary antibodies (monoclonal anti-APP-antibody 4G8 (Chemicon, CA) diluted in 5% goat serum in PBS and anti-synaptophysin-antibody) at 4°C overnight, washed with PBS, incubated with secondary antibodies (Atto565 goat anti-mouse IgG, 10 µg/ml, Dy485XL goat anti-rabbit IgG), and embedded in Mowiol (Sigma, Germany) on glass coverslips.

Neuroblastoma: Lamin

The SH-SY5Y neuroblastoma cell line was grown as described previously (Encinas et al., 2005). Cells were seeded on standard glass coverslips to a confluency of about 80%. For immunostaining of the nuclear lamina, the cells were fixed with 3.7% PFA for 15 min followed by a 5 min-treatment with Triton X-100. Before the incubation with the primary antibody, the cells were blocked in 1% BSA in PBS for 5 min. Anti-lamin B1 rabbit IgG (Abcam, Cambridge, UK) was used as primary antibody, anti-rabbit conjugated Atto647N IgG as secondary antibody respectively. Both antibodies were diluted in blocking buffer. Postfixation was carried out with 3.7% PFA for 10 min. Cells were mounted in Mowiol.

A.2.2 Fluorescent bead sample preparation

Nile red filled polystyrene micro spheres (specified diameter, 21 nm; 2% solids in distilled water; Molecular Probes) or self made silica nanoparticles with a mean diameter of approximately 25 nm were sowed on poly-L-lysine (PLL) (Sigma, Germany) coated coverslips and mounted in DABCO containing Mowiol (Sigma, Germany) to avoid molecular diffusion and photobleaching.

Silica nanoparticles doped with the fluorescent dye Atto425 were prepared according to a modification of the Stöber method (Stöber et al., 1968). 0.5 mg of Atto425-NHS and 3 µl (about 9 equivalents) of (3-aminopropyl)triethoxysilane were dissolved in 300 µl ethanol at room temperature. After 10 hours of stirring, the mixture was diluted with ethanol, and ammonium hydroxide (28% in water) was added to a final concentration of 0.45 M. Then 110 µl tetraethyl orthosilicate (TEOS) were added, yielding a molar ratio TOES/dye of approximately 500. The sample was then stirred overnight at room temperature. The reaction was quenched by diluting the mixture with two parts of solvent, and purified by three centrifugation/resuspension cycles.

A.3 Direct light-driven modulation of luminescence from Mn-doped ZnSe quantum dots: a new contrast

A.3.1 Sample preparation

Fixed cluster samples of the Mn-QDs were prepared from aqueous solution (~15 µM) obtained directly from NN-Labs (Fayetteville, AR). Approximately 25 µL of undiluted solution was placed on a cover slip which was sealed against a microscope slide. After ~24 hr, small (20-300 nm) clusters formed on the cover slip, which were visible in a standard epi-fluorescence microscope. The most probable explanation for clustering lies in the nature of the stabilization of the quantum dots in polar solvents. Due to weak covalent bonding between the Mn-QDs and the mercaptopropionic acid stabilization agent, a significant fraction of the nanocrystals can lose their ligands. In the absence of the electrostatic repulsion provided by the ligands, nanocrystal solubility is lost and results in aggregation and immobilization on the cover slip surface.

A.4 2,2´-Thiodiethanol (TDE) as an embedding medium

A.4.1 Medium

For preparation, TDE (2,2’-Thiodiethanol) (CAS 111-48-8, highest purity, #88559 Sigma-Aldrich) is adjusted to a pH of 7.5 with 1.2 M hydrochloric acid. 970 µl TDE mixed with 30 µl PBS1x (or other aqueous buffer solution) give 1 ml mounting medium with a refractive index of 1.515 and a pH value of 7.5±1.

A.4.2 Buffers

The water amount in the final solution contains PBS buffer which consists of 137 mM NaCl, 2.68 mM KCl, 8 mM Na_2HPO_4, and 1.47 mM KH_2PO_4; pH=7.5.

A.4.3 PtK2 cell culture and immunocytochemistry

PtK2 cells were grown as described previously (Osborn et al., 1977). For immunocytochemistry, the cells were seeded on standard glass coverslips to a confluency of 50-80% and permeabilised with cold methanol (-20ºC) for 4-6 min. The cells were subsequently washed in PBS with 1% BSA (blocking buffer) and incubated with primary antibodies (anti α-Tubulin rabbit IgG, 1 µg/ml, Abcam, Cambridge, UK; anti β-tubulin mouse IgG, 1 µg/ml, Sigma-Aldrich; anti β-actin mouse IgG, 1 µg/ml, Sigma-Aldrich; anti-α-subunit of F_1F_0-ATP-synthase mouse IgG, 1 µg/ml, Molecular Probes, Carlsbad, CA). After 1 h of incubation, the cells were washed with blocking buffer for 10 min and incubated with secondary antibodies (Alexa 488 goat anti-rabbit IgG, 10 µg/ml, Molecular Probes, Carlsbad, CA; Alexa 546 goat anti-mouse IgG, 10 µg/ml, Molecular Probes, Carlsbad, CA; Cy5-conjugated sheep anti-mouse IgG, 15 µg/ml, Dianova, Hamburg, Germany; Cy3-conjugated sheep anti-mouse IgG, 15 µg/ml, Dianova, Hamburg, Germany; DY-485XL-conjugated sheep anti-mouse IgG, 15 µg/ml, Dyomics GmbH, Jena, Germany) for 1 h. Nucleus staining was performed by incubating cells 15-30 min in the presence of DAPI (dissolved in ethanol 2 µg/ml, Sigma). For imaging, the cells were mounted in 97%. TDE containing 0.02 M phosphate buffer pH 7.5.

A.4.4 Cell transfection

For staining, the matrix cells were transiently transfected with GFP and DsRed, respectively, fused to a mitochondrial targeting sequence. Cells were grown to a confluency of about 80%, trypsinized, washed, and resuspended in transfection buffer (120 mM KCl, 10 mM KH_2PO_4, 10 mM K_2HPO_4, 2 mM EGTA, 5 mM $MgCl_2$, 25 mM HEPES, 0,15 mM $CaCl_2$, 5 mM GSH, 2 mM ATP) containing 10 µg of DNA (pcDNA3.1(+)-preSu9 (1-69)-GFP and pDsRed1-Mito, Clontech). A double-pulse protocol was used for electroporation (GenePulser, d = 2 mm, U = 800 V, R = 200 Ω, C = 25 µF, BioRad, USA) and cells were seeded on glass coverslips. 12-16 h after transfection they were fixed in 3.7% formaldehyde and mounted in 97% TDE.

A.4.5 Preparation of the triangularis sterni muscle of P5 mice

Mice from postnatal day 5 (P5) were decapitated using large medical scissors and transected below the ribs to isolate the thorax. The skin, muscles and extremities were carefully dissected away, as well as remnants of the stomach and liver. The cleaned ribcage was placed into 4% PFA/PBS at 4 °C overnight to ensure proper fixation. For dissection of the muscle, the ribcage was tranferred to PBS/0.02% NaN_3 and placed into a Sylgard coated 10 cm dish under a binocular dissection miscroscope. In order to open the ribcage, the ribs were transected close to the vertebral column on both sides and the diaphragm was dissected off the ribs around the entire circumference of the thorax. The thoracic vicera were removed from the ribcage. The two halves of the ribcage were cut away from the sternum and the ribcage was pinned into a 10 cm dish coated with Sylgard polymer (Momentive performance materials), with the inside of the ribs facing upward, and placed under a binocular dissection microscope. Using small scissors the two halves of the ribcage were separated from the sternum by a cut between the bony part of the sternum and the blood vessels running parallel to it. The ribs were then trimmed to near the cartilage-bone transition to obtain a piece of tissue corresponding to the triangularis sterni muscle (Fig. A.1). The tissue was then pinned to the dish with fine hypodermic needles placed at an angle in order to avoid piercing the thin triangularis sterni muscle on top. Starting caudally, the muscle was carefully detached from the ribs and the intercostals muscles by holding on to one side of it and using a fine hypodermic needle to cut away the connective tissue until the muscle could be lifted off the ribs. Finally, the muscle was carefully cleaned from remaining fat and connective tissue and placed into a 24-well plate in PBS/0.02% NaN_3 at 4 °C and stored until IHC staining.

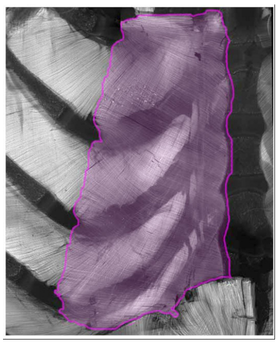

Fig. A.1: Outline of the triangularis sterni muscle between the sternum and the bony part of the ribcage (from Kerschensteiner et al., 2008)

In order to analyze NMJ morphology, triangularis sterni muscles were stained with anti-synaptophysin antibodies to visualize the nerve terminals. Dissected muscles were transferred to 48- (adult muscles) or 96-well plates (P5 muscles) and blocked in antibody buffer (PBS, 0.02% NaN_3, 2% (w/v) BSA, 5% (v/v) goat serum, 0.5% (v/v) Triton X-100) for at least 1 h at RT on a horizontal shaker. Afterwards, Atto565 conjugated anti-synaptophysin antibodies were diluted in antibody buffer and incubated with the muscle over night at RT on a horizontal shaker. Subsequently, the tissue was washed again 3x in PBS and 1x in antibody buffer over a period of 6 h. For imaging, the muscle was mounted in 2,2'-thiodiethanol (TDE) according to Staudt et al., 2007 or Mowiol. In the case of TDE, the muscle was dehydrated in a series of increasing TDE concentrations (10, 25, 50, and 3x 97 %) for 10 min each. Then, the muscle was mounted in TDE and pressed between two metal plates under a 5 L beaker filled with water overnight at 4°C to flatten the tissue.

A.4.6 MCF7 cell culture and immunocytochemistry

MCF7 cells were grown on glass coverslips to semi-confluence in DMEM supplemented with penicillin, streptomycin, glutamine (100 g/ml each) and 10% heat-denatured FCS. This medium will be referred to as normal growth medium. Its total osmolarity was measured as 307 mOsm. To apply water stress, cell cultures were incubated with different loads of sucrose, sorbitol or sodium chloride, added to the normal growth medium. Media were prewarmed to 37°C before application; incubation of cells took place in controlled environments (5% CO2 and 37°C) for about 20 minutes. The osmotic pressure of media was measured by the principle of freezing-point depression (Knauer osmometer, Germany). The crowding agent dextran (10 and 41 kDa, Sigma, Germany) was used at a concentration of 10% w/v, which is equivalent to 320 mM sucrose). Even though cells reacted quickly upon osmotic changes, adaptation of the fixative to the osmotic conditions of the respective experiment did not prove to be necessary. After fixation, the specimens were washed three times in PBS and cells were permeabilized by incubation with 0.05% Triton X-100 (Sigma) and 0.05% Tween 20 (Sigma) in PBS for 10 minutes at room temperature. Then, a protein block was applied by incubation with 1% goat serum in PBS for 10 minutes. Antibodies (anti-SC35 mouse IgG; NK51 goat anti-mouse IgG), diluted in PBS containing 0.1% goat serum, were incubated for 1 hour at room temperature. Each antibody incubation was followed by three short washes with 0.1% goat serum in PBS. Finally, the coverslips were mounted on glass slides with Mowiol or embedded in TDE.

A.4.7 Imaging

For imaging we used a confocal microscope TCS SP2 (Leica Microsystems, Mannheim, Germany) equipped with immersion micro-objectives 63x1.2NA W for the reference samples in buffer and 63x1.4NA Oil or 100x1.4NA Oil for imaging of the samples in TDE respectively. Phase contrast images were taken with a DMRE microscope (Leica Microsystems, Mannheim, Germany) equipped with digital camera D10 (Canon, Japan) and objective N PLAN L 40x0,55NA Corr PH2.

A.4.8 Fluorescent dyes

The following dyes were used for the spectroscopic measurements: coumarin 120 (Lambda Physik, Göttingen, Germany), coumarin 153 (Lambda Physik, Göttingen, Germany), fluorescein isothiocyanate (Isomer I) (FITC) (#F1906, Molecular Probes, Carlsbad, USA), Oregon Green® 488 (#Q6142, Molecular Probes, Carlsbad, USA), Texas Red® (#T1905, Molecular Probes, Carlsbad, USA), BODIPY® FL, SE (#D2184, Molecular Probes, Carlsbad, USA), BODIPY® 650/665-X, SE (#D-10001, Molecular Probes, Carlsbad, USA), Cy3 NHS

(#PA13101, Amersham Biosciences, Buckinghamshire, UK), Atto532 NHS (#AD 532-3, Atto-Tec, Siegen, Germany), Atto565 NHS (#AD 565-3, Atto-Tec, Siegen, Germany), Atto655 NHS (#AD 655-3, Atto-Tec, Siegen, Germany), EGFP, mRFP.

A.4.9 Spectra

The transmission spectrum was measured with a Cary 500 Scan Spectrometer (Varian, Darmstadt, Germany) in a semi micro cell (Hellma, Müllheim, Germany). Fluorescence spectra were recorded with a Cary Eclipse Fluorescence Spectrophotometer (Varian, Darmstadt, Germany). Absorption spectra were measured with a Cary 4000 UV-VIS Spectrophotometer (Varian, Darmstadt, Germany).

A.4.10 Refractive index

The refractive index of the mounting medium was measured with an AR200 Digital Hand-Held Refractometer (Reichert, New York, USA) as a n_D^{23} value (refractive index at 589 nm and 23°C). The refractive index of a standard immersion oil is typically specified as $n_e = 1{,}518$ (refractive index at 546 nm).

A.4.11 Dispersion measurements

The beam of an Innova 70 Ar-Kr-Laser (Coherent, Santa Clara, USA) was separated spectrally using a prism and coupled into a model 197 Abbe Refractometer (Carl Zeiss, Jena, Germany). The refractive index was measured at 466, 476, 483, 488, 514, 521, 531, 568, and 647 nm to determine the dispersion of TDE.

A.4.12 Temperature dependence

The *Abbe* refractometer was connected to a thermostat to measure the refractive index dependence on the temperature of TDE.

A.4.13 pH-Measurement

The pH of the mounting medium was controlled by a PT-10 pH-Meter (Sartorius, Göttingen, Germany) equipped with a PY-P22 electrode (Sartorius, Göttingen, Germany).

Danksagung

Die hochauflösende optische Mikroskopie wird als aktives Forschungsgebiet detailreiche Einsichten in die Zellbiologie eröffnen. Sie kann wichtige Grundlagen für genauere Modelle zur Beschreibung zellulärer Prozesse und Strukturen liefern. In erster Linie möchte ich mich bei Prof. Dr. Stefan W. Hell für die Möglichkeit bedanken, im interdisziplinären und spannenden Umfeld der hochauflösenden optischen Mikroskopie tätig zu sein. Er war immer bereit für produktive Diskussionen und vermittelte stets den Blick für das Ganze. Prof. Dr. Jürgen Wolfrum danke ich für die Unterbringung am Bioquant und Zugang zu einer hervorragenden Forschungsumgebung. Von Dr. Johann Engelhardt habe ich vieles gelernt über Optik und Elektronik. Dank seiner Expertise und Anreize konnten die in dieser Arbeit beschriebenen Methoden erst verwirklicht werden.

Das Potenzial der hochauflösenden optischen Mikroskopie kann nur ausgeschöpft werden, wenn viele Menschen aus unterschiedlichen Forschungsgebieten zusammenarbeiten und die Methoden angewandt werden, um biologische, chemische oder materialwissenschaftliche Fragestellungen zu klären. Großer Dank gebührt daher allen Kooperationspartnern, die helfen, die in dieser Arbeit vorgestellten Methoden zu verbreiten:

> Simone Back, Tabea Mundinger und Katja Wagner von der AG Prof. Dr. Stefan Kins (ZMBH Heidelberg) für APP-markierte primäre Neuronen, neuromuskuläre Endplatten, und Aktin-markierte Zellen
>
> Jakub Chojnacki und Nikolas Herold von der AG Prof. Dr. Hans-Georg Kräusslich (Universität Heidelberg) für unzählige Proben von markierten Viren und SupT1-Zellen
>
> Christian Kempf von der AG Dr. Thomas Kuner (Universität Heidelberg) für die Stammhirn Schnitte zur Untersuchung der *Calyx of Held*
>
> Dr. Michelle Nessling und Dr. Carsten Richter (AG Prof. Dr. Peter Lichter, DKFZ Heidelberg) für die markierten *Speckles*
>
> Daniel Aydin von der AG Prof. Dr. Joachim Spatz (Universität Heidelberg, MPI Stuttgart) für die Bereitstellung von micro-nano strukturierten Metalloberflächen
>
> Dr. Solak Harun (Paul Scherrer Institut, Villigen, Schweiz) für die Strukturierung von Farbstoffoberflächen mittels *X-Ray Interference Lithography*
>
> Dr. Cordula Grüttner (Micromod Partikeltechnologie GmbH, Rostock-Warnemünde) für die Bereitstellung von oberflächen-modifizierten Nanopartikeln
>
> Carsten Steinkamp (Santa Cruz Biotechnology Inc., Heidelberg) und Silvia Löbermann (MPI Göttingen) für die prompte Versorgung mit Antikörpern und die Markierung von sekundären Antikörpern
>
> Dr. Ulrike Engel (Nikon Imaging Center, Bioquant Heidelberg) für die Mitbenutzung der Zellkultur
>
> Dr. Carsten Rippe (Bioquant, Heidelberg) für die Bereitstellung der λ-DNA und die Hilfe bei der Präparation der DNA-Oberflächen

Dem gesamten Arbeitskreis von Prof. Dr. Stefan W. Hell danke ich für die herzliche Aufnahme, das freundliche Arbeitsklima und die Unterstützung bei dieser Arbeit. An die Zeit in Heidelberg werde ich mich immer gerne erinnern, dank der Heidelberger Gruppe Dr. Johann Engelhardt, Dr. Marion Lang, Andreas Engler, Dorothea Sauter, Matthias Reuss, Dr. Scott Irvine, Jale Ozcelik, Franziska Curdt und Pit Bingen. Unsere Diskussionen werden den Besuchern des DKFZ Casinos bestimmt unvergessen bleiben. Dr. Marion Lang, Dr. Scott Irvine und Andreas Engler gebührt Dank für die gute Zusammenarbeit bezüglich des Einbettungsmediums, der *Quantum Dots*, beziehungsweise der Durchführung des RESCue-Projekts. Vielen Dank Dorothee, Matthias und Pit für das Korrekturlesen in letzter Minute. Die Mechanikwerkstatt am DKFZ um Heinrich Rühle fertigte viele Teile des optischen Aufbaus, und trug somit entscheidend zum Gelingen dieser Arbeit bei. Ebenso bedanke ich mich bei Jürgen Vierling, Leiter des elektronischen Entwicklungslabors des DKFZ und seinen Mitarbeitern für viele elektronische Bauteile und einige Oszillographen und dem optischen Werkstatt Team von Wolfgang Kluge in Göttingen. Während der Umbauarbeiten am DKFZ hat uns die AG Prof. Dr. Jürgen Wolfrum und AG Dr. Volker Ebert in ihre Labors aufgenommen; herzlichen Dank hierfür. Ein großer Dank geht an die AG Dr. Dirk-Peter Herten für spannende Fußballspiele, und speziell an Jessica Balbo für viele Messungen am SP5.

Ein besonderer Dank gilt Dorothee Aydin für die Zeit, die sie mit mir teilt, und ihrem gnadenlosen Optimismus.

Meinen Eltern und meinem Bruder danke ich von ganzem Herzen, dass sie mir einen nicht selbstverständlichen Werdegang bedingungslos ermöglicht haben und mir immer ein herzliches Zuhause bieten.

Nach Vollendung ihres 29. Lebensjahrs und viel zu früh von uns gegangen ist unsere Kommilitonin Dr. Katharina Stöhr. Sie ist einem Krebsleiden zum Opfer gefallen und erinnert alle, die an Krebsforschungsprojekten beteiligt sind, warum sie tun was sie tun, und dass es noch Wichtigeres gibt im Leben.

Heidelberg, Januar 2009

List of Publications

PHD thesis:

Staudt, T., Lang, M.C., Medda, R., Engelhardt, J. & Hell, S.W. (2007) 2,2'-thiodiethanol: a new water soluble mounting medium for high resolution optical microscopy. *Microsc Res Tech.* **70**(1):1-9

Staudt, T., Engler, A., Harke, B., Engelhardt, J. & Hell, S.W. Reduction of excitation and signal suppression cycles (RESCue) in zero based high resolution optical microscopy. *in preparation*

Irvine, S.E., Staudt, T., Rittweger, E., Engelhardt, J. & Hell, S.W. (2008) Direct light-driven modulation of luminescence from Mn-doped ZnSe quantum dots. *Angew Chem Int Ed Engl.* **47**(14):2685-2688

Lang, M., Staudt, T., Engelhardt, J. & Hell, S. W. (2008) 4Pi microscopy with negligible sidelobes. *New J Phys.* **10**:1-13

Hell, S.W., Rankin B., Kellner, R., Jethwa, J., Staudt, T. (2007) Fluoreszenzlichtmikroskopisches Messen einer Probe mit rotverschobenen Stokes Linien. *Deutsches Patent* DE 10 2007 048 135.9

Diploma thesis:

Marmé, N., Weston, K.D., Staudt, T., Spatz, J., Knemeyer, J.-P. (2005) A fluorescence-based assay for exopeptidases using self-quenching peptide probes with single-molecule sensitivity. *Int J Environ Anal Chem.* **85**:741-751

Staudt, T.M., Knemeyer, L., Kräusslich, H-G., Knemeyer, J-P., Marme, N. (2005) Novel fluorescently labeled enzyme substrates for the sensitive detection of HIV-protease. *SPIE Proc.* **5704**:112-119

Staudt, T.M., Kräusslich, H-G., Knemeyer, J-P., Marmé, N. (2007) New HIV-protease assays applying self-quenching peptide substrates in combination with time-resolved fluorescence single-molecule spectroscopy *Int J Environ Anal Chem.* **87**:731-743

Erklärung gemäß § 7(3) b) und c) der Promotionsordnung:

a) Ich erkläre hiermit, dass ich die vorgelegte Dissertation selbst verfasst und mich dabei keiner anderen als der von mir ausdrücklich bezeichneten Quellen bedient habe.

b) Ich erkläre hiermit, dass ich an keiner anderen Stelle ein Prüfungsverfahren beantragt bzw. die Dissertation in dieser oder anderer Form bereits anderweitig als Prüfungsarbeit verwendet oder einer anderen Fakultät als Dissertation vorgelegt habe.

(Thorsten Staudt)